UNIVERSIDAD DE CHILE
FACULTAD DE CIENCIAS FÍSICAS Y MATEMÁTICAS
DEPARTAMENTO DE INGENIERÍA ELÉCTRICA

ELECTROMAGNETIC AND DEVICE SIMULATIONS FOR IMPROVEMENTS ON VERTICALLY ILLUMINATED TRAVELLING-WAVE UNI-TRAVELLING-CARRIER PHOTODIODES

TESIS PARA OPTAR AL GRADO DE DOCTOR EN INGENIERÍA ELÉCTRICA

VICTOR HUGO CALLE GIL

PROFESOR GUÍA
ERNEST ALEXANDER MICHAEL

PROFESOR GUÍA 2
PATRICIO MENA MENA

MIEMBROS DE LA COMISIÓN
ENRIQUE MORENO PÉREZ
ANTONIO JESÚS GARCÍA LOUREIRO
RICARDO FINGER CAMUS

ESTA TESIS DE INVESTIGACIÓN FUE FINANCIADA POR LA COMISIÓN NACIONAL DE INVESTIGACIÓN CIENTÍFICA Y TECNOLÓGICA CONICYT

SANTIAGO DE CHILE
2016

Resumen

Los fotomezcladores Verticalmente Iluminados (VI) de Onda Viajera (TW) de Portadores Unipolares (UTC) son fuentes continuas de radiación de THz. Este dispositivo usa la conversión heterodino para generar señales de onda milimétrica. Este dispositivo genera además una corriente distribuida para incrementar su capacidad de manejar mayores cantidades de corriente y además eliminar la limitación de constante RC.

Este trabajo se divide en simulaciones electromagnéticas de alta frecuencia y simulaciones de dispositivos semiconductores. Los estudios de dispositivos semiconductores se enfocan en el modelado numérico del fenómeno de transporte de portadres proveyendo una descripción cualitativa y cuantitativa del transporte de portadores en fotodiodos UTC. Como resultado del análisis de semiconductor, resultados de brecha de energía, espacio de carga, densidad electrónica, velocidad del electrón, todos ellos bajos diferentes valores de potencia de iluminación son presentados en esta sección. Una curva de responsividad versus potencia óptica se muestra también. Esta tesis desarrolla además simulaciones electromagnéticas de alta frecuencia para estudiar la propagación de la onda electromagnética a lo largo del dispositivo VI-TW-UTC. Los fotodiodos VI-TW-UTC ultra-rápidos requieren una capa base altamente dopada que hace de conexión conductora entre el fondo de la estructura mesa y los contactos metálicos de la capa base. Tal estructura se denomina mesa vertical p-i-n o de Uni-Portador. La capa base dopada tiene una fuerte influencia en las perdidas de THz. Por lo tanto, simulaciones electromagnéticas de alta frecuencia fueron ejecutadas en HFSS y CST Microwave Studio para estudiar las pérdidas de THz. El dispositivo VI-TW-UTC fue modelado como una línea de transmisión cuasi-coplanar (Q-CPW). Posteriormente, las pérdidas de THz fueron calculadas indirectamente a través de los parámetros de dispersión S_{21}. Las simulaciones muestran un valle de baja pérdida cerca de la conductividad 5×10^4 Sm^{-1}, en medio de un rango de conductividad de excesiva absorción de THz haciendo este valor la mejor elección para el rango de frecuencia de 0 a 2000 GHz.

Adicionalmente, estructuras de Mushroom-CPW y Wall-CPW se desarrollaron y simularon en la presente tesis para comparar sus pérdidas de THz. Un modelo analítico describiendo la potencia entregada a la entrada de antena del fotomezclador se desarrolló. El modelo analítico tiene como variables de entrada la curva de responsividad versus potencia óptica y la absorción de THz. Como resultado, la conductividad de la capa base muy alta es necesaria para alcanzar una potencia de THz razonablemente alta.

Abstract

The Vertically-Illuminated (VI) Traveling-Wave (TW) Uni-Traveling Carrier (UTC) photomixers are continuous sources of THz radiation. This device uses the heterodyne conversion to generate millimeter-wave signals. This device also generates a distributed current to increase the capability to drive higher currents and also suppress the RC limitation. This device is also vertically illuminated because this way of illumination allows controlling the matching between the optical interference and the THz current traveling along the transmission line. The incident angle between the two lasers illuminating the photomixer controls the phase matching between the optical interference and the THz current.

This work is focused in the numerical modeling of VI-TW-UTC photomixers by dividing the work in semiconductor and High-Frequency RF simulations. The semiconductor studies are focused in the numerical modeling of carrier-transport phenomena providing quantitative and qualitative description of semiconductor transport in UTC photodiodes. The semiconductor analysis is based on the Hydrodynamic Carrier transport Model which treats the propagation of electrons and/or holes in a semiconductor device as the flow of a charged compressible fluid. As a result of the semiconductor analysis, studies of energy bandgap, space charge, electron density, electron velocity, versus distance, and with different applied optical powers are presented in this section. A curve of Responsivity versus Optical power is obtained.

This thesis also performs High-Frequency RF Simulations to study the electromagnetic wave propagation of the VI-TW-UTC device. The VI-TW UTC ultra-fast photodiodes require a highly doped base layer that makes a well-conducting transverse connection between the mesa bottom layer and the bottom metal contacts. Such structure is a vertical p-i-n or uni-traveling (UTC) mesa. The base layer doping has a strong influence in the THz losses. Therefore, High-Frequency Electromagnetic simulations were executed in HFSS and CST Microwave Studio to study the THz losses. The VI-TW UTC device was modeled as a Quasi-CPW transmission line. Then, the THz losses were calculated indirectly through the scattering parameters S_{21}. The simulations show a low-loss valley about a conductivity of 5×10^4 Sm^{-1}, in the middle of a conductivity range of excessive THz absorption and, making this the best choice for the frequency range from 0 to 2000 GHz.

Additionally, the Mushroom-CPW and Wall-CPW structures are also developed and simulated in the present thesis to make a comparison of THz losses against the Quasi-CPW structure. An analytical model for the VI-TW-

UTC photomixer, describing the THz Power delivered at the antenna input versus Frequency and versus Conductivity is developed. The analytical model has as input variables the curve of Responsivity versus Optical power and The THz absorption. As a result, a high n-layer conductivity is needed to reach a reasonable THz power.

"Dedicado a mi madre por todo su amor y soporte en darme la mejor educación posible. Por todos sus grandes sacrificios sin los cuales no hubiese sido posible culminar este gran paso para mi vida"

Acknowledgements

First of all, I would like to express my gratitude to my supervisor Prof. Dr. Ernest Michael, for his continuous support and encouragement throughout this research, his professional guide and an inexhaustible pool of ideas. I deeply appreciate his commitment to academic excellence. I consider it a privilege to have been part of the Radio Astronomical Instrumentation Group at the Faculty of Physical and Mathematical Sciences (FCFM) of the University of Chile.

I would also like to thank Prof. Dr. Patricio Mena for his help with a lot of technical discussions, advices and suggestions. My sincere thanks also go to Prof. Dr. Marcos Diaz, for all the technical guidance, advices and help he rendered during my Ph.D. studies. I also want to thank Dr. Jerald Ramaclus for his help with all his advices, reviews and, suggestions. I want thank visiting student Santiago Bernal from Ecuador for valuable help. Additionally, I would like to thank Prof. Dr. Martin Adams for his comments and suggestions given during the paper preparation. I would also like to acknowledge Prof. Dr. Antonio García Loureiro for your valuable help performing the TCAD simulations in Synopsys Sentaurus.

I am privileged to be a part of this very cordial and friendly Radio Astronomical Instrumentation Group. My research at the University of Chile has been enriched by many discussions with present and previous members of the Radio Astronomical Instrumentation group, especially Laurent Pallanca, Pablo Zorzi, Jaime Álvarez, Claudio Barrientos, Felipe Besser, Dr. Richard Querel, Pablo Barrios, Cristobal Vio, Rafael Rodriguez, and Valeria Tapia. Apart from the research discussions, I would like to thank you all for the fun and refreshing activities we did together. These activities helped me a lot during tough times and gave me the inspiration to go on.

In the end, I would like to thank my mother for their constant encouragement and emotional support, which has been essential in fulfilling this endeavor. Thanks to my brothers Freddy and Carlos, together with their wives, July and Martha, who through their love, persistence, and patience taught me what truly matters in life. Thank you for supporting me through the tough times without expecting anything in return, giving me encouragement to persist this big task. I also want to thank my nephews María José and Martín for being so sweet and giving me their love. I cannot express enough gratitude to my family, and I dedicate this dissertation to them.

This work was realized in the framework of the CONICYT Chile grants Fondecyt number 1090306, ALMA 31080020, 31090018 and 31110014, and a doctoral stipend for V.C. Support was also given through the Chilean Center

for Excellence in Astrophysics and Associated Technologies (CONICYT Project PFB 06).

Victor Hugo Calle
June, 2016.
Santiago, Chile

Contents

List of Figures

List of Tables

List of Acronyms and Abbreviations

Numerical Methods and Computer Software

FEM	finite element method
TLM	transmission-line matrix
FDTD	finite-difference time-domain
FDTLM	frequency-domain transmission-line matrix
MoM	Method of moments
HFSS	High Frequency Structure Simulator
CST	Microwave CST Studio
2-D	two dimensional
3-D	three dimensional
SCN	symmetrical condensed node
PML	perfectly matched layer
PDCM	photodistributed current model
BTE	Boltzmann transport equation
MC	Monte Carlo
DD	drift-diffusion
EB	energy balance
HD	hydrodynamic
LHS	left hand side
RHS	right hand side
SG	Scharfetter and Gummel

Electromagnetics

EM	electromagnetic
CW	continuous wave
RF	radio frequency
MMW	millimeter-wave
LO	local oscillator
DC	zero frequency
RC	resistance-capacitance
CPW	coplanar waveguide
CPS	coplanar stripline
RPW	reverse-propagating wave
FPW	forward-propagating wave
E	electric
H	magnetic
PEC	perfect electric conductor
PMC	perfect magnetic conductor
TE	transverse electric
TM	transverse magnetic

Optoelectronics

EO	electrooptic
OCS	optical communication system
PLO	photonic local oscillator
OFP	optical field profile

Photodetectors

VPD	vertically illuminated photodetector
WGPD	waveguide photodetector
TWPD	traveling-wave photodetector
VMDPD	velocity-matched distributed photodetector
PD	photodiode
UTC	uni-traveling-carrier
MSM	metal-semiconductor-metal
FWHM	full-width half-maximum

Semiconductors

UD	unintentionally doped
SI	semi-insulating
LTG	low-temperature-grown
EH	electron-hole
SRH	Shockley-Read-Hall
GR	generation-recombination
QW	quantum well
MBE	molecular-beam epitaxy
MSM	Metal-Semiconductor-Metal device type
GaAs	Gallium Arsenide
HDCTM	Hydrodynamic Carrier Transport Model
DDCTM	Drift-Diffusion Carrier Transport Model.

List of Symbols

f	frequency	[GHz]
ω	radial frequency	[rad/s]
c	velocity of light in free space	[m/s]
$\vec{E}$	electric field vector	[V/m]
$\vec{H}$	magnetic field vector	[A/m]
$\vec{D}$	electric displacement vector	[As/m^2]
$\vec{B}$	magnetic induction vector	[Vs/m^2]
Z	impedance	[Ω]
R_L	Load resistance	[Ω]
ε_0	dielectric permittivity constant	[A s/(V m)]
μ_0	magnetic permeability constant	
ε_r	relative dielectric permittivity	
μ_r	relative magnetic permeability	
$\vec{A}$	vector field potential	
$\vec{J}$	current density vector	[A/m^2]
I_{ph}	Photomixer photocurrent	[A]
I_{NIR}	Near Infrared Radiation Intensity	
$\mathcal{R}$	Responsivity	[A/W]
Z_0	characteristic impedance	[Ω]
R_A	Antenna impedance	[Ω]
Y_0	characteristic admittance	[S]
h	Planck's constant	[Js]
$\hbar$	Planck's constant	[Js]
k_B	Boltzmann's constant	[J/K]
D_e	Diffusion's constant	[cm^2/s]
ρ	volume charge density	[cm^{-3}]
n	electron concentration	[cm^{-3}]
p	hole concentration	[cm^{-3}]
N_A	Acceptor concentration	[cm^{-3}]
N_D	Donor concentration	[cm^{-3}]
n_1	Concentration of trap states for electrons	[cm^{-3}]
p_1	Concentration of trap states for holes	[cm^{-3}]
n_i	Intrinsic carrier concentration	[cm^{-3}]
φ	electrostatic potential	[V]
$\vec{x}$	spatial position	[cm]
$\vec{k}$	wave vector	[1/cm]
$\overrightarrow{u_\nu}$	carrier group velocity	[cm/s]
f_ν	non-equilibrium probability distribution	
f_{ν_0}	equilibrium probability distribution	
$F_{\nu e}$	external force	[CV/cm]
R_ν	carrier recombination rate	[cm^{-3}s^{-1}]
G_ν	carrier generation rate	[cm^{-3}s^{-1}]

$\overrightarrow{v_v}$	carrier drift velocity	[cm/s]
$\overrightarrow{v_{tv}}$	carrier thermionic recombination velocity	[cm/s]
$\overrightarrow{p_v}$	carrier momentum	[kg-cm/s]
W_v	carrier energy	[J]
W_{v_0}	equilibrium energy	[J]
$\overrightarrow{S_v}$	carrier energy flux	[$Jcm^{-2}s^{-1}$]
T_v	carrier temperature	[K]
T_L	crystal lattice temperature	[L]
f_v^{hf}	Coefficients for heat flux	
f_v^{td}	Coefficients for thermal diffusion	
r_v	Coefficients for energy flux	
m_v^*	carrier constant effective mass	[kg]
τ_{pv}	momentum relaxation time	[s]
$\tau_{\omega v}$	energy relaxation time	[s]
τ_v	carrier lifetime	[s]
τ_{el}	Electrode time	[s]
τ_{tr}	Transit time	[s]
τ_A	Transit time through the absorption layer	[s]
τ_C	Transit time through the collection layer	[s]
τ_{RC}	RC time	[s]
τ_{rec}	Recombination time	[s]
W_A	Absorption layer thickness	[cm]
v_{th}	Thermionic emission velocity (2.5×10^7 cm/s)	[cm/s]
v_{OS}	Velocity overshoot of the electrons	[cm/s]
$\overrightarrow{J_v}$	carrier current density	[A/cm2]
μ_v	carrier mobility	[$cm^2/(Vs)$]
E_g	energy gap	[eV]
E_{trap}	Difference between the defect and intrinsic level	[eV]
χ	electron affinity	[eV]
η	quantum efficiency	
η_{int}	internal quantum efficiency	
$\mathcal{R}$	responsivity	[A/W]
$\overrightarrow{v_{sv}}$	carrier saturation velocity	[m/s]
Γ_{opt}	optical confinement factor	
M	Modulation index	
ℓ_{OE}	Optical and electrical losses	
α_{opt}	optical power absorption coefficient	[m^{-1}]
α_{RF}	attenuation coefficient	[m^{-1}]
P_{opt}	Optical power	[W]
P_{RF}	Microwave power	[W]
P_{THz}	Terahertz power	[W]
P_{inj}	Input optical power	[W]
ε_{eff}	effective permittivity of RF waveguide	
Z_0	characteristic impedance	[Ω]
c	light speed in free space	[m/s]

B_{vm}	velocity mismatch bandwidth [Hz]	
I_{vm}	frequency response due to velocity mismatch	[dB]
I_{tr}	transit frequency response	[dB]
I_f	total frequency response	[dB]
θ	thermal impedance	[°C mm/W]
σ_t	thermal conductivity	[W/(°Cmm)]
T_{opt}	duration of the optical pulse	[s]
R_{opt}	optical reflection coefficient	

Subscript ν stands for "n" and "p" denoting the respective quantity for electrons or holes.

1. Introduction

1.1. Photonic terahertz technology

The generation of powerful tunable continuous-wave (CW) radiation, in the so-called "terahertz gap", has been intensively studied in the last couple of decades [1]–[15]. In fact, there has been rapid progress in the field and several technologies have emerged to fill this gap. One of them is CW systems based on photoconductive mixers (photomixers). They have several attractive features, among them high spectral resolution and tunability in a wide frequency range, both based on the relatively cheap semiconductor lasers. Nevertheless, THz photomixers have a substantial disadvantage: their output power is very low [16]. The generation of THz sources with photonic technology promises new developments in several applications such as high-speed measurements [17], spectroscopy [18], wireless communications [19], security, medicine [17], [20], [21], and, in case the output power problem were alleviated, photonic local oscillators (LO) in radio astronomy [19].

The development of photonic LOs for heterodyne receivers in radio telescopes could be regarded as a challenging research because of the difficulty in obtaining high power and ultra-wide bandwidth sources. The main advantages of this technique over conventional electronic devices are the extremely wide bandwidths (e.g. a 3dB-down frequency of 700 GHz for low-temperature grown (LT) GaAs [22]). In the last years, several research groups have developed new high-speed photodiodes to obtain higher conversion efficiency (responsivity) and ultra-wide bandwidth. Among these devices are the Uni-Traveling Carrier (UTC) photodiodes. These photodiodes have demonstrated to be the most efficient for the generation of CW-THz waves [16], [23]–[25].To eliminate the device RC-time constant and so increase the 3dB-down-frequency, the concept of traveling-wave (TW) in photomixers [26] has been applied for developing edge-coupled photodetectors with larger bandwidth-efficiency products [9], [27]–[30]. However, edge-coupled TW-devices inherently suffer from velocity mismatch between optical and sub-mm wave, as well as power limitations due to the small optical cross section. In contrast, VI-TW-Metal-Semiconductor-Metal (MSM)-mixer structures have been demonstrated to be in full TW mode due to the in-situ adjustability of the optical fringe velocity. These structures have additionally high power capabilities if large optical absorption areas are used (large-area travelling-wave mixers).

Travelling-wave (TW) p-i-n photodiodes are based on the distribution of the photodiode along a (quasi-)planar microwave waveguide and were originally designed for illumination from a buried on-chip optical waveguide

("edge" illumination) [31] [32]. The principle is based on a phased distribution of excitation along the structure, so that the output signal (CW or pulse) is summed up constructively at the end of the microwave waveguide at the transition to the antenna. This results in bypassing the capacitance of the photodiode structure and, therefore, results in the elimination of the RC-cutoff frequency. This principle has been applied to increase the response speeds of telecommunication-type photodiodes towards the deep gigahertz range [33].

A built-in phase mismatch [34] and excessive absorption in the sub-mm range resulted in very short structures suited for the deep gigahertz range as needed for telecommunications but not for signal generation in the higher sub-mm range. One consequence of short structures and edge illumination is the limitation of the input power to still less than 100 mW, because of the very limited absorption volume. In 1999, sub-mm and terahertz (THz) generation from a TW-photomixer structure was demonstrated on a vertically illuminated planar metal-semiconductor-metal (MSM) structure on low-temperature-grown (LT) GaAs layer [35][7]. This structure allowed a useful velocity match between the optical and the THz signal, which enabled longer structures to be optically excited. In a separate research, the uni-travelling-carrier (UTC) photodiode structure was invented in 1997, which demonstrated a substantially more efficient CW-signal generation in the sub-mm and terahertz range [36]. A combination with the "edge-coupled" waveguide-illuminated TW structure has recently been studied [37] and realized [38][39]. To study an *in-situ* velocity-match for a distributed UTC-photodiode and to enable high input power, a combination with the vertically illuminated TW scheme has been proposed [30] and is still under investigation.

1.2. Photomixers

A photodetector is an optical-to-electrical signal transducer. Its function is to convert an incoming modulated light wave into a modulated electrical current. The semiconductor photodetector absorbs the incident light in the absorbing (active) region where the bandgap energy of the material is smaller than the energy of the photons. The absorption of the light generates free carriers which are swept out by a strong electric field inside the active region of the device.

The photodetector can be considered as an electrical two-port device for the electrical output, with an internal generator driven by the optical input (see Figure 1.1). As a linear system, this generator is completely characterized by its impulse or frequency response. The bandwidth of the photodetector is usually defined as the frequency at which the magnitude of the response is 3 dB below the magnitude of the zero frequency (DC) response. Generally, the

bandwidth is determined by two characteristic time-constants. A first contribution is given by the electrode response time, τ_{el}, which is a mixture between the transit time (τ_{tr}) of the carriers from the active (photon-absorbing) region to the contacts. The second contribution is the recombination time of the carriers, τ_{rec}, before they can reach the electrodes. The (effective) electrode response time is

$$\frac{1}{\tau_{el}} = \frac{1}{\tau_{tr}} + \frac{1}{\tau_{rec}} \tag{1.1}$$

The transit-time is determined by the velocity of the carriers and the distance they need to travel to reach the electrodes. A large transit-time bandwidth requires a very thin/narrow active region of the photodetector. A second contribution to the bandwidth is given by the RC-time due to the capacity of the photomixer and the resistance of the embedding (load) circuit.

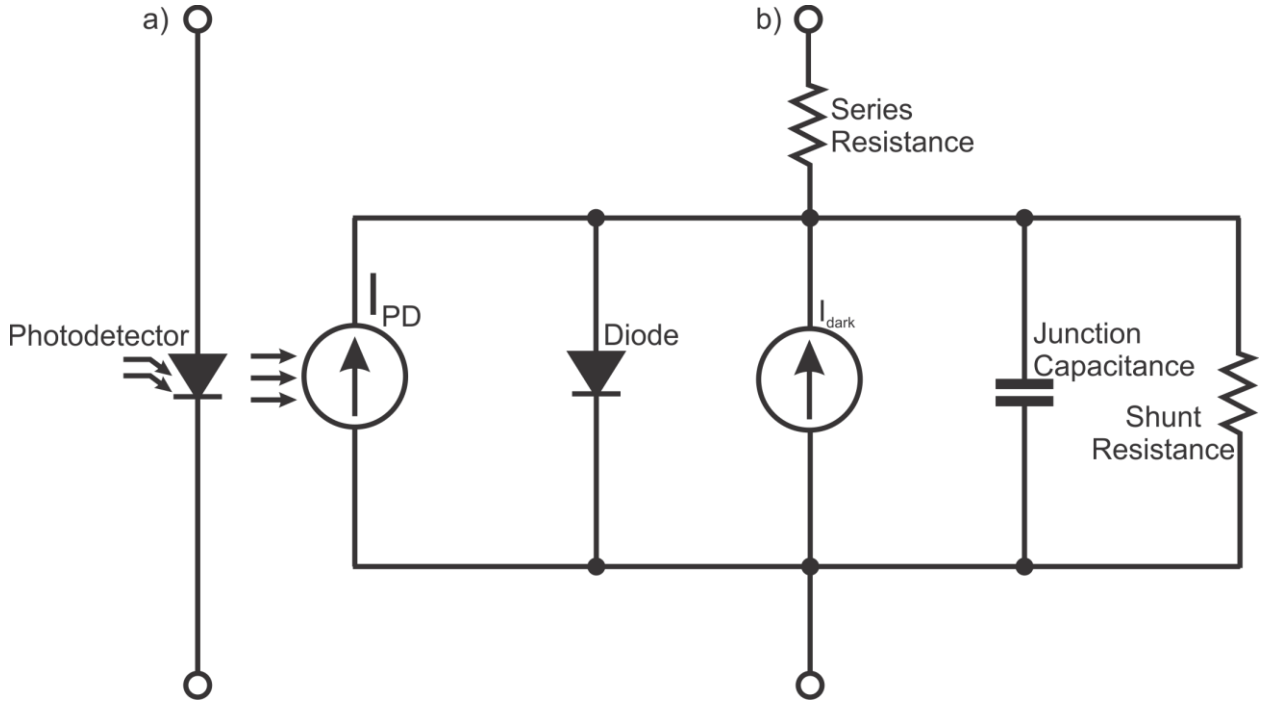

Figure 1.1. Photodiode model. a) Photodiode symbol. b) Equivalent Circuit.

The responsivity $\mathcal{R}$ of a photodetector is defined as the number of electron-hole (EH) pairs generated per photon and detected through the electrodes. It is defined as the output current produced per unit of incident optical power:

$$\mathcal{R} := \frac{I_{ph}}{P_{opt}} \qquad [\mathcal{R}] = \frac{A}{W} \tag{1.2}$$

Its maximum possible value is given by

$$\mathcal{R}_0 := \eta \frac{e}{h\nu} \tag{1.3}$$

where η is the quantum efficiency of the photomixer, which depends on the material and the electrode structure. The realistic responsivity is reduced by the absorbance, α, in the photoconducting medium and its thickness, d, and by the surface reflectivity, R, of the photomixer:

$$\mathcal{R} = \mathcal{R}_0(1-R)e^{-\alpha d} \tag{1.4}$$

The quantum efficiency, η, is then determined by the ratio of the generated photoelectrons in the external circuit to the absorbed photons inside the photoconductor volume. This depends mainly on the ratio of the total recombination time and the total transit time, the so-called "photoconductive gain" G and the multiplication factor m, which are both functions of the applied E-field, i.e. the bias voltage *V*:

$$\eta(V) := m(V) \cdot G(V) =, \text{ where } \quad G(V) = \begin{cases} \frac{\tau_{rec}}{\tau_{tr}(V)}, & \tau_{rec} < \tau_{tr}(V) \\ 1, & \tau_{rec} > \tau_{tr}(V) \end{cases} \tag{1.5}$$

In photodiodes or photoconductors $m > 1$ is caused by impact ionization (Avalanche effect). This is the case in Avalanche photodiodes and also in ultra-fast LT-GaAs photomixers under high bias voltages [40]. It could be seen as if the recombination time is increasing by the factor $m(V)$.

When the recombination time becomes larger than the transit-time, the photoconductive gain stays at 1. Photoconductive mixers in this regime are called "transit-time limited", in the other case they are called "recombination-time limited" or "trap-time limited". Therefore, for a simple photoconductor or a normal photodiode it is $G \leq 1$

It has to be noted that the involvement of these two time constants into the efficiency also makes it dependent on the modulation frequency, i.e. the transit-time roll-off can be seen as a deterioration of efficiency at higher frequencies.

Bandwidth and responsivity are the two most important parameters of photodetectors. They are interrelated, and usually one cannot be improved without deteriorating the other. That is why the so-called "bandwidth-efficiency product" is a very important figure of merit for photodetectors. A large bandwidth-efficiency product is an essential requirement in the design of THz-photomixers. Several different types of photodetectors have been developed in order to satisfy this requirement. In general, they can be separated into lumped and distributed photomixers.

1.2.1. Photomixing theory

Photomixers are based on the physical principle of down-conversion to a microwave, millimeter-wave or THz-signal by employing a high-frequency photodetector (a photomixer) [41]. This is also called optical heterodyning. Two optical waves with frequencies ω_1 and ω_2 and average powers P_1 and P_2 are superimposed and injected into a nonlinear device such as a photoconductor which down-converts the input signals by generating a beat signal with the frequency $f = \omega_2 - \omega_2$, as shown in Figure 1.2. During photomixing, the photons of energy higher than the semiconductor band-gap are absorbed by the electrons present in the valence band which are then excited into the conduction band leaving behind a hole in the valence band – an electron-hole pair has been created. Both photogenerated carriers will remain active during the electrode-response time. After this time, the electron-hole pairs will perform any of the three following processes. In the first process, the electron-hole pair recombines directly between conduction and valence bands (interband transition), eventually assisted by an intermediate energy level (intraband transitions). In the second process, the electron can be trapped for some time by that intermediate level (a defect in the crystal) before a hole is attracted by that charged electron trap and recombines finally (τ_h). In this situation, the carrier can be reemitted or recombined in case that a counterpart carrier interacts with the trap [42]. These devices are recombination-lifetime photodetectors. In the third case, the electrons and holes can reach the electrodes before they recombine. These devices are called transit-time limited photodetectors [43].

During the interference of two laser beams with frequencies ω_1 and ω_2 on the photomixer the instantaneous optical power on the photomixer is given by [18]:

$$P_i(t) = P_0 + 2\sqrt{mP_1P_2}[\cos\{(\omega_2 - \omega_1)t\} + \cos\{(\omega_2 + \omega_1)t\}] \qquad (1.6)$$

where $P_0 = P_1 + P_2$ is the total incident power (averaged over several oscillation periods) and m is the spatial overlap of both laser beams that ranges between 0 and 1. The first cosine term modulates the photocurrent at the difference frequency $\omega_{THz} = \omega_2 - \omega_1$ but the second term, approximately twice the optical frequency, varies on a time scale much shorter than the carrier lifetime τ, and thus does not modulate the photocurrent significantly, since the responsivity is a decaying function with frequency [43]:

$$I_{ph}(\omega) = \mathcal{R}(\omega) \cdot P_{NIR}(\omega) = \frac{\mathcal{R}(0)}{(1 + i\tau_{el}\omega)(1 + i\tau_{RC}\omega)} \cdot P_{NIR}(\omega) \qquad (1.7)$$

Thus, one gets:

$$I_{ph}(t) = \mathcal{R}_0 \cdot P_0 + 2\mathcal{R}_{THz} \cdot \sqrt{mP_1P_2}\cos\{\omega_{THz}t\} \tag{1.8}$$

so that with $P_1 = P_2 = P$ and equal to

$$P_{THz} = \frac{1}{2}R_A\hat{I}_{ph}{}^2 = \frac{R_A m[\mathcal{R}_0 P]^2}{[1+(\tau_{el}\omega)^2][1+(\tau_{RC}\omega)^2]} \tag{1.9}$$

where R_A is the antenna impedance (see Appendix B).

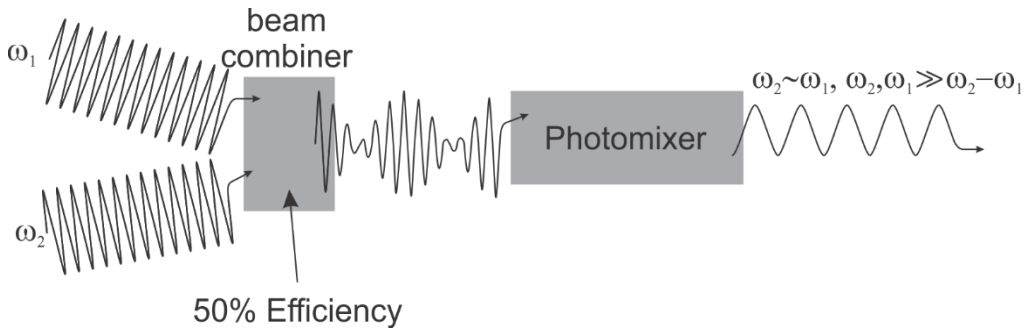

Figure 1.2. Principle of optical heterodyning.

1.2.2. Materials for THz photomixer

When the system is designed such the difference of the laser frequencies falls in the THz range, it is called a THz photomixer.

1.2.2.1. Trap-time limited materials and structures (LT-GaAs photoconductive mixers)

LT-GaAs photomixers are planar metal-semiconductor-metal (MSM)structures which consist of interdigitated metallic electrodes deposited on top of a semiconductor material, as shown in Figure 1.3. The semiconductor material should be an ultrafast photoconductive (PC) material. The most widely used PC material is Low-Temperature grown Gallium Arsenide (LT-GaAs), which is grown at around 200°C in thin layers of 1-2 μm by molecular beam epitaxy (MBE) on top of SI-GaAs. This temperature is used instead of 600 °C, which is the optimum temperature for SI-GaAs, because at 200 °C a lot of defect are created which act as electron-traps. The LT-GaAs has properties of great quality, such as short carrier lifetime (~<0.5 ps), large breakdown-field threshold (>300 kV/cm), and relatively high carrier mobility (~3000 cm^2/Vs [45])[18]. When the MSM photomixer is illuminated with two lasers (the gap of GaAs is at $\lambda \approx 800$ nm) and a bias voltage *V* is applied to the electrodes, a depleted high-field zone is generated between the fingers. In this region, the photogenerated carriers are accelerated into opposite directions and a small fraction is collected by the electrodes whereas the main fraction

recombines within the gap (a small photoconductive gain is the cost of high speed). The gap between the fingers is made small (typically 2 μm, but down to 0.2 μm was demonstrated) to decreases the transit time and so to increase the photoconductive gain. Additionally, the fingers are made thin to reduce their shadow-effect on the responsivity $\mathcal{R}$. Since the reduction of the finger spacing reduces the RC-cutoff frequency, the total area is made as smallest as possible in tradeoff with the total responsivity, proportional to the total area, and thus in tradeoff with the input power capability, which is wanted as high as possible. Overall, due to the fast electron-trapping time, these detectors are extremely fast (cutoff-frequency>500 GHz), but their responsivity is affected largely by that short time in relation to the still relatively long electron-transit time. Although that trapping time should be so extremely short (<0.2ps), it is found that the quantum efficiency increases with increasing bias voltage, which suggests that there is some electron-multiplication gain that arises due to impact-ionization at the electron-traps (avalanche effect) [51]. This impact ionization is equivalent to an increase of the effective electron-trap time, and so this shows that the shortest trap-times in LT-GaAs are not optimal for generation around 1 THz. In fact, one expects naively that the recombination time should be largest possible to increase the photoconductive gain, but not larger than $\tau_{rec} \approx 1/f_{THz}$, where f_{THz} is the desired frequency range to be generated, so that the conductivity-modulation is not washed out by the long transit time. Experiments with ion-implantation of different dose could generate different zero-E-field electron-trap times, and show that there is a maximum of photomixer output power as a function of implantation dose and thus as a function of electron-trap time [46].

If Au/Pt metal contacts are deposited onto the unmodified intrinsic LT-GaAs, the interface forms a Schottky contact barrier which is equivalent to an increased contact resistance. Such resistance could be very detrimental to the optimal performance of those photomixers. However, when such mixers were fabricated with Schottky and ohmic contacts to be compared systematically, only a marginal factor of improvement could be observed [47].

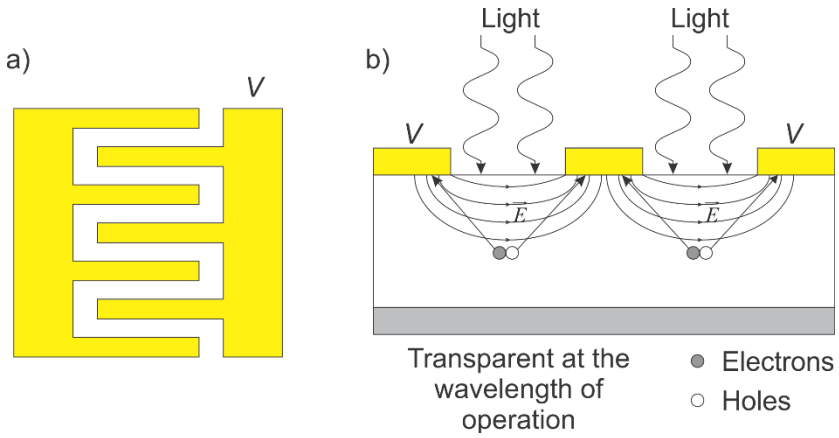

Figure 1.3. a) Top view of an interdigitated form of the MSM photodetector. b) Transversal section of the MSM photodetector.

1.2.2.2. Transit-time limited materials and structures (InGaAs/InP PIN photodiodes (PDs) and UTC PDs)

A transit-time limited device is defined as a device whose frequency bandwidth is limited by the time employed by the carriers to travel across its structure. Among them are the PIN and UTC photodiodes. A *p-i-n* structure is a *p-n* diode with an intrinsic (lightly doped) layer sandwiched between the *p* and *n* layers. The energy-band diagram, the charge distribution, and the electric field for a reverse-biased *p-i-n* photodiode are illustrated in Figure 1.4. This structure serves to extend the width of the region supporting an electric field, in effect widening the depletion layer [44]. The '*i*' region can be also a p^- or n^- layer. In this device, the depletion layer extends through the whole '*i*' region. By virtue of bandgap engineering, the absorption takes place only in the i-layer.

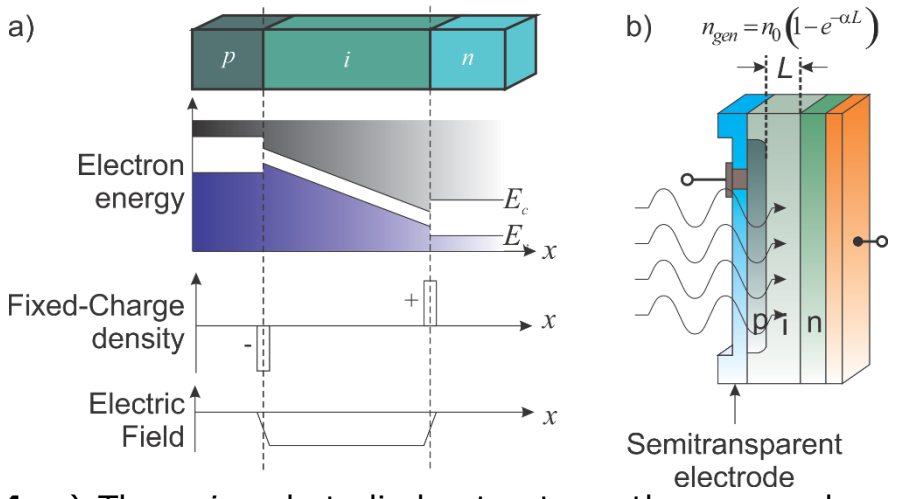

Figure 1.4. a) The *p-i-n* photodiode structure, the energy-band diagram, the charge distribution, and the electric-field distribution. B) The device can be illuminated either perpendicularly to, or parallel to, the junction [44].

PIN photodiodes work as follows. Photons enter to the device with energies at or above the band gap of the i-layer semiconductor, but below the bandgaps of the n- and p-contact semiconductors, and generate electron-hole pairs in the i-layer. The electric field present in this zone pulls electrons and holes in opposite directions, the holes to the *p*-contact and the electrons to the *n*-contact, because of the reverse bias [47].

PIN photodiodes offer several advantages over PN (photo)diodes like increased width of the depletion layer (where photons can be absorbed and the generated carriers see an electric field and are transported by drift) increases the volume available for absorbing photons, furthermore restricting it to a region with electric field (in a pn-diode the band gap is everywhere the same). Increasing the width of the depletion layer reduces the junction capacitance and so the *RC* time constant. As a consequence, a greater proportion of the generated carriers are influenced by the faster drift process [43].

The performance of PIN photodiodes suffers from the fact that holes are much slower than electrons (both have different mobility and effective masses). Because the photocurrent is the sum of electron and hole current, and the contribution of the holes to the high-frequency response of the photodiode is small when compared to that of electrons, the presence of holes in the intrinsic region is detrimental to the electron behavior. This leads to the build up of a space-charge in front of the cathode, causing positive band bending (less bias field in front of the cathode, or even a collapse of the bias field) which leads to a low electron saturation current [38].

Uni-travelling carrier (UTC) photodiodes were invented in 1997 with the intention to decrease this field-screening effect resulting from the bipolar drift and diffusion by suppressing the contribution of holes to the total current of the device [49][36][50]. With this, UTC photodiodes are able to operate at much higher photocurrents [50]. Furthermore, they use a thin depleted transport layer, in which electrons can drift at an overshoot velocity, which can be five times higher than the saturation velocity (see Figure 1.5). Thus, the carrier density in the depletion layer is one-fifth of that in conventional p-i-n structures, further reducing any possible space charge effects [50]. At thicknesses of less 0.2 μm (less than the mean free path in InP), such a layer admits even a totally ballistic transport of the electrons.

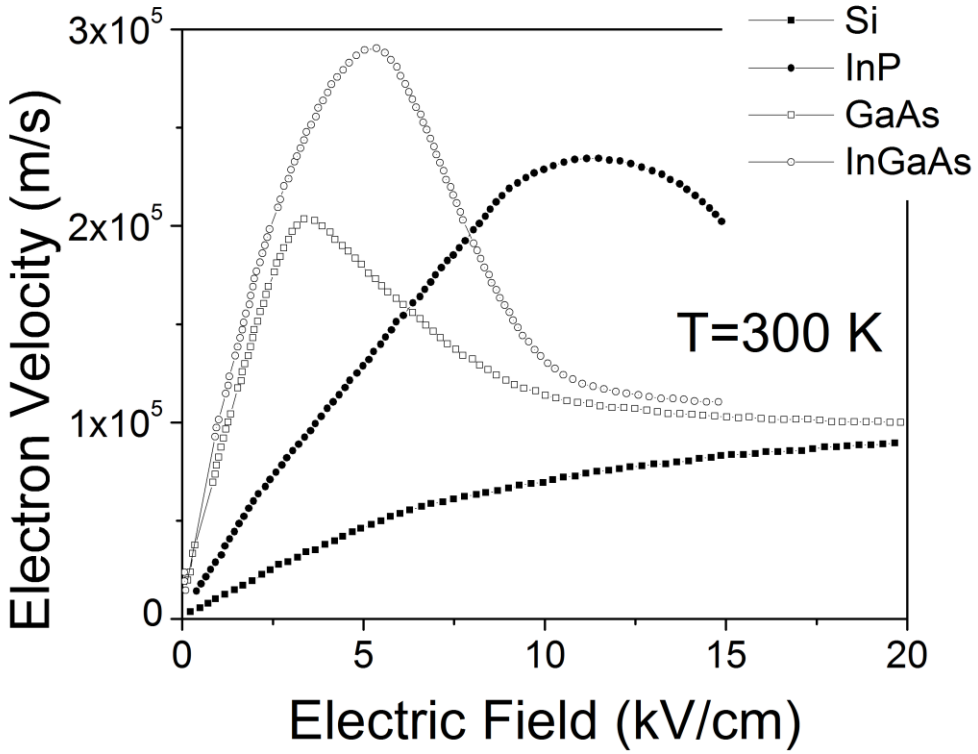

Figure 1.5. Electron velocity field characteristics for InGaAs, GaAs and InP [50].

The energy diagram of a typical UTC-PD device is shown in Figure 1.6. The active layer (the "absorption layer") of the UTC-PD (see ref [50]) is highly p-type doped InGaAs and has a thickness W_A in the range of 100-200 nm. The following wider-gap (depleted) carrier-collection layer is intrinsic or slightly doped InP of a slightly larger thickness. Carriers are photo-generated in the absorption layer, and the electrons (being minority carriers) diffuse/drift into the collection layer. The electrons, having higher mobility than the holes or even overshoot velocity, bridge the complete distance between the electrodes

in the same time as the slower holes drift over the short distance from the absorption layer to the p-contact. The diffusion block layer gives electrons unidirectional motion toward the collection layer. Since holes are the majority carriers, their transport behaves depending on the electron current. Therefore, the photo-response of a UTC-PD is determined by the electron transport in the whole structure. In a typical UTC-PD structure with similar absorption layer thickness W_a and collection layer thickness W_C, the absorption layer traveling time T_a is dominant because the diffusive velocity is usually smaller than the drift velocity in the collection layer with its high electric field [20].

The operation of a UTC-PD device is as follows. The photo-generated electrons in the absorption layer diffuse to the edge of the transport layer by virtue of the concentration gradient built up by the electrons pulled away by the electric field of the transport (collection) layer. Only the electrons enter the transport region, the holes are confined to the absorption region by proper selection of the band profile at the interface between the regions of absorption and transport. On the other hand, the conduction band edge profile must be smooth enough so that it does not hinder the electron transport from the absorption into the transport layer. Ideally, the electrons move ballistically through the entire transport layer, minimizing the transit time. The energy gap of all layers, except the absorption layer, is sufficiently larger compared with the photon energy of illumination so that optical absorption occurs only in the absorption layer [52]. This is the same concept as in the PIN PD.

In a PIN-PD, on the other hand, both electrons and holes in the depleted absorption layer contribute to the response. When electrons and holes travel independently, the output response is the sum of both current components. Here, due to the significant difference in carrier velocities, the 3-dB-down bandwidth is determined by the hole transport. Therefore, due to the large difference in carrier velocities, the UTC design can finally provide a shorter τ_c (carrier transit time) and superior frequency response[50].

The transit time τ_{tr} of a UTC photodiode is given by [50]

$$\tau_{tr} = \tau_A + \tau_C \approx \tau_A = \frac{W_A^2}{3D_e} + \frac{W_A}{v_{th}} \tag{1.10}$$

where τ_{tr} is the transit time through the absorption layer, τ_C is the transit time through the collection layer, which is defined as $\tau_C = W_C/v_{os}$ (v_{os} is the velocity overshoot), W_A is the absorption layer thickness as defined in Figure 1.6, D_e is the diffusion constant and, v_{th} is thermionic emission velocity (2.5×10^7 cm/s). τ_C is much smaller than τ_A. This is the reason why $\tau_A + \tau_C$ is approximated as τ_A in equation (1.10). Thermionic emission is the process where electrons are

emitted across a barrier. The driving force of this process is the thermal energy which provides a non-zero density of carriers at energies larger than the confining barrier [53]. The approximately equal symbol in equation (1.10) is given by the fact that transport through the absorption layer is dominated by diffusive transport (which is essentially slow), thereby the transit time through this layer is larger than the transit time through the collection layer. Therefore, we can approximate both transit times as the transit time through the absorption layer.

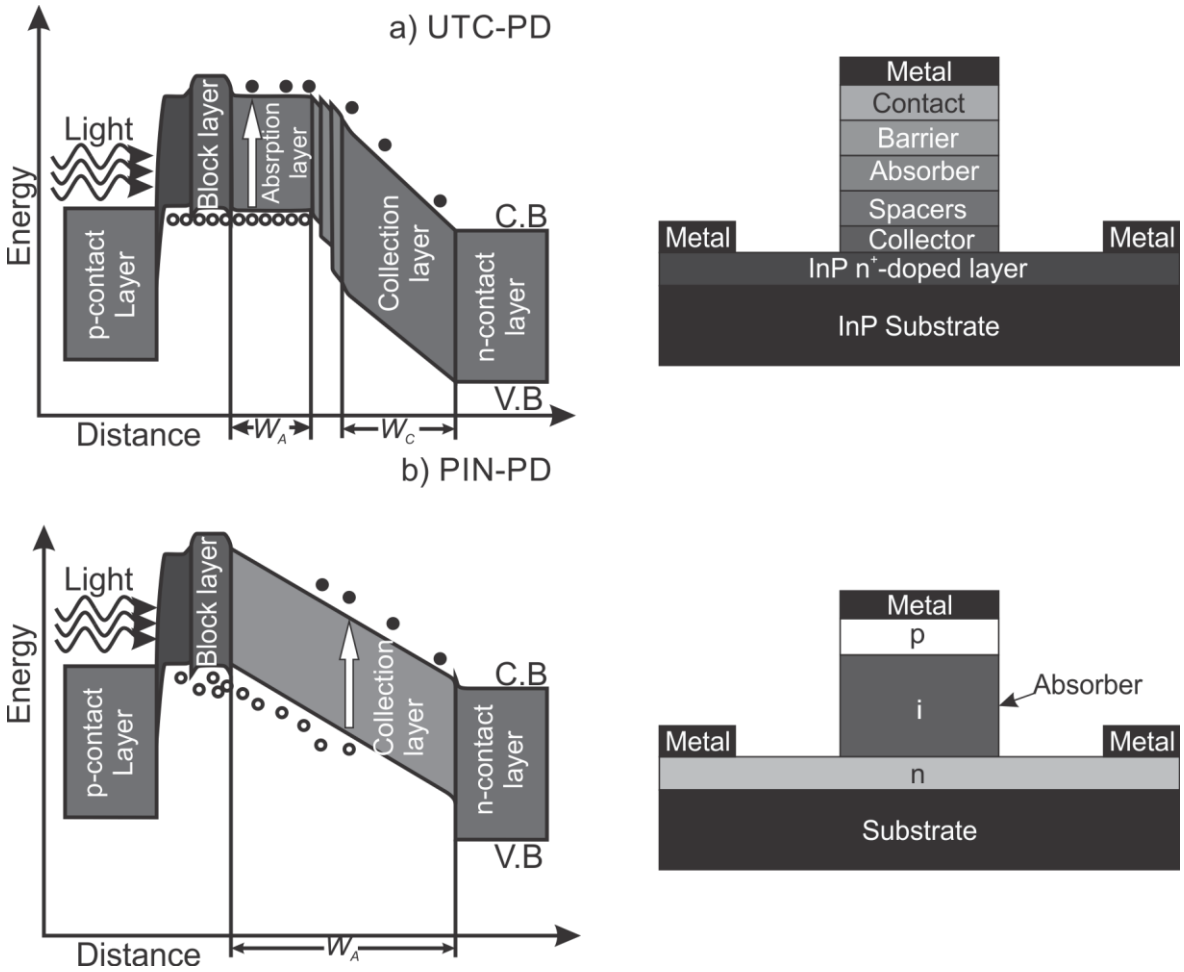

Figure 1.6. Band diagrams (left) and structures (right) of UTC-PD and a PIN-PD in comparison.

The RC-time constant is expressed as [54]

$$\tau_{RC} = RC = \frac{\varepsilon A}{w}(R_L + R_{int}) \tag{1.11}$$

here, R_{int} is the internal resistance, R_L is the load resistance, A is the junction area and w is the full thickness when the UTC photodiode is fully depleted ($w = W_C$ + thicknesses of the intrinsic spacers).

To increase the carrier velocity in the photodiode, τ_{tr} needs to be decreased by reducing τ_A and/or τ_C. It is interesting to note that both layers lead different roles, the absorption layer is related with photogenerated carriers whereas the collection layer interact with carrier transport. The thickness of each layers can be changed without inducing modification in the behavior pattern of the other layer. However, a thinner absorption layer would decrease the photodiode responsivity. Therefore, a balance between speed and responsivity needs to be considered. Moreover, we need to decrease the RC-time constant.

The output power of the UTC photodiode can be expressed as [54],

$$P_{THz} = \frac{R_L \mathcal{R}^2 P_{inj}^2 M \ell_{OE}}{2[1+(\omega\tau_{tr})^2][1+(\omega\tau_{RC})^2]} \tag{1.12}$$

where $\mathcal{R}$ is the responsivity, P_{inj} is the input optical power, M is the modulation index, and ℓ_{OE} is related to optical and electrical losses such optical coupling loss, optical absorption, optical reflection, dielectric loss, conductors loss, and radiation loss[55]. If τ_{tr} is not too different from τ_{RC}, we can write the roll-off as

$$P_{THz} \propto \frac{1}{[1+(f/f_{3dB})^2]^2} \tag{1.13}$$

with a 3-dB bandwidth given by [54]

$$f_{3dB} = \frac{1}{2\pi\sqrt{\tau_{tr}^2+\tau_{RC}^2}} \tag{1.14}$$

1.2.3. THz Photomixer Geometries

1.2.3.1. Lumped-Element (LE) Photomixers (LE PM)

The LE photomixer is a device that employs the heterodyne principle. Its maximum length meets the requirement $L_C \ll \lambda$, where L_C denotes the photomixer's characteristic length, and λ denotes the photomixer output wavelength. Under this condition, the voltage and current parameters can be considered constant along the device length.

In these devices, the THz-radiation power is given by [18]:

$$P_{THz}(\omega) = \frac{I_{ph}^2 R_A}{2[1+(\omega\tau)^2][1+(\omega R_A C)^2]} \tag{1.15}$$

where, R_A is the antenna-radiation resistance and I_{ph} is the DC photocurrent. The parameters R_A, C, and the photocurrent I_{ph} are represented in Figure 1.7 (see appendix 2). This expression is valid for moderate optical power. Equation (1.15) shows that the output power of THz radiation increases in proportion to the square of the bias voltage V_b and the photocurrent and hence, total incident power P_0. It also shows that the output power decreases, on the higher-frequency side, influenced by whether τ or $R_A C$ is dominant, or by both when they are comparable. If small-area mixers are used with broadband antennas of load resistance R_A, the uncompensated device capacitance, C, introduces a roll off, $\sim 1/[1+(\omega R_A C)^2]$, which is usually around 1 THz. This is followed by the unavoidable roll off $\sim 1/[1+(\omega\tau)^2]$, given by the effective response time, τ, for the electronic current seen locally at the electrodes. It is increased by the intrinsic transit time of a space-charge dominated current pulse initiated by the short-living photoelectrons between the electrodes. The restriction on the capacitance imposes upper limits on the device area. All together this results in restrictions on the ultimate generated power above 1 THz [40].

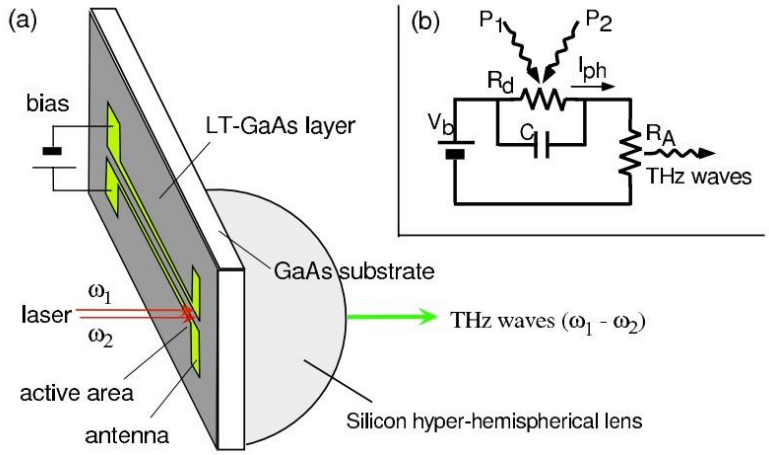

Figure 1.7. Principle of THz generation. (a) Schematic view of two-beam photomixing with a photomixer. (b) Equivalent circuit of the photomixer [18].

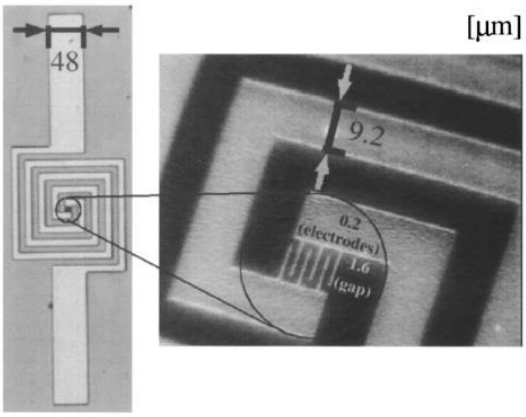

Figure 1.8. Photographs of spiral antenna (left) and interdigitated fingers (right). The fingers are 0.2 μm wide and separated by 1.6 μm [56].

Figure 1.8 shows a typical photomixer with a maximum power typically of 12 μW around ~90 GHz [56] and the band width is ranging from ~20 GHz to ~2 THz. This photomixer has interdigitated fingers, and it is grown on ErAs:GaAs thin films. Each photomixer is coupled to a composite dipole-spiral planar antenna that emits a Gaussian-type beam into free space. The beam switches from dipole to spiral antenna behavior as the frequency increases. A distributed Bragg reflector is embedded in the device beneath the photomixer to increase its external quantum efficiency. The photomixer has a 900 Å thick silicon nitride coating which serves as an antireflection and passivation layer.

1.2.3.1.1. VI Photomixers

The laser beams illuminate the VI photomixer vertically, i.e. they propagate transversal to VI-photomixer layers as shown in Figure 1.9. Therefore, the absorption path length equals the thickness of the absorption (intrinsic) layer. For high efficiency, the absorption layer has to be made as thick as possible. If the VI photomixer is a transit-time based device, then the thick absorption layer means a large distance the photogenerated carriers must travel. This causes long response time and small transit bandwidth of the photodetector. Additionally, since the VI photomixer is a lumped photodetector with and their equivalent circuit is shown in Figure 1.9, others factors such as resistance-capacitance (RC) time constant also limit the bandwidth. The RC bandwidth is inversely proportional to the capacitance of the device, given by $C = \varepsilon A/d$. Here, ε is the dielectric constant of the intrinsic region. Thus, the RC-bandwidth can be increased by decreasing the junction area, A [57].

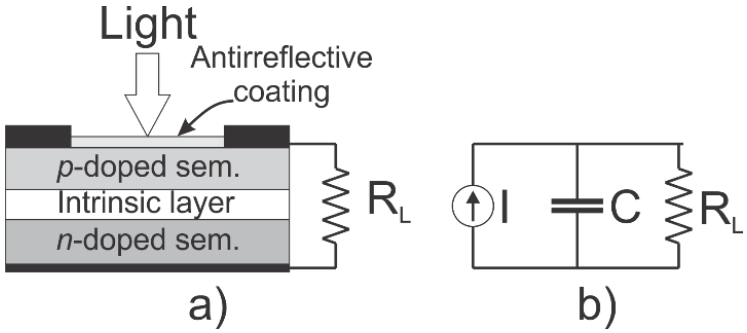

Figure 1.9. Vertically Illuminated photodetector. a) Schematic representation. b) Equivalent circuit [57].

Assuming that the junction area can be made small enough to eliminate the RC limitation, transit response is the only limitation of the bandwidth. In this case, bandwidth-efficiency product of a VI photomixer made of a certain material is a constant. For example, the maximum possible bandwidth-efficiency product of a GaAs-based VPD is about 40 GHz [58]. This constant can be improved only by using a different absorbing material with larger carrier velocity and optical absorption coefficient. However, the availability of such absorbing materials in the range of interest is limited.

1.2.3.1.2. Edge-Coupled (EC) Photomixers

A simplified schematic diagram and the equivalent circuit of a Waveguide Photodetector (WGPD) are shown in Figure 1.10. Layers of the WGPD form a dielectric waveguide, with light-transparent p- and n-doped claddings. The light propagates along the waveguide in the direction perpendicular to the drift direction of the photogenerated carriers. This structure permits a long absorption path while maintaining a short distance traveled by the carriers. Thus, the transit bandwidth and the efficiency of the WGPD can be specified almost independently [57].

The equivalent circuit of Figure 1.10b shows a large mismatch between the characteristic impedance of the photodetector and the load R_L. Consequently, there are multiple electrical reflections from the load degrading the performance of the photodetector. Thus, the WGPD is modeled as a lumped-element device, and its bandwidth is limited by the RC time constant. To decrease this factor, the capacitance should be reduced. Early works focused on decreasing the junction area of the photodetector. However, although smaller area decreased the junction capacitance, it increased the parasitic resistance of the device. Thus the tradeoff between the capacitance and the parasitic resistance was the problem for enlarging the RC bandwidth.

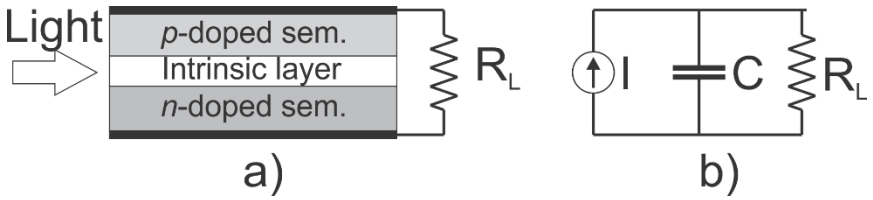

Figure 1.10. Waveguide photodetector. a) Schematic representation. b) Equivalent circuit [56].

1.2.3.2. Travelling-wave photomixers (TW)

In this case, the photogenerated RF power is guided by a microwave planar waveguide in distributed photodetectors. The characteristic impedance of this waveguide can be designed for perfect matching to the load impedance. Therefore, the reflection from the load is eliminated or significantly reduced along with the RC bandwidth limitation. Two of the most common types of distributed photodetectors are the velocity matched distributed photodetector (VMDPD) and the traveling-wave photodetector (TWPD).

The VMDPD is a linear array of ultrafast photodiodes (PDs) serially connected over a light-transparent optical waveguide [59]. Figure 1.11 shows a schematic diagram of the VMDPD. The laser beams are guided from the waveguide to the photodiodes. Each photodiode generates a photocurrent, which is collected by a Ω-coplanar stripline (CPS). The electrical signal phase velocity traveling along the planar stripline is larger than the group velocity of the laser beams in the optical waveguide. The VMDPD reaches its maximum THz power when the RF phase velocity in the CPS matches the optical group velocity of the laser beam interference. VMPDP is used for generation of RF signals in W-band in reference [60] (frequencies up to 100 GHz) through optical heterodyning. A Maximum output current of 25 mA was achieved, with a DC-responsivity of 0.25 A/W.

A traveling-wave photodetector is a WGPD with a planar structure, like a microstrip line or coplanar waveguide with enough length to allow the propagation of RF waves [27]. The photoabsorption process occurs in a distributed manner along the length of the device such that it contributes to the overall electrical signal in the contact transmission line. Therefore, the traveling-wave photodetectors are not limited by the RC time constant, since electrically the devices are not lumped elements with a concentrated capacitance but an electrical waveguide [59]. Figure 1.12 shows a traveling-wave device in which light propagating in the optical waveguide is absorbed exponentially, thus generating a RF power along the way. The RF waveguide is designed with a characteristic impedance matched to that of the embedding microwave circuit. Therefore, the TWPD is modeled as a matched transmission

line with position-dependent photocurrent sources distributed along its length [56].

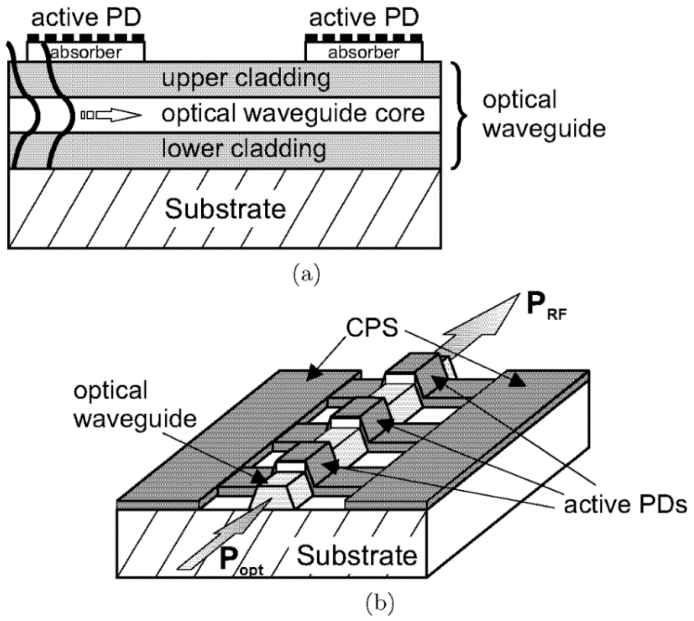

Figure 1.11. Velocity matched distributed photodetector. a) Side view. b) 3D view [59][56].

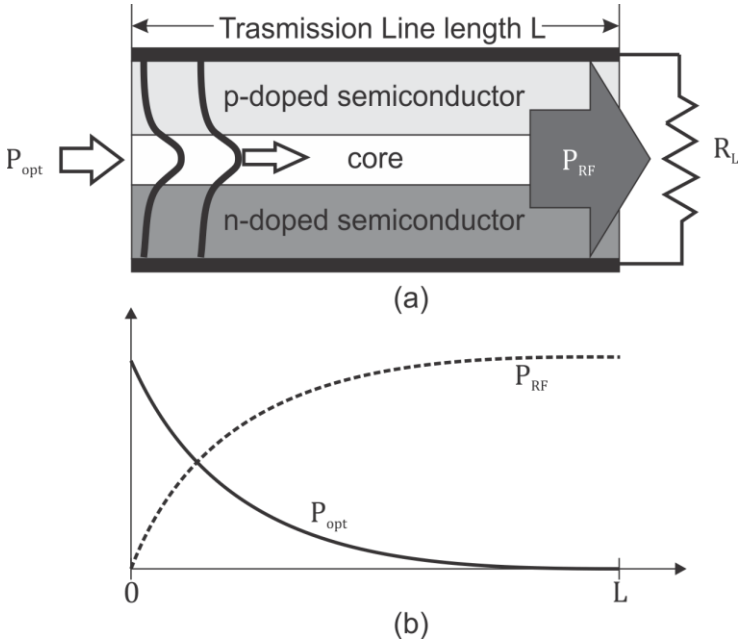

Figure 1.12. Traveling-wave photodetector. a) Simplified schematic. b) Propagation of optical (P_{opt}) and microwave (P_{RF}) powers along the transmission line [56].

1.2.3.2.1. VI-TW photomixers

As indicated above, the distributed photomixer is constituted by a CPS or CPW on a photoconductive substrate connected at one of its ends to a planar antenna. In a VI TW mixer, the photoconductive gaps of this waveguide is illuminated vertically throughout its length by a laser beam (dual-frequency laser in our case) which can excite the fundamental mode of the waveguide. This mode propagates along the guide, loads the antenna, which leads to a continuous terahertz radiation to free space. We consider a local illumination of the photoconductive area of the waveguide between two polarized electrodes. This generates a local THz beat current that produces a periodic perturbation of the voltage across the electrodes. Given the structure of the waveguide, the perturbation will propagate along the waveguide until its end and excites the antenna [62].

A VI-TW mixer works as follows: The TW photoconductor is illuminated vertically by two optical lasers of two similar optical frequencies, υ_1 and υ_2 with $\upsilon_1 - \upsilon_2 = \upsilon_{\mathrm{THz}}$ (see Figure 1.13, left CPS). The two laser beams create a beating signal at the photoconductor; with the cross term $E_1 E_2^* \cos[2\pi(\upsilon_1 - \upsilon_2)t]$ oscillating at the desired THz frequency (see Figure 1.13, right CPS). Here,E_1 and E_2^* represent the electric fields of the two laser beams with their respective phases [63]. After the efficient conversion of the photons into electron-hole pairs, these carriers produce an oscillating photocurrent $I_{\mathrm{THz}} \propto E_1 E_2^* \cos[2\pi(\upsilon_1 - \upsilon_2)t]$. This photocurrent is only a contribution from one differential element of the photoconductor. After that, all these contributions have to be added by varying the spatial phase of the dual optical lasers to meet the phase matching condition. This is done by using a structure in which the THz and optical waves can propagate in the same direction with the same phase velocity, thus avoiding the capacitive problems. One way to meet the phase matching condition is to tilt the two lasers at an angle with respect to each other in order to generate optical interference fringes moving along the waveguide. In the case of a structure vertically illuminated using optical interference fringes to satisfy the condition of phase matching, the running fringes speed must be equal to that of the wave in the waveguide. The two waves then travel along the whole structure. This is the reason for which this mechanism is called "Traveling-Wave Photomixer" [62].

Assuming that the two laser wave fronts are flat, the speed of the optical interference fringes along the surface is given by [7]

$$v_{opt} = \frac{2\pi(f_1 - f_2)}{k_1 - k_2} = \frac{(f_1 - f_2)c}{f_1 \sin\theta_1 - f_2 \sin\theta_2} \tag{1.16}$$

where θ_1 and θ_2 are the incidence angles of the two lasers with respect to a line normal to the photomixer surface, f_1 and f_2 are the laser frequencies, k_1 and k_2 are optical propagation wave constant along the surface, c is the light speed (see the definition of these parameters in Figure 1.14). By changing the angle between the lasers we can change the optical velocity in order to meet the phase matching condition which is given by $v_{op} = v_{\mathrm{THz}}$, where v_{THz} is the group speed of a THz wave generated in a dispersionless transmission line and it is given by [7]

$$v_{THz} = \frac{c}{\sqrt{\frac{(1 + \varepsilon_r)}{2}}} \tag{1.17}$$

where ϵ_r is the dielectric constant of the substrate material.

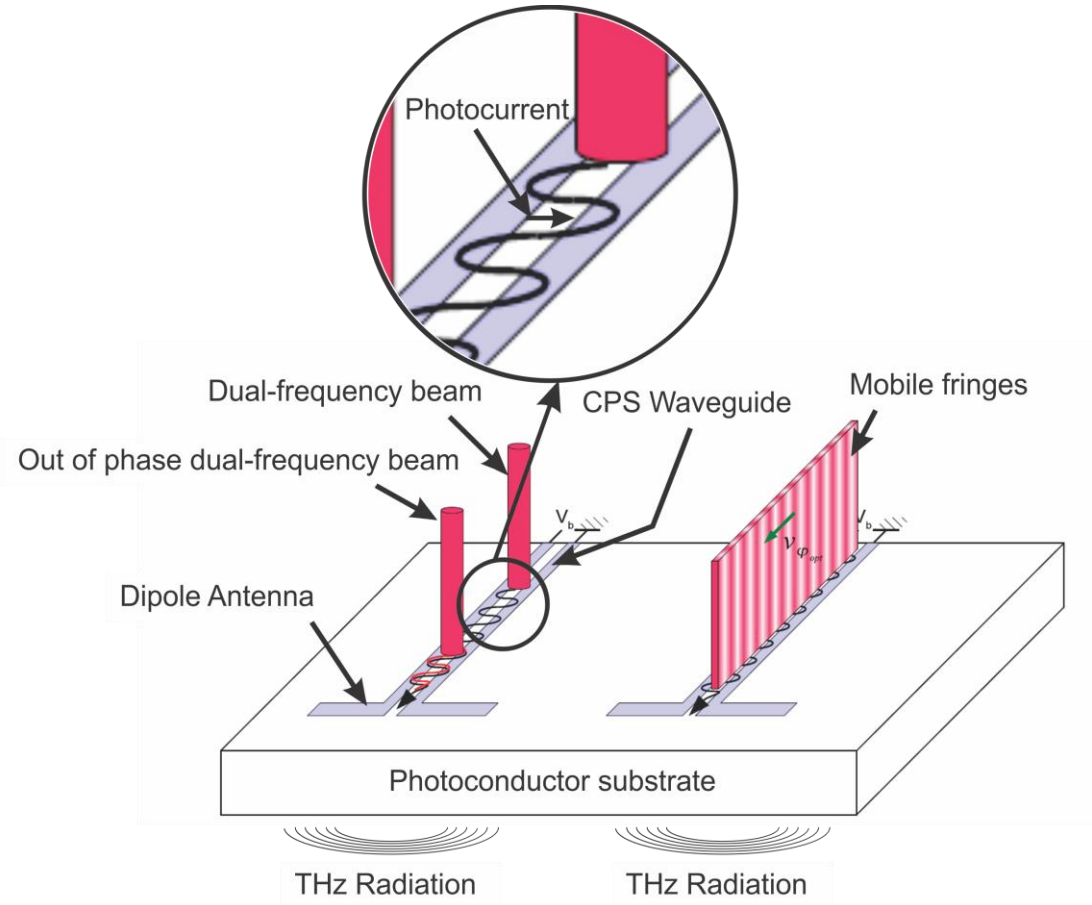

Figure 1.13. Operation principle of a Distributed Photomixer. In this case the waveguide is formed by a CPS loading a dipole antenna. Left CPS: The transmission line is illuminated vertically by two lasers. Right CPS: The two lasers interfere constructively making mobile fringes.

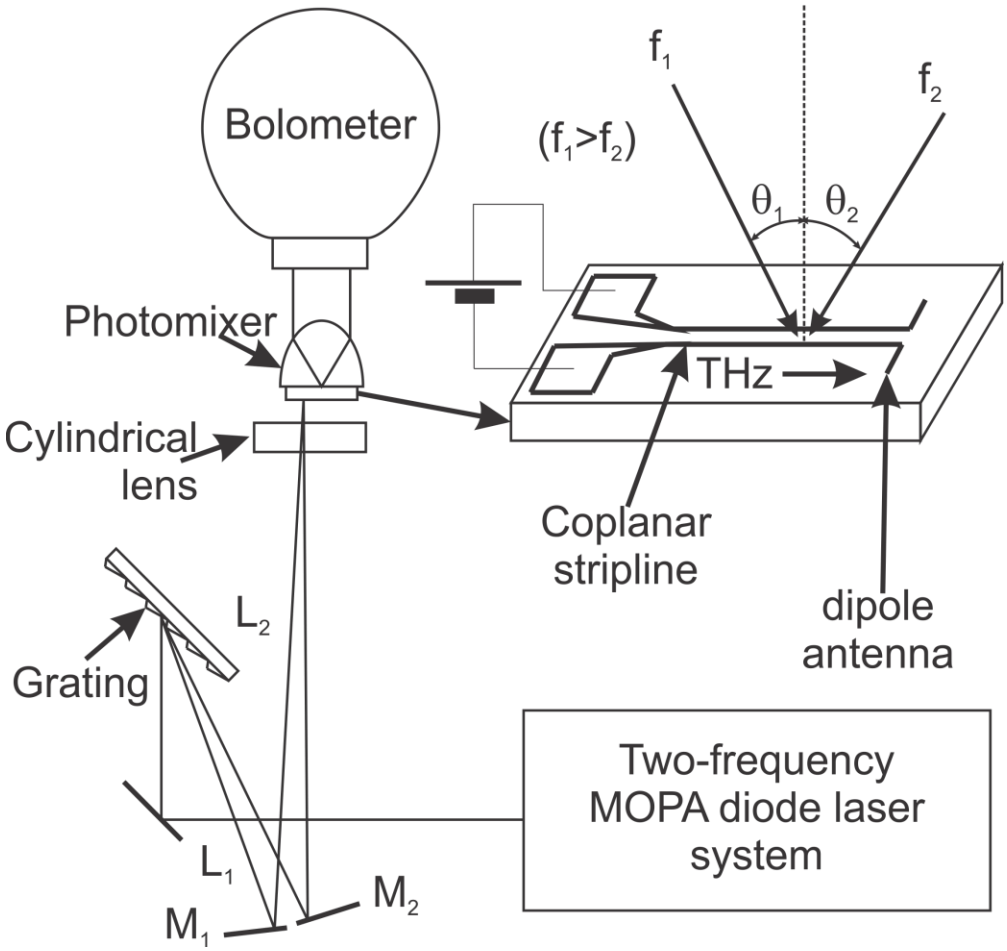

Figure 1.14. Experimental setup from Matsuura et al [7].

1.2.4. Antenna Geometries

As one of the most important part of the chain in the photomixer experiment, the performance and efficiency of the CW-THz source depends strongly on the impedance matching between the photomixer and the antenna. To understand how the antenna affects the performance of a CW THz source, let us consider the power emitted by the different type of photomixers. The THz power of a lumped-element (LE) is given by equation (1.15) [18] [1].

In the case of Traveling-Wave photomixers the THz power is given by simplifying [18] [1] equation (1.15):

$$P_{THz} = \frac{I_{ph}^2 R_A}{2[1 + (\omega\tau)^2]} \tag{1.18}$$

Therefore, the THz power is directly proportional to the antenna impedance. As the impedance of the antenna increases, the THz power will do. Figure 1.15 shows the different broadband antennas used in VI TW

photomixers. The following antennas can be used in both, LE and TW devices, as photomixers.

Reference [39] reports the use of Bow Tie (Figure 1.15a) and planar 2-arm log-periodic antennas (Figure 1.15b) with a TW waveguide as part of their THz sources using Uni-Traveling Carrier (UTC) photodiodes. The Bow Tie antenna reached a maximum of 110 μW at 200 GHz. The planar 2-arm log-periodic antenna climbed up to 600 μW at 10 GHz. Reference [15] reports the use of a planar 2-arm log-periodic antenna with a LE UTC-PD reaching an output power of 2.3 μW at 1.5 THz (Figure 1.15c). Reference [64] reports the use of a LT-GaAs photomixer with a logarithmic spiral (Figure 1.15d). Reference [56] reports the use of a LT-GaAs with a rectangular spiral antenna (Figure 1.8) capable of reach 12 μW. As TW device. Reference [30] reports the development of a TW photomixer based in a distributed UTC-PD along its structure. Its antenna is complementary Bow Tie (Figure 1.15e). For the best of our knowledge, this is the first device which mix the concepts of distributed UTC-PD with a slotted bow tie.

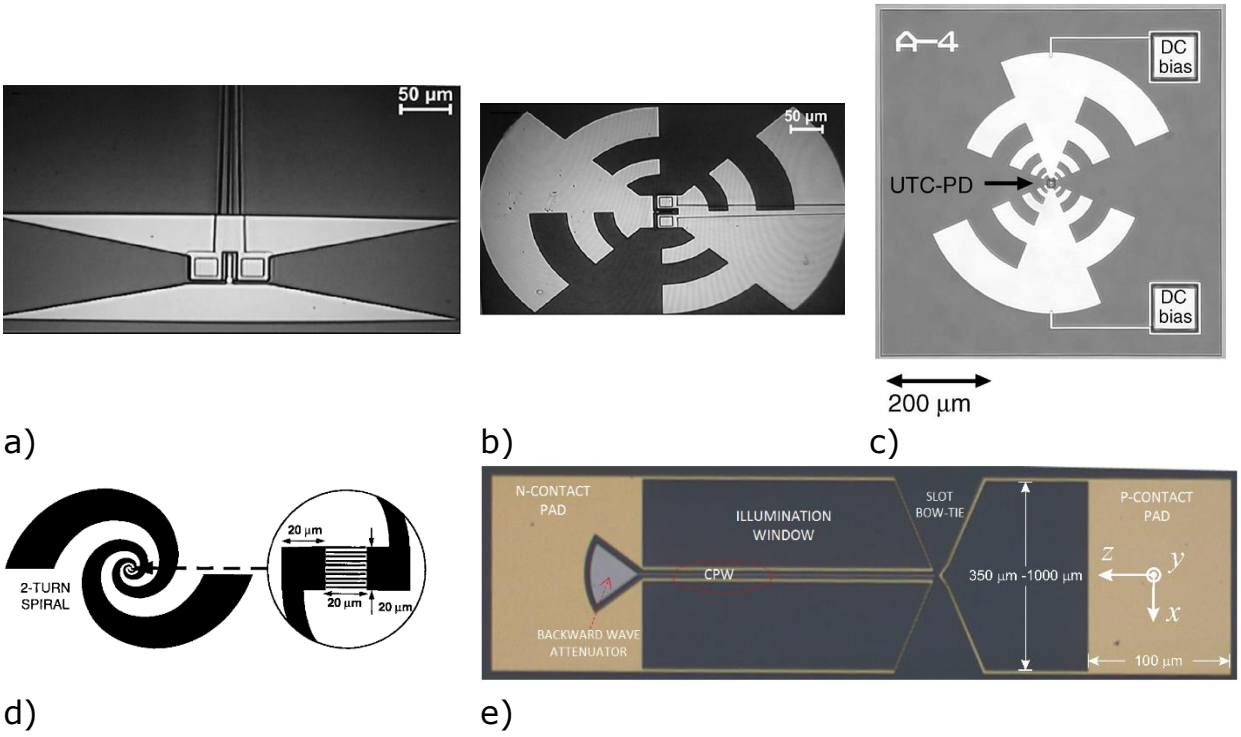

Figure 1.15. Different antennas geometries: a) TW waveguide with a Bow Tie antenna [39], b) TW waveguide with a Planar 2-arm log-periodic antenna [39], c) LE device with a Planar 2-arm log-periodic antenna [15], d) LE device with a Planar Spiral antenna [64], e) TW waveguide with a slot Bow Tie antenna [30].

1.2.5. Why investigating VI-TW-UTC photomixers with broadband antennas?

In both, LE and TW photomixers, the output power is proportional to the square of the photocurrent, and the bandwidth is limited by the photocarrier transit in the case of carrier transit time devices and carrier lifetime in the case of MSM photomixers. In LE photomixers, the electrode capacitance plays a role and it is given by the factor R_aC present in equation (1.15) [65][2]. The LE photomixers can be classified according its carrier behavior, which can be photomixers based in photoconductor material with and without electron traps (devices whose performance is based in the carrier traveling from the absorption layer to one of their cathodes) [34]. The RC tradeoff is common to both devices. As example of photomixers based in carrier transport phenomena is the PIN photodiode, both electrons and holes are involved in its carrier transport. Because the electron velocity is high when it is compared with hole velocity, their transport dominates the space charge effect and saturation current. This is known as space-charge tradeoff [50]. Conversely, the UTC-PD device is designed to have an unidirectional motion dominated only by the electrons, overcoming by this way the space-charge tradeoff [50][66]. The PIN photodiode bandwidth is mainly determined by the time that carriers take to travel between the contacts. Therefore, as the intrinsic layer thickness of the PIN photodiode is made thinner, shorter the transit time of the electrons and holes, and consequently, higher is its bandwidth. However, the reduction of the thickness has two negative consequences: an increased capacitance of the depleted region and lower responsivity in the case of photodetectors illuminated vertically [26]. The photomixers based in electron-trap behavior have been designed to have narrow electrode gaps for high photocurrent and small active areas for small capacitance. Consequently, such designs have limited power handling capabilities [5][7]. The edge-coupled WGPD has an optical waveguide structure in itself. Its main tradeoff is that it is difficult to obtain efficient coupling or good overlap integral between the input optical field and the optical field at the photodiode [67]. The TW photomixer overcome these tradeoffs. However, the TW photomixer adds another tradeoff, the matching between the optical interference fringe and the THz waves [34]. Again, to overcome this effect, the VI TW photomixer was proposed. The phase matching is fulfilled by tuning the incident angle of two laser beams. Up to date, the highest generated output power delivered by a LE photomixer is a UTC-PD device, which generates 25 μW output power at 914 GHz [68][67]. Therefore, they are promissory candidates for CW sources, because its carrier transport based in only electron transport. To reach new levels of THz-power output, a combination of VI-TW- UTC photomixer is studied here. Therefore, the goal of this thesis is on the design and analysis of VI TW UTC with broadband antennas by the use of computer simulations. We

will focus mainly on two areas: Semiconductor Carrier Transport and High-Frequency and Electromagnetic simulations.

1.2.6. Hypothesis

The hypothesis presented in this doctoral thesis are the following:

- It is possible to obtain the VI-TW-UTC-PD performance by performing carrier transport and electromagnetic high-frequency RF simulations separately over the electromagnetic structure where the UTC photodiode is supported.

- As the doping of the UTC-PD n-layer is changed, its conductivity changes, the THz absorption of the transmission line which composes the VI-TW-UTC device changes. Therefore, the n-layer doping has a strong influence in the RF behavior of the VI-TW-UTC photomixer.

1.2.7. Contributions of this work to the state of the art

This Thesis deals with computational simulation of the VI-TW-UTC photomixer dividing the simulations in two different kinds of modeling due to its semiconductor and electromagnetic nature. They are referred as Semiconductor Carrier Transport and High-Frequency Electromagnetic Modeling.

The contributions come mainly from the High-Frequency Electromagnetic Modeling and are the following. The first contribution from this thesis is the study of the dependence of the THz loss with the highly doped base layer doping measured indirectly through the conductivity. This study was performed in HFSS™ and CST Studio™. This study lead to a publication in Journal of Physics D: Applied Physics [70].

Full-Wave numerical calculations of the THz losses of a VI-TW-UTC photodiode as a function of the ground layer conductivity were done in this paper. These results were validated by the employ of an analytical model and the decay rate of a photocurrent along its transmission line. Finally, the most important conclusion from this paper was that there is ground layer conductivity when the THz loss is minimum. This conductivity value will be used as a reference value for the best doping value of the ground layer.

This thesis also contributes with the proposal of an analytical model for the THz power developed by the VI-TW-UTC photomixers. This analytical model takes into account the THz losses calculated using HFSS™, the conductivity of the n-doped layer, the applied voltage, the responsivity

calculated from the Carrier Transport Simulations. The optical Intensity employed by the lasers. From this analysis, the optimal n-doped layer conductivity values for which the THz output is maximum matches with these reported by the publication for this thesis [70].

In the semiconductor field, this thesis also proposes the use of homojunction materials for the absorption and collection layer to suppress the cliff layers to make the transition between these layers totally smooth.

1.2.8. Overview of this Thesis

Chapter 2 starts by defining the VI-TW-UTC photomixer. It also explains that the VI-TW-UTC photomixer will be analyzed by two parts, the semiconductor parts which corresponds with LE-UTC photodiode, and the electromagnetic part which corresponds with the transmission line, i. e., the TW line. This chapter also gives a short review of the hydrodynamic carrier transport. Responsivity and charge space are investigated.

Chapter 3 presents a brief review about High-Frequency RF modeling and the tools used in this dissertation with a short explanation of the numerical method used by these tools. This section contains the two most important issues discussed in this thesis. To understand them, this section will focus particularly in the strong doped layer and its influence in the High-Frequency RF outputs. The most important output from these simulations are the THz losses, calculated from the scattering parameters. The doping is measured indirectly through the conductivity value. The second issue regards the THz power generated at the junction between the transmission line and the antenna. Moreover, the THz losses and THz power of two new structures are evaluated with the purposes of making a comparison.

2. Carrier Transport Modeling of LE P-I-N and UTC Photodiodes

The Astronomical Instrumentation Group is developing a novel device [71], which is a merger of two ideas, the concept of vertically illuminated TW photomixers and the concept of UTC layer systems: vertically pumped TW-UTC structures. Figure 2.1 shows a schematic diagram of the vertically illuminated TW-UTC photodiode. Figure 2.1a) shows the layer structure along a vertical axis extending along a CPW line as shown in Figure 2.1b. The TW-UTC photodiode is a transmission line which is composed of a vertically stacked semiconductor layers corresponding to the UTC photodiode (see Figure 2.1a) placed in a distributed manner along the center conductor of a CPW configuration (see Figure 2.1b).

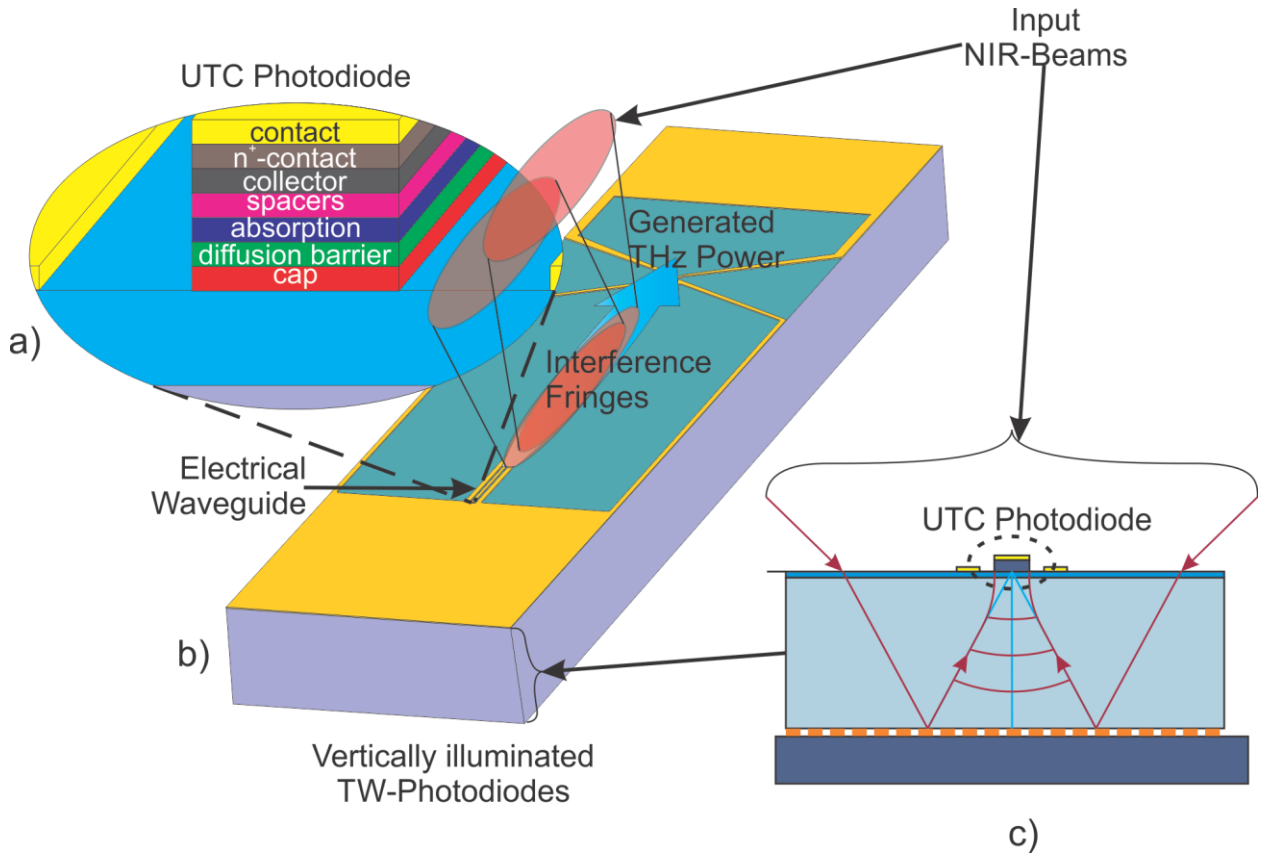

Figure 2.1. Proposed principle of travelling-wave UTC structures. a) layer configuration. b) Vertically illuminated TW-UTC [71]. c) The input NIR beams passes through the top surface, it is reflected at the back side of the chip and absorbed by the absorption layer. The dashed oval represents the cross-sectional UTC PD.

2.1. LE-UTC-Photodiodes

The LE-UTC photomixer has demonstrated to have the highest output power in the submillimeter range due to their high saturation currents and record fast transit times [50]. A UTC-PD-based photomixer for THz wave generation with an output of of 1.1 μW at 940 GHz for 50 mW of total optical power (photocurrent) was developed in reference [72]. A system of two discrete UTC-PDs were developed. They reached output records of 1.2 mW at 300 GHz with a saturation current of around 40 mA from a 240-mW optical input [73]. Moreover, an output power of 10.9 μW at 1.04 THz and a twin-dipole planar antenna [74].

These devices suffer limitations because of heating, optical absorption, or space charge deformation. The main heating mechanism loss is the Joule Heating (ohmic heating) [52]. The limitation by optical absorption is due to the accumulation of electrons in the absorption layer. These electrons can block the flow of light through this layer [52]. The deformation of the space charge appears because the electric field inside the device is modified due to the oscillating space charges and they disturb the currents flowing there and, in the end, they can also limit the output THz power of the photodiode [52]. This chapter will focus in the space charge limitation, and with the help of computer simulations, demonstrate the strong influence of the cliff layers in the electric field inside the LE-UTC device.

This section will describe the layer structure of the InGaAs/InP UTC-PD and the models used to describe the carrier transport, the Drift-Diffusion and Hydrodynamic carrier transport models.

To account for velocity overshoot (see section 1.2.2.2) in the simulations, the Hydrodynamic Carrier Transport Model (HDCTM) was used[75], [76]. The HDCTM treats the propagation of electrons and holes in a semiconductor device as a flow of charged compressible fluid, producing hot electron effects and velocity overshoot. The transport model is based on the approach involving the solution of a number of partial differential equations. The model consists of the Poisson's equation, continuity equations and the energy conservation equations for electrons, holes, and the lattice.

The epitaxial layer of the InGaAs/InP were modeled using the software Sentaurus TCAD™ from Synopsys™ [77]. Table 2.1 shows the epitaxial layers of the device and the layer parameters. This layer's arrangement allows the use of only electrons as the active carrier and it also gives the unidirectional motion of the electrons [49]. Sentaurus Device is a widely used and commercially available multi-dimensional numerical device simulator [77]. It

is primarily designed for simulating the thermal, electrical, and optical characteristics of silicon devices, but it is also capable of simulating compound semiconductor material such as GaAs. Terminal currents, voltages, and charges are computed based on a set of physical device equations based on the carrier distribution and conduction mechanism. Sentaurus can adopt various 1D, 2D & 3D mesh sizes, generated by the Sentaurus Device Editor software. Sentaurus Device self-consistently solves Poisson's equation and two current continuity equations in order to calculate the carrier densities, potential, field strength, and carrier distribution. In addition, one of the major advantages is its ability to selectively include specific numerical model functions such as mobility, tunneling effects, or bandgap narrowing.

This thesis will be restricted to 2D simulations with the HDCTM model. To compute the carrier density crossing through the device, a cylindrical device is assumed. Therefore, when the current density is calculated, Sentaurus TCAD automatically translate the 2D current profile using cylindrical coordinates, that is, it is rotated around the y-axis [73]. Two cylindrical devices were simulated. They were about 3 and 10 μm diameter. The simulations were performed with the purpose of getting a physical understanding by numerical modelling, the original UTC-PD epitaxial structure was used [49].

Table 2.1. Layer parameters of the simulated InGaAs/InP UTC-PD in TCAD.

Layer	**Material**	**Thickness (nm)**	**Doping Level (cm^{-3})**	**Band gap (eV)**
P-Contact	*p*-$In_{0.53}Ga_{0.47}As$	50	3×10^{19}	0.73
Diffusion Barrier	*p*-$In_{0.63}Ga_{0.37}As_{0.80}P_{0.20}$	20	2×10^{19}	0.85
Absorption	*p*-$In_{0.53}Ga_{0.47}As$	220	1×10^{18}	0.73
Spacing	*i*-$In_{0.53}Ga_{0.47}As$	8		0.73
Spacing	*i*-$In_{0.76}Ga_{0.24}As_{0.52}P_{0.48}$	16		1.0
Spacing	*i*-InP	6		1.35
Spacing	*n*-InP	7	1×10^{18}	1.35
Collector	*n*-InP	263	1×10^{16}	1.35
Subcollector	*n*-InP	50	5×10^{18}	1.35
Etch stop, *n*-contact	*P*-$In_{0.53}Ga_{0.47}As$	10	1.5×10^{19}	0.73
Etch Stop	*P*-$In_{0.53}Ga_{0.47}As$	10		0.73

2.1.1. Drift-Diffusion Model

The drift-diffusion carrier transport model[57][78] consists of a set of Poisson's equations and the first two moments of Boltzmann's transport equation. The total carrier energy is assumed to be constant throughout the device; thus, the carrier velocity is dependent on the electric field only. The equations are given by [77]

$$\nabla(\varepsilon_0\varepsilon_r\nabla\varphi) = q(n - p - C) \tag{2.1}$$

$$\vec{\nabla}\cdot\vec{J}_n = qR_{net,n} + q\frac{\partial n}{\partial t} \tag{2.2}$$

$$-\vec{\nabla}\cdot\vec{J}_p = qR_{net,p} + q\frac{\partial p}{\partial t} \tag{2.3}$$

$$\vec{J}_n = -q\mu_n n\vec{E} + qD_n\vec{\nabla}n \tag{2.4}$$

$$\vec{J}_p = -q\mu_p p\vec{E} + qD_p\vec{\nabla}p \tag{2.5}$$

$$\vec{E} = -\vec{\nabla}\varphi \tag{2.6}$$

where φ is the electrostatic potential, n and p are the electron and hole carrier concentrations, q is the electron charge, ε_0 and ε_r are vacuum and relative dielectric permittivities, $\vec{J}_{n,p}$ are the electron and hole current densities, $\vec{E}$ is the electric field, $R_{net,n}$ and $R_{net,p}$ are the electron and hole net recombination rate, while $\mu_{n,p}$ and $D_{n,p}$ are the electron and hole mobilities and diffusivities, respectively. Similarly,

$$C = N_D - N_A \tag{2.7}$$

where $N_{D,A}$ are the donor and acceptor concentrations.

The net recombination takes into account the carrier generation and recombination processes to maintain a balance between the electron and hole concentrations inside the semiconductor crystal. The Shockley-Read-Hall

(SRH) process is one of the most widely modeled generation-recombination processes. The SRH rate is given by [77]

$$R^{SRH} = \frac{np - n_i^2}{\tau_p(n + n_1) + \tau_n(p + p_1)} \tag{2.8}$$

Where n_i is the intrinsic carrier concentration, τ_n and τ_p are the electron and hole lifetimes, n_1 and p_1 are concentrations of trap states for electrons and holes, respectively, and they are given by

$$n_1 = n_{i,eff} \exp\left(\frac{E_{trap}}{k_B T}\right) \tag{2.9}$$

and

$$p_1 = p_{i,eff} \exp\left(\frac{-E_{trap}}{k_B T}\right) \tag{2.10}$$

where E_{trap} is the difference between the defect level and intrinsic level. The minority lifetimes τ_n and τ_p are modeled as a product of doping-, field-, and a temperature-dependent factor as

$$\tau_c = \frac{\tau_{dop} f(T)}{1 + g_c(F)} \tag{2.11}$$

where $c = n$ for electrons or $c = p$ for holes.

In equations (2.1)-(2.6), it was assumed that carrier ge1neration and recombination always refer to electron-hole pairs; thus, $R_n = R_p = R$ and $G_n = G_p = G$. Furthermore, the equations include the diffusion constant D_v, defined by the Einstein relation for non-degenerate semiconductors

$$D_v = \mu_v \left(\frac{k_B T_L}{q}\right) \tag{2.12}$$

where T_L is the lattice temperature.

2.1.2. Hydrodynamic Carrier Transport Model

The hydrodynamic carrier transport model treats the propagation of electrons and/or holes in a semiconductor device as the flow of a charged compressible fluid producing hot electron effects and velocity overshoot. The transport model is based on the approach involving the solution of a number of partial differential equations. The model consists of the Poisson's equation,

continuity equations and the energy conservation equations for electron, holes, and the lattice. The equations are given by [54]

$$E_C = -\chi - q(\varphi - \varphi_{ref}) \tag{2.13}$$

$$E_V = -\chi - E_{g,eff} - q(\varphi - \varphi_{ref}) \tag{2.14}$$

$$\begin{aligned}\vec{J}_n = \mu_n\big(n\vec{\nabla}E_C + k_B T_n \vec{\nabla} n - n k_B T_n \vec{\nabla}\ln\gamma_n + \lambda_n f_n^{td} k_B n \vec{\nabla} T_n \\ - 1.5 n k_B T_n \vec{\nabla}\ln m_e\big)\end{aligned} \tag{2.15}$$

$$\begin{aligned}\vec{J}_p = \mu_p\big(p\vec{\nabla}E_V - k_B T_p \vec{\nabla} p + p k_B T_p \vec{\nabla}\ln\gamma_p - \lambda_p f_p^{td} k_B p \vec{\nabla} T_p \\ + 1.5 p k_B T_p \vec{\nabla}\ln m_h\big)\end{aligned} \tag{2.16}$$

$$\frac{\partial W_n}{\partial t} + \vec{\nabla}\cdot\vec{S}_n = \frac{\vec{J}_n\cdot\vec{\nabla}E_C}{\mathrm{q}} + \left.\frac{dW_n}{dt}\right|_{\mathrm{coll}} \tag{2.17}$$

$$\frac{\partial W_p}{\partial t} + \vec{\nabla}\cdot\vec{S}_p = \frac{\vec{J}_p\cdot\vec{\nabla}E_V}{\mathrm{q}} + \left.\frac{dW_p}{dt}\right|_{\mathrm{collector}} \tag{2.18}$$

$$\frac{\partial W_L}{\partial t} + \vec{\nabla}\cdot\vec{S}_L = \left.\frac{dW_L}{dt}\right|_{\mathrm{collector}} \tag{2.19}$$

$$\frac{\partial W_L}{\partial t} + \vec{\nabla}\cdot\vec{S}_L = \left.\frac{dW_L}{dt}\right|_{\mathrm{coll}} + \vec{J}_n\cdot\vec{\nabla}E_C + \left.\frac{dW_n}{dt}\right|_{\mathrm{coll}} + \vec{J}_p\cdot\vec{\nabla}E_V + \left.\frac{dW_p}{dt}\right|_{\mathrm{coll}} \tag{2.20}$$

$$\vec{S}_n = -\frac{5r_n\lambda_n}{2}\left(\frac{k_B T_n}{q}\overrightarrow{J_n} + f_n^{hf} k_n \vec{\nabla} T_n\right) \tag{2.21}$$

$$\vec{S}_p = -\frac{5r_p\lambda_p}{2}\left(-\frac{k_B T_p}{q}\overrightarrow{J_p} + f_p^{hf} k_p \vec{\nabla} T_p\right) \tag{2.22}$$

$$\vec{S}_L = -k_L \vec{\nabla} T_L \tag{2.23}$$

$$k_n = \frac{k_B^2 n \mu_n T_n}{q} \tag{2.24}$$

$$k_p = \frac{k_B^2 p \mu_p T_p}{q} \tag{2.25}$$

Equations (2.13) and (2.14) represent the conduction and valence band edges. The current densities are given by equations (2.15) and (2.16), where T_n and T_p are the carrier temperatures whereas E_C and E_V are the conduction and valence band potentials, respectively. The first two terms take into account the contribution due to the spatial variations of electrostatic potential, electron affinity, and the energy bandgap. The three left terms take into account the contribution due to the gradient of concentration, the carrier temperature gradients, and the spatial variation of the effective masses m_e and m_h. For Fermi statistics, γ_n and γ_p are given by $\gamma_n = n\exp(-\eta_n)/N_C$ and $\gamma_p = p\exp(-\eta_p)/N_C$, with $\lambda_n = F_{1/2}(\eta_n)/F_{-1/2}(\eta_n)$ and $\lambda_p = F_{1/2}(\eta_p)/F_{-1/2}(\eta_p)$ and, $\eta_n = (E_{F,n} - E_C)/(k_B T)$, $\eta_p = (E_V - E_{F,p})/(k_B T)$. $F_{1/2}$ and $F_{-1/2}$ are the Fermi integral of order ½ and -½, respectively. For Boltzmann statistic, $\gamma_n = \gamma_p = \lambda_n = \lambda_p = 1$.

The energy balance equations are given in equations (2.17) and (2.18) while equations (2.21) to (2.23) represent the energy flux [54]. f_n^{hf} and f_p^{hf} are the coefficients for heat flux, f_n^{td} and f_p^{td} are the coefficients for thermal diffusion, r_n and r_p are the coefficients for energy flux.

The drift-diffusion carrier transport model takes into account carrier velocity and lifetime, bias voltage, and optical field intensity, while the hydrodynamics carrier transport also takes into account carrier temperature

dependent parameters such as mobilities and diffusion coefficients and thereby models more accurately the carrier transport.

The DDCTM is valid as the absorption and collection layers lengths ($L_a = 220$ nm and $L_c = 263$ nm) are too lower when compared with their respective electron-phonon scattering lengths ($L \gg L_{e-ph}$, $L_{e-ph,a} \cong 16$ and $L_{e-ph,c} \cong 7.9$ nm, respectively) [79]. The HDCTM is valid as the length device are too lower when compared with the electron-electron scattering length ($L \gg L_{e-e}$). Under this situation, the simulation is valid because the absorption and collection layer lengths ($L_a = 220$ nm and $L_c = 263$ nm) are too larger when compared with their respective electron-electron scattering lengths ($L_{e-e,a} \cong 1.3$ nm and $L_{e-e,c} \cong 1.0$ nm) [79]. See Appendix C to see the procedures used in the computing of the different relevant scattering lengths.

2.1.3. Numerical results from DD and HD Model

This section will show several simulation results using the drift-diffusion and hydrodynamic model of the InGaAs/InP UTC-PD structure shown in Table 2.1. DC simulations were performed under different input optical power. Figure 2.2 shows the responsivity curve for the 3 and 10 μm diameter cylindrical devices. Figure 2.2 also shows also the responsivity curve reported in reference [80], which is a 5-μm diameter cylindrical device. The responsivity is a common measure of the photodetector performance, which is defined as the ratio of the photocurrent to the optical intensity (see equation (1.2)). The InGaAs/InP UTC-PD responsivity was also investigated by varying the optical intensity from 5×10^3 W/cm^2 to 1×10^7 W/cm^2, under an applied reverse voltage of 2 V. Under low-level illumination, the 10-μm InGaAs/InP UTC-PD device presents a responsivity of 0.13 A/W, and the 3-μm InGaAs/InP UTC-PD device present a 0.17 A/W. With high-level illumination, the 10-μm InGaAs/InP UTC-PD device responsivity falls abruptly at 5×10^5 W/cm^2, while the 3-μm InGaAs/InP UTC-PD device responsivity falls at 3×10^5 W/cm^2. Therefore, the devices with greater surface supports higher optical intensity but with lower responsivity. The 3-μm and 10-μm diameter LE-UTC gives maximum of responsivity values of 0.2 and 0.14 A/W, respectively. These values are not far from 0.25 A/W reported by Mahmuddur Rahman et al [80], performing

hydrodynamic simulations with a 5-μm-diameter LE-UTC photodiode. Figure 2.3 shows the same as Figure 2.2, but with the optical input expressed in W.

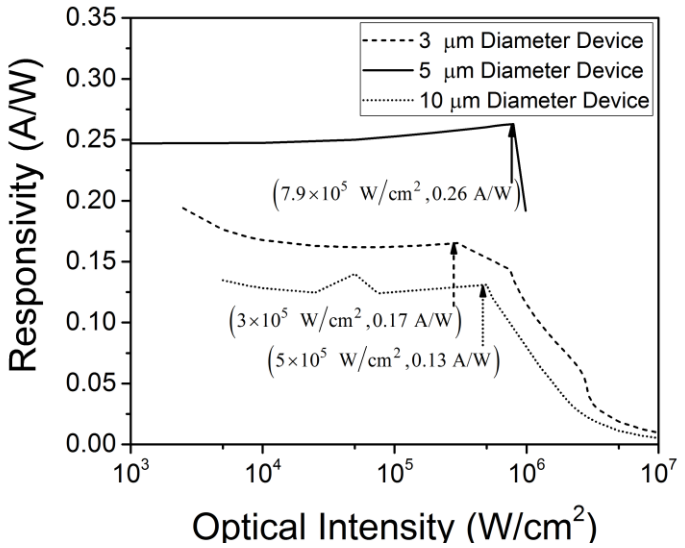

Figure 2.2. Plot of responsivity of the LE-UTC photodiode versus optical intensity for the 3, 5, and 10 μm diameter under an applied reverse bias of 2 V. The results for the 5-μm LE-UTC were taken from reference [80]

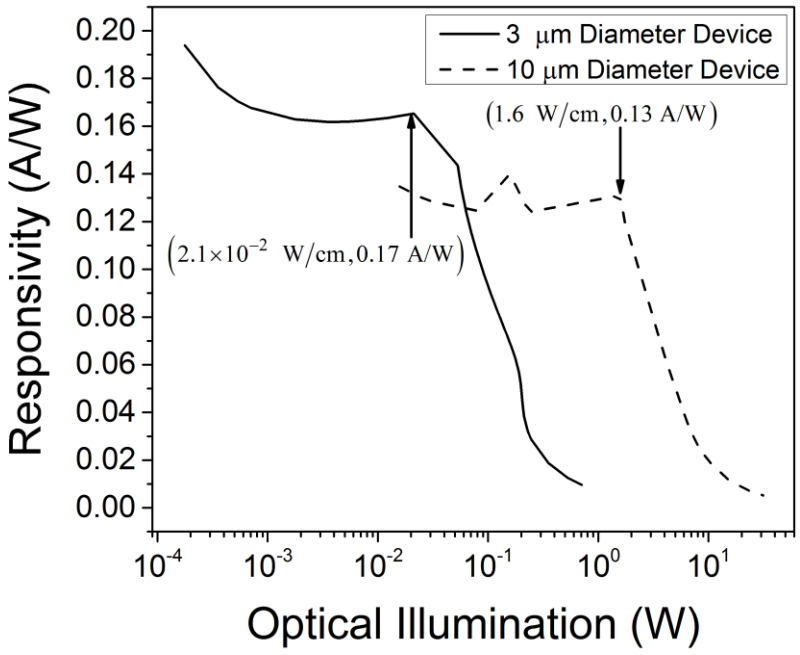

Figure 2.3. Responsivity of the InGaAs/InP UTC-PD device versus optical intensity for for a 3 and 10 μm diameter device under a reverse bias of 2 V.

For the sake of simplicity and the purpose of this thesis, a definition of curvature is given here. The curvature is the reciprocal of the radius of a circle. Therefore, the curvature of a circle of radius R is small if R is short and small if R is long. Following this, one says, the higher is the curvature, more is the bending. Figure 2.4 shows the energy band diagrams for a 3 μm diameter UTC-PD device under different optical injection levels at a reverse bias of 2 V. Figure 2.4 also shows the distance corresponding to the absorption, cliff, and collection layers. Under low-level optical-input injection (optical injection with values lower than $1 \times 10^5\ W/cm^2$), the curvature value of the collection bandgap is practically zero (no bending). Under high-level optical-input injection, this value increases (bending start to appears). This band-bending phenomenon is in agreement with published results [81]. An interesting feature of this bending appears as the optical intensity increases from $2.5 \times 10^6\ W/cm^2$ to $1 \times 10^7\ W/cm^2$: the curvature value decreases making the collection bandgap practically linear. This behavior suggests that the cliff layers as the main cause why the energy bandgap deviates that much from its shape under low-level optical-input injection. In the following, more results will be shown to support this conjecture The cause of this behavior appears to happen in the cliff-layers, where first a reduction of the gradient and then a reversal of the electrical field occurs for the electrons in the conduction band (but only a minor reduction for

the holes in the valence band) as the optical intensity is increased to the highest value of $1 \times 10^7\ W/cm^2$ [50]. Until $10^4\ W/cm^2$ only marginal changes occur.

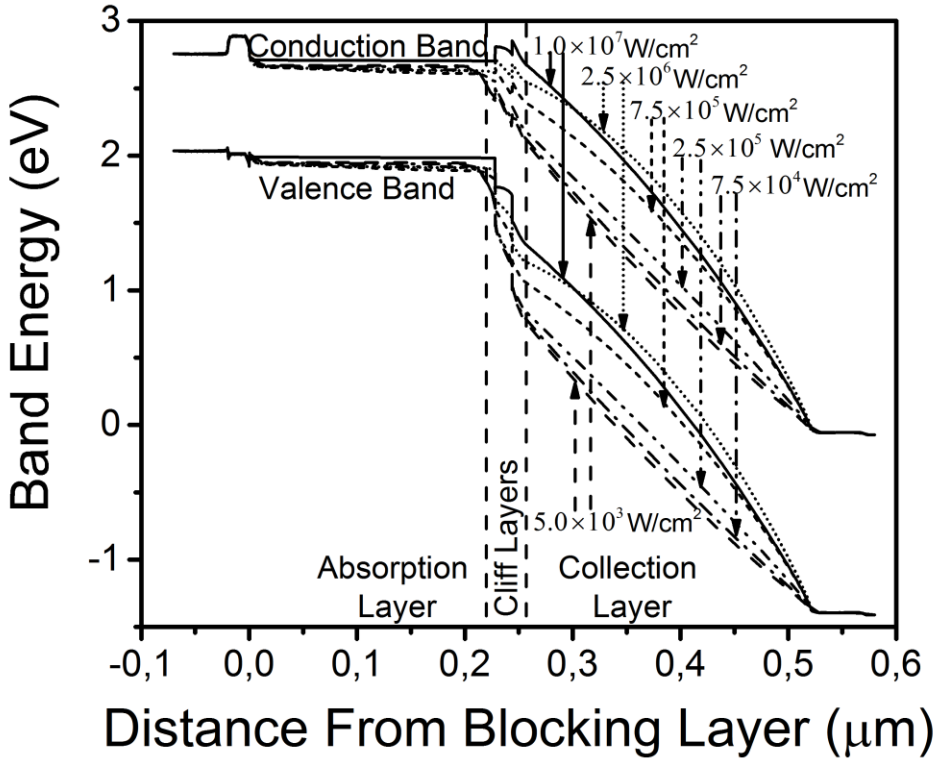

Figure 2.4. Energy band-diagram for different optical injection levels, the line style matches the optical intensity for each curve for both, the valence and conduction bands.

To understand better this reduction in the electrical field, the electric field profile is shown in Figure 2.5 for different optical intensities with an applied reverse bias of 2 V. Figure 2.5a) shows the calculated electric fields for optical intensities between 5×10^3 and 5×10^5 W/cm^2. Figure 2.5b) shows the calculated electric fields for optical intensities between 5×10^5 and 1×10^7 W/cm^2. The electric field is nearly zero in the heavily doped absorption and subcollector regions, it peaks at the junctions between the p-contact and block layers, block layer and absorption layer, absorption layer and cliff layers, and between the collection and subcollector layers.

At low light levels, the electric field inside the cliff layers, as shown in Figure 2.5a), is higher than present at high light levels as shown in figure Figure 2.5b). To understand better, the nature of this decreasing electric field inside the cliff layers when a strong optical input is applied, Figure 2.6 shows the space charge vs distance plot. When the light conditions change from low

to high level, the space charge inside the cliff layers increases strongly. This is explained by the accumulation of electrons around the pikes present at the cliff layer energy bandgap.

Under low light levels (between 5×10^3 and 7.5×10^4 W/cm^2) (see Figure 2.5a), the electric field inside the collector layer has a negative slope. When the optical intensity is increased again to 5×10^5 W/cm^2, the slope of the electric field inside the collector layer changes from a slightly negative to a slightly positive value. During this increasing optical intensity, the electric field inside the cliff layers is clearly lower and its maximum peak decreases from 1.5×10^5 to 1.2×10^5 V/cm. For high light levels (between 5×10^5 and 1×10^7 W/cm^2), the slope of the electric field inside the collector retains its positive value, leaving the electric field fixed at the collection layer end and increasing their its value close the cliff layers as shown in Figure 2.5b. At high light levels also accentuates the decreasing nature of the electric field inside the cliff layers as showed in Figure 2.5b. This behavior can be explained with the help of Figure 2.7, which shows the electron density vs distance present along the structure layer of the UTC-PD device. For low light levels (up to 7.5×10^4 W/cm^2), the electron density is similar in value in both layers, the absorption and collection layer. Under this condition, the electric field has a positive slope as shown in Figure 2.5a). With optical intensities larger, like 5×10^5 W/cm^2, the electrons start to accumulate at the absorption layer changing the space charge profile. To explain this behavior, the conjecture that the band bending is due to the cliff layers, as proposed in Figure 2.4, will be resumed. Observing the cliff layers in Figure 2.7, the electron density has values similar to those from the absorption and collection layers under conditions of low-level lights. Under high-level light conditions, the accumulation of electrons in the cliff layer is greater than the electron density at the absorption and collection layers having an effect of electron trapping at the absorption layer. Therefore, the space charge effect is strongly influenced by the cliff layers. This suggest a route in improving future UTC-PD devices by engineering the cliff layers in order to smooth the transition between absorption and collection layer. One possibility is the Other way to do improvement in the UTC-PD devices is the suggestion of a homojunction between the absorption layer to suppress the cliff layers making the transition totally smooth, but this is not possible because it is needed to avoid electron-hole generation inside the collection layer. This is, the collection layer needs to be completely transparent to the wavelength of operation. A third way to solve this issue was the use of a staggered heterojunction (type II). The lattice-matched $GaAs_{0.51}Sb_{0.49}$ instead of $In_{0.53}Ga_{0.47}As$ in the UTC-PD absorption layer was used [82]. The GaAsSb absorbing layer conduction band edge lines up $\Delta E_C = 0.11$ eV above that of InP, making a type-II heterojunction with the InP collection layer. This allows

avoiding the compositional grading layer between the absorption and collection layer simplifying the UTC-PD final structure and suppressing the conduction band energy peaks between the absorption and collection layer of the InGaAs-InP UTC-PD [82]. Therefore, space charge limitation is suppressed.

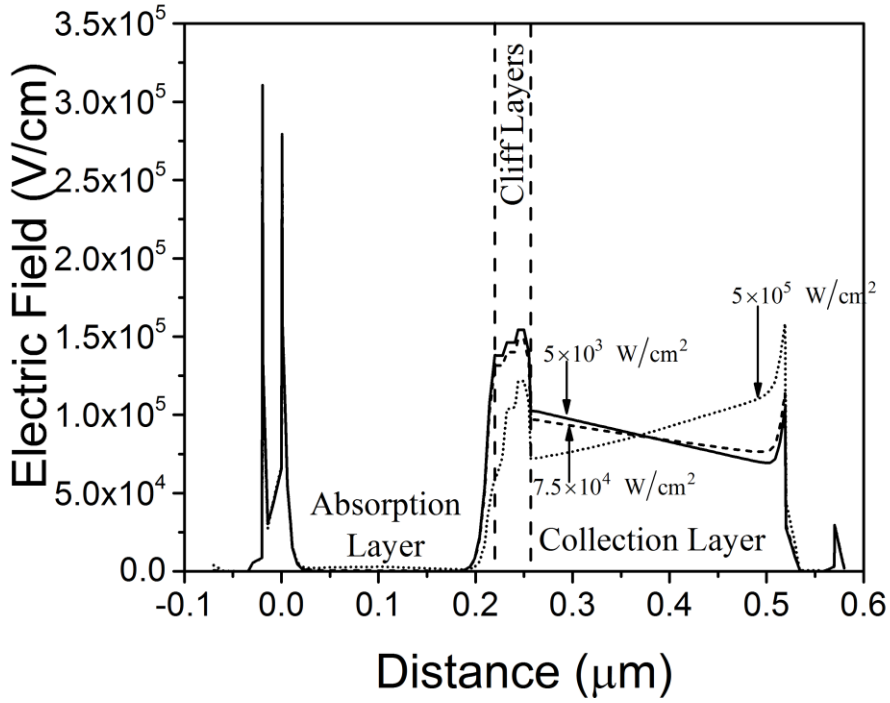

a)

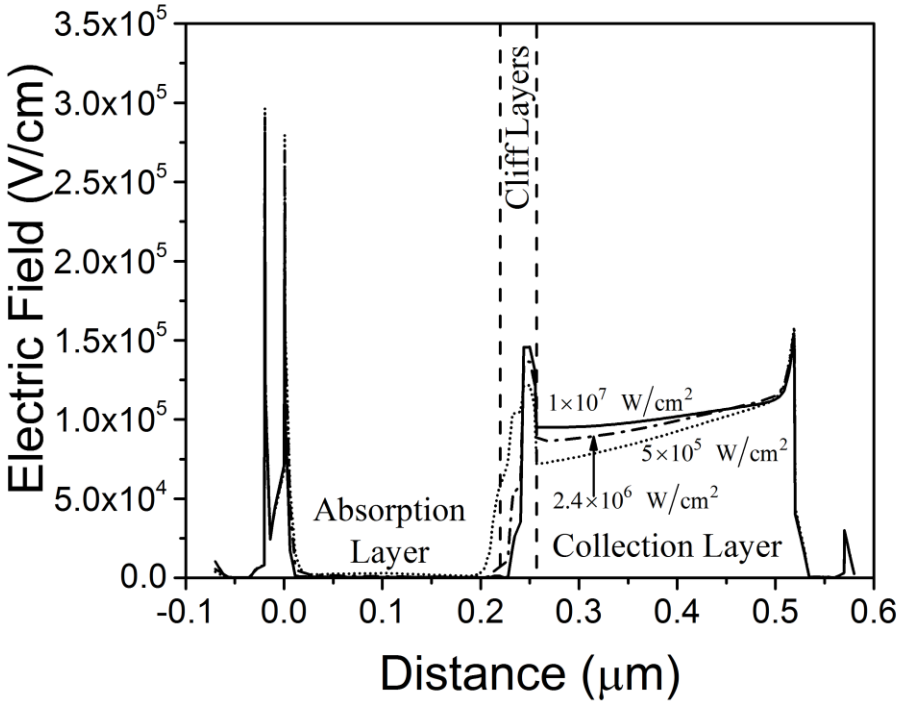

b)

Figure 2.5. Electric field under different optical power. a) Optical intensities from 5×10^3 and 5×10^5 W/cm^2. b) 5×10^5 and 1×10^7 W/cm^2.

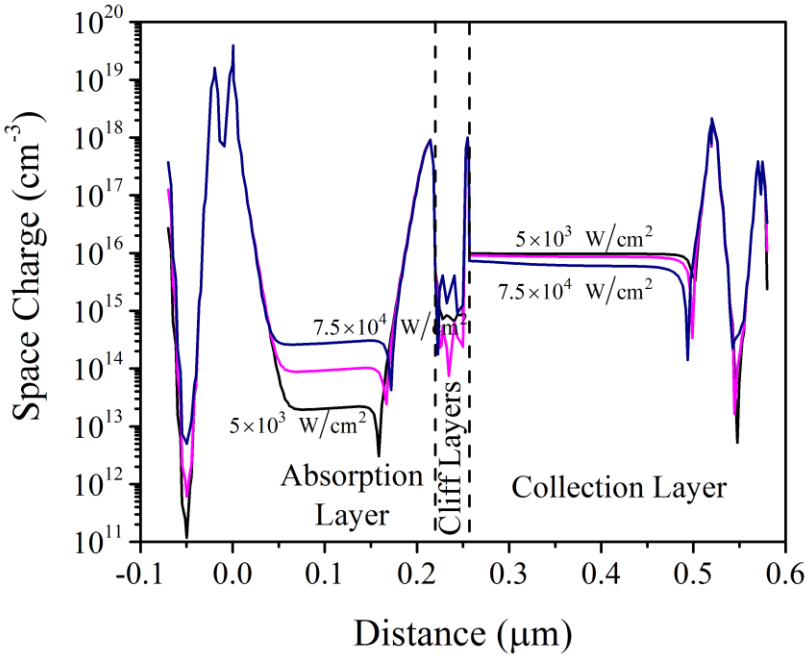

a)

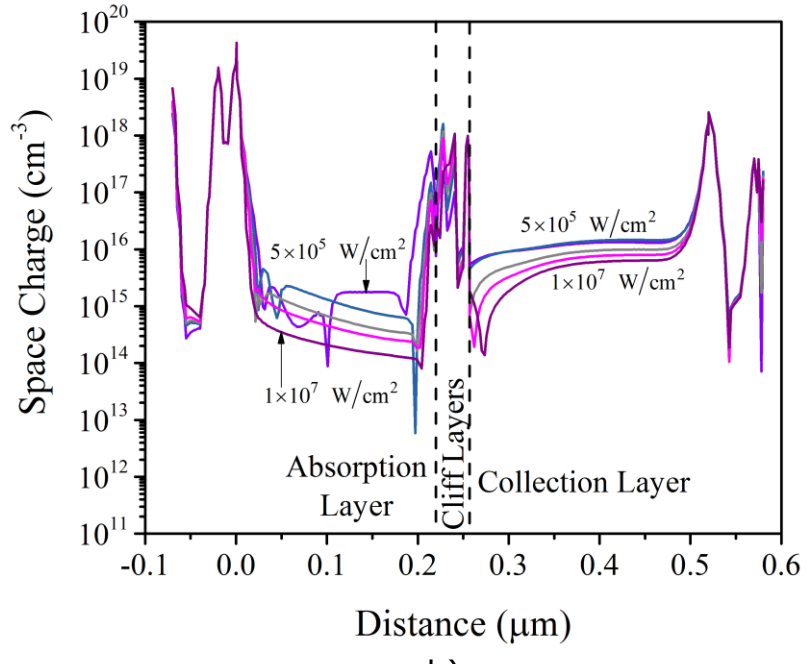

b)

Figure 2.6. Space charge under different optical power. a) Optical intensities from 5×10^3 to 7.5×10^4 W/cm^2. b) from 5×10^5 to 1×10^7 W/cm^2.

At enough high optical power levels, the space-charge-induced electric field is strong enough to collapse the external electric field. This leads to a decrease in the transit time (and corresponding decreasing in bandwidth), a

reduction in the saturation photocurrent. The number of photogenerated carriers that travels through the UTC photodiode also increases enough to increase the space charge inside the cliff layers. This leads to a screening effect on the electrons traveling across the device, decreasing the saturation photocurrent and electron velocity (decreasing in bandwidth).

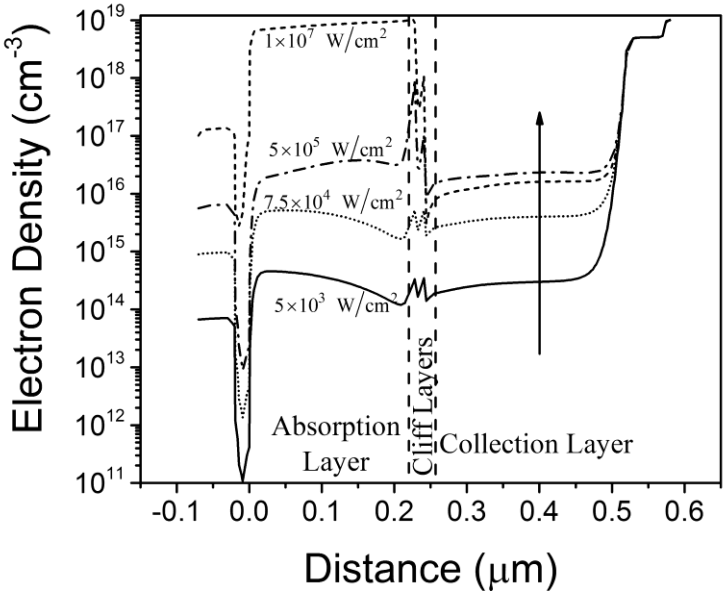

Figure 2.7. Electron density versus distance under different optical intensities.

Figure 2.8a shows curves of electron velocity against the distance measured from the block layer. Three plots are presented, two resulted from the HDCTM and, the other plot from the Drift-Diffusion Carrier Transport Model (DDCTM). The simulated DDCTM plot was compared with the reported by Rahman et al [80], and they are exactly the same results. Then, only one DDCTM plot was depicted in Figure 2.8a. The HDCTM predicts velocity overshoot, which is observed in Figure 2.8a when this is compared with the results from the DDCTM. The velocity overshoot is present because the DDCTM only predicts a saturated velocity [80]. The physical origins of the velocity overshoot is shown in Figure 2.9. This figure shows the measured electron drift velocity versus the applied electric field for InGaAs. In low electric field regime (0-1 kV/cm), the electron velocity increases proportional to the electric field. This region has a linear dependence a represented by the dashed line. In this electric field regime, the conduction electrons are in the high-mobility energy minimum (called a valley) represented by the lower valley (see inset 1). If the electric field is increased more than the electric linear regime, the electric field delivers an additional energy ΔE to the conduction electrons. As a result, the

electrons are transferred to the upper valley, where the electron mobility is lower (see Figure 2.9, inset 2) [83, pp. 73–75].

An interesting feature shown by our simulation, which is presented in Figure 2.8a, is the electron overshoot appearing at the absorption layer, contrary to the prediction by the DDCTM, which guesses a lower electron velocity. The electron velocity starts increasing in the absorption layer and it almost reaches a maximum velocity of 4×10^7 cm/s value close the cliff layers. This is explained in Figure 2.10 and Figure 2.9. Figure 2.10 is a plot of Electric field vs distance like Figure 2.5. The difference is the vertical axis are limited between 0 and 4 kV/cm to zoom the electric field at the absorption layer. The electric field has values that go from 2.5×10^{-2} to 3 kV/cm, and according to Figure 2.9, the electron energy falls in the lower valley where the electrons have the highest mobility. Therefore, velocity overshoot occurs in the absorption layer. The electron velocity starts with its maximum value decreasing as the electron travels along the collection layer. This lower velocity is explained qualitatively in Figure 2.9. According to Figure 2.5, the collector electric field values oscillates around 65 and 160 kV/cm, which means that the electrons operate in the electron-velocity saturated regime. Therefore, the electrons populate completely the upper valley with lower mobility. Additionally, the electron velocity shows a monotonically decrease in the collection layer, according to our results. This is explained qualitatively with the help of the Figure 2.8b. Figure 2.8b shows the electron temperature versus the distance. The maximum electron temperature appears to be at the collection layer. The electron temperature is a measurement of the kinetic energy of the electrons. It is clearly that the maximum electron kinetic energy appears across the collection layer.

A comparison between Figure 2.8a and Figure 2.8b, our simulation shows an apparently contradiction between the electron velocity and the kinetic energy of the electrons, because the absorption layer presents the maximum electron velocity, the electron temperature is the lowest among the whole structure. Contrary to this, the collection electron velocity is decreasing and has the highest electron temperature. This is explained qualitatively in the following manner. At any finite temperature above the absolute zero, the free electrons are in a random motion inside the lattice, and due the imperfections originated in the thermal lattice vibration, the electrons are colliding with the lattice atoms. The average of all the free paths taken by the electrons between successive collisions is the mean free path, l, and associated with this value is the mean free flight time, τ, which is calculated as $\tau = l/v_T$, where $v_T = \sqrt{2k_BT/m_e}$ is the thermal velocity of the electrons, k_B is the Boltzmann's constant, m_e is the electron mass (9×10^{-28} g), and T is the absolute

temperature taken a room temperature (usually taken at 300 K, the room temperature). The mean free flight time is interpreted as the time for which an electron is allowed to freely accelerate and build up a superposed velocity (over and above its thermal velocity) and hence a superposed displacement. When a small electric field is applied, the electrons receive an additional energy, it is shared with the lattice in the form of collisions. Anyway, the probability of a collision and the mean free time, τ, are not affected by this small increase in electron velocity. However, when the electric field applied to a semiconductor is increased significantly (higher than 69 kV/cm), the electron velocity between two successive collisions inside the collection layer is increased significantly over the thermal velocity v_T according Figure 2.5. Therefore, the probability of the electron encountering a collision increases, leading to a reduction of mean free flight time (τ) and electron mobility μ_n [77]. As the electric field becomes more intense, the number of collisions increases, implying that the charge carriers increase the intensity of their interaction with the lattice potential, and that means that they become heavier. Therefore, their kinetic energy is increased by increasing the electron mass from the standpoint of the system, but their velocity is lower.

The first difference is the higher electron velocity inside the block layer. But, this has to be discarded because its role is to block the electron passing through this layer. Therefore, there is not a physical meaning off the electron velocity magnitude inside this layer. This thesis also reports a slightly higher electron velocity across the absorption layer than the reported by Rahman et al. Therefore, there is not a significant difference between them. Across the collection layer, the physical behavior is different. According to Rahman et al, the electron velocity starts decreasing up to reaching a minimum at some position of the collection layer. After this position, the electron velocity starts to increase its magnitude reaching a new local maximum to decrease after reaching such position. This thesis reports a different physical behavior for the electron velocity across the collection layer. In this case, the electron velocity starts with a maximum at the beginning of the collection layer. After this maximum, the electron velocity is always decreasing. A comparison between Figure 1.5 and Figure 2.5 justify this behavior. Figure 2.5 shows that the maximum velocity appears when the electric field is about 13 kV/cm (for InP, because this is the collection layer material), while the electric field inside the collection layer has values higher than the electric field for the maximum electron velocity of the InP materials. This means that the electron velocity has to be valued lower than the maximum electron velocity at the collection layer, and looking the electron temperature in Figure 2.8b, the number of collisions of electrons inside the collection layer should be the highest among

the whole UTC photodiode. Therefore, the electron velocity has to be a decreasing fashion at the collection layer.

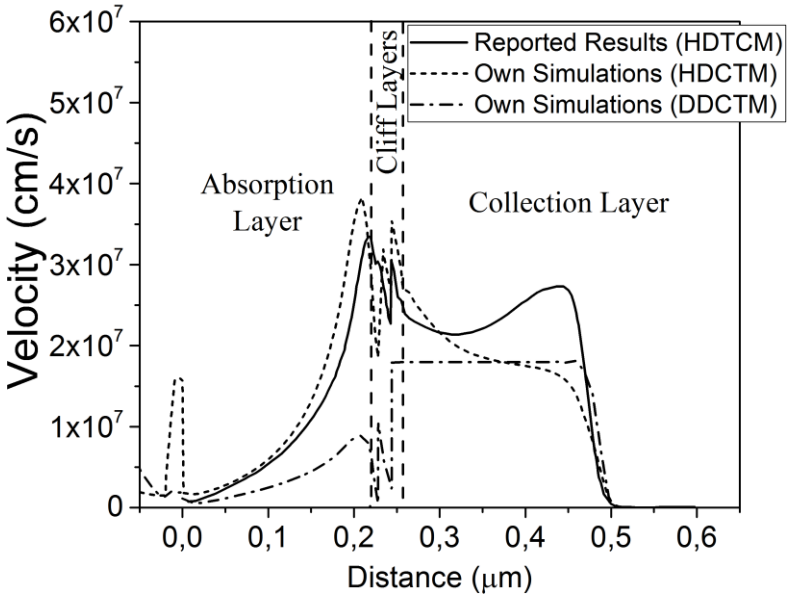

a)

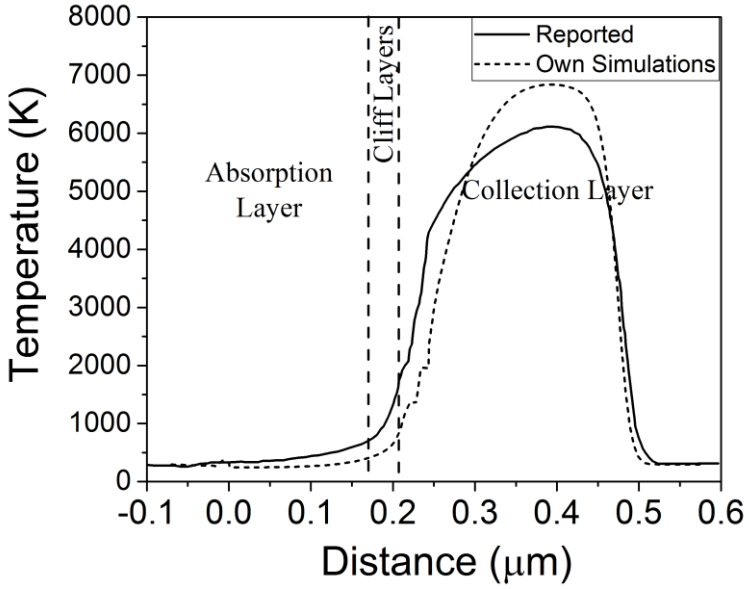

b)

Figure 2.8. a) Electron velocity distribution where the reported results were obtained from S.M. Mahmudur Rahman et al [80], and b) electron temperature across the UTC-PD at a 2 V reverse bias and optical intensity of 5000 W/cm^2, also compared with the reported results in reference [80].

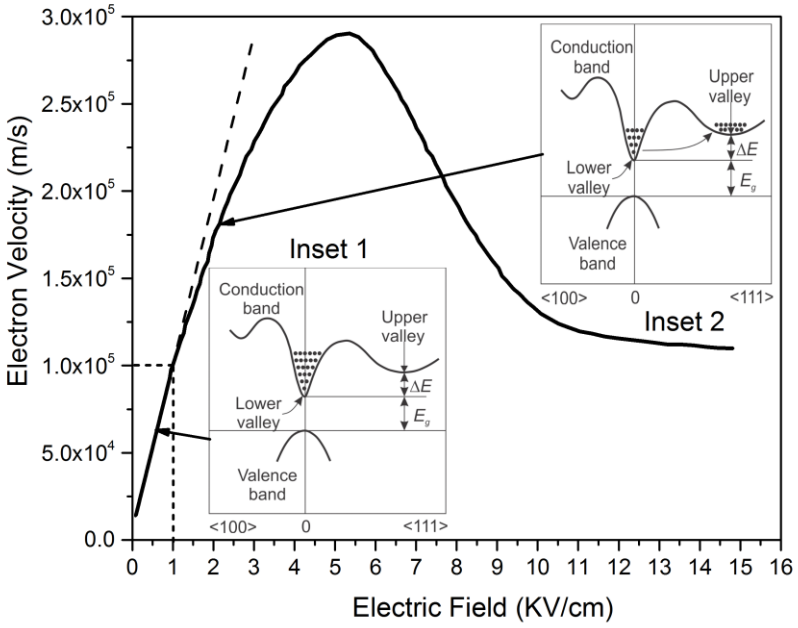

Figure 2.9. Physical principle of the transferred-electron effect: The main plot shows the Electron velocity vs the applied electric field. The linear dashed shows the linear region where the electron velocity behaviors linearly. Under this situation the electrons remain in the lower valley (inset 1). At electric field values higher than 1 kV/cm, the electrons start to transfers from the lower valley to the upper valley represented in the figure inset 2 [76].

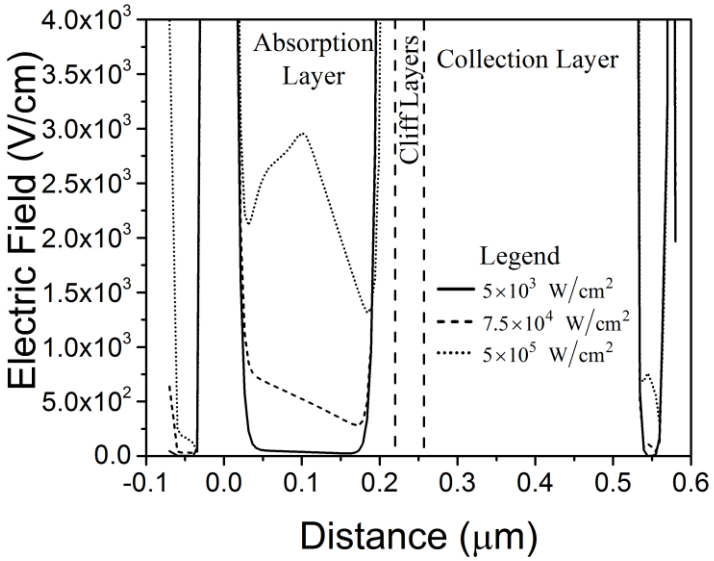

Figure 2.10. Electric field versus distance under different applied optical intensities. This plot corresponds to figure Figure 2.5a, but with a vertical axis scale between 0 and 4×10^3 V/cm, to focus on the electric field inside the absorption layer.

Despite there are simulation results, the results here presented are really reported results [80], and therefore not relevant to publish. The initial goal was simulating different layers' thickness to study the performance behavior, and also the transient, and AC response of the LE UTC devices but they were not possible due to numerical convergence.

3. RF Electromagnetic Modeling

RF electromagnetic modeling is used in general as design tool, but in this thesis, the purpose of RF electromagnetic modeling is to understand the THz losses from physical principles. Therefore, by the help of RF electromagnetic modeling tools, it is expected to be understood the influence of THz losses in VI-TW-UTC photomixers. This chapter will give a short review about the time-domain modeling and the corresponding tool used for this purpose. This will give also a short explanation about the tool used for the frequency domain modeling.

3.1. Time-domain modeling (CST Microwave Studio)

The Transient solver used in CST Microwave Studio is based on the Finite Integration Technique (FIT). It applies highly advanced numerical techniques like the Perfect Boundary Approximation (PBA)® in combination with the Thin Sheet Technique™ (TST) to allow accurate modeling of small and curved structures without the need for an extreme refinement of the mesh at these locations. This allows a memory-efficient computation together with a robust hexahedral meshing to successfully simulate extremely complex structures. The fields are calculated step by step through time by the "Leap Frog" updating scheme [85]. It is proven that this method remains stable if the step width for the integration does not overcome a known limit. This value of the maximum usable time step is directly related to the minimum mesh step width used in the discretization of the structure. Therefore, a denser means a smaller time step size [86].

3.2. Frequency domain modeling (HFSS)

To calculate the full three-dimensional electromagnetic field inside a structure and the corresponding S-parameters, HFSS employs the finite element method (FEM) [87]. FEM is a very powerful tool for solving complex engineering problems, the mathematical formulation of which is not only challenging but also tedious. The basic approach of this method is to divide a complex structure into smaller tetrahedral sections known as finite elements. These elements are connected to each other via joint scaled nodes. Each unique element is then solved independently of the others thereby drastically reducing the solution complexity. The final solution is then computed by reconnecting all the elements and combining their solutions. These processes are named assembly and solution respectively in the FEM [87]. FEM finds applications not only in electromagnetics but also in other branches of engineering such as plane stress problems in mechanical engineering, aerodynamics and heat transfer.

FEM is the basis of simulation in HFSS. HFSS divides the geometric model into a large number of tetrahedral elements. Each tetrahedron is composed of four triangles and the collection of tetrahedral forms what is known as the finite element mesh. Figure 3.1 shows the finite element mesh for a sample horn antenna. This figure was taken from [87]. At each vertex of the tetrahedron, components of the field tangential to the three edges meeting at that vertex are stored. The other stored component is the vector field at the midpoint of selected edges, which is also tangential to a face and normal to the edge. Using these stored values, the vector field quantity such as the H-field or the E-field inside each tetrahedron is estimated. A first-order tangential element basis function is used for performing the interpolation. Maxwell's equations are then formulated from the field quantities and are later transformed into matrix equations that can be solved using traditional numerical techniques.

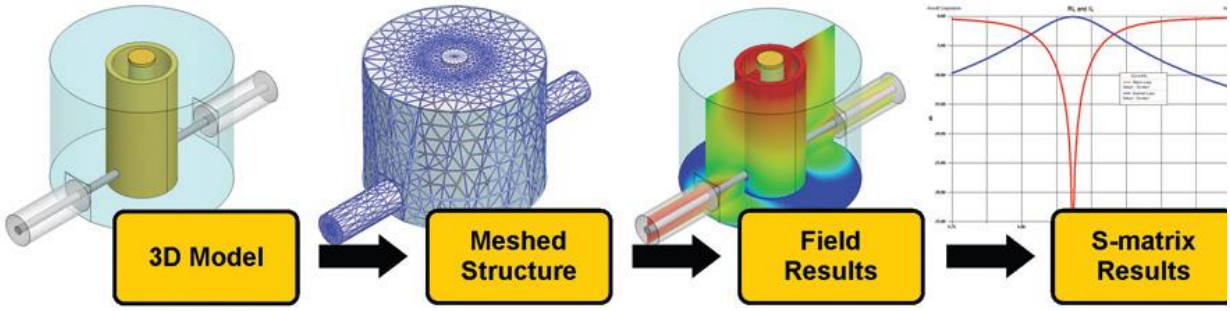

Figure 3.1. Procedure used by HFSS in order to solve an electromagnetic problem [87].

3.3. Electromagnetic simulation results for TW-mixer structures in different simulators

3.3.1. Port-to-Transmission-line transmission losses and impedance matching

The procedure used to get the best value for the characteristic impedance Z_0 of the CPW at which the power from port 1 is transferred best to the waveguide, and extracted from it in port 2 is shown in Figure 3.2. We start by giving an arbitrary and reasonable initial input Z_0 value at the device shown in Figure 3.10. The simulations were performed in the time domain (see Figure 3.4b), then the smith chart with the scattering S_{11} parameter for each conductivity is created and inspected. If the S_{11} curve is far from the intersection between the $Z_0 = 1$ circle and the horizontal axis, a new value for Z_0 is proposed and then simulated. This is repeated up to find the Z_0 value for which the S_{11} curve is the closest to the intersection between the $Z_0 = 1$ circle

and the horizontal axis (see Figure 3.3). This procedure and its results are shown in Figure 3.4. The program CST Microwave Studio™ was manually stopped after the seed pulse coupled in completely.

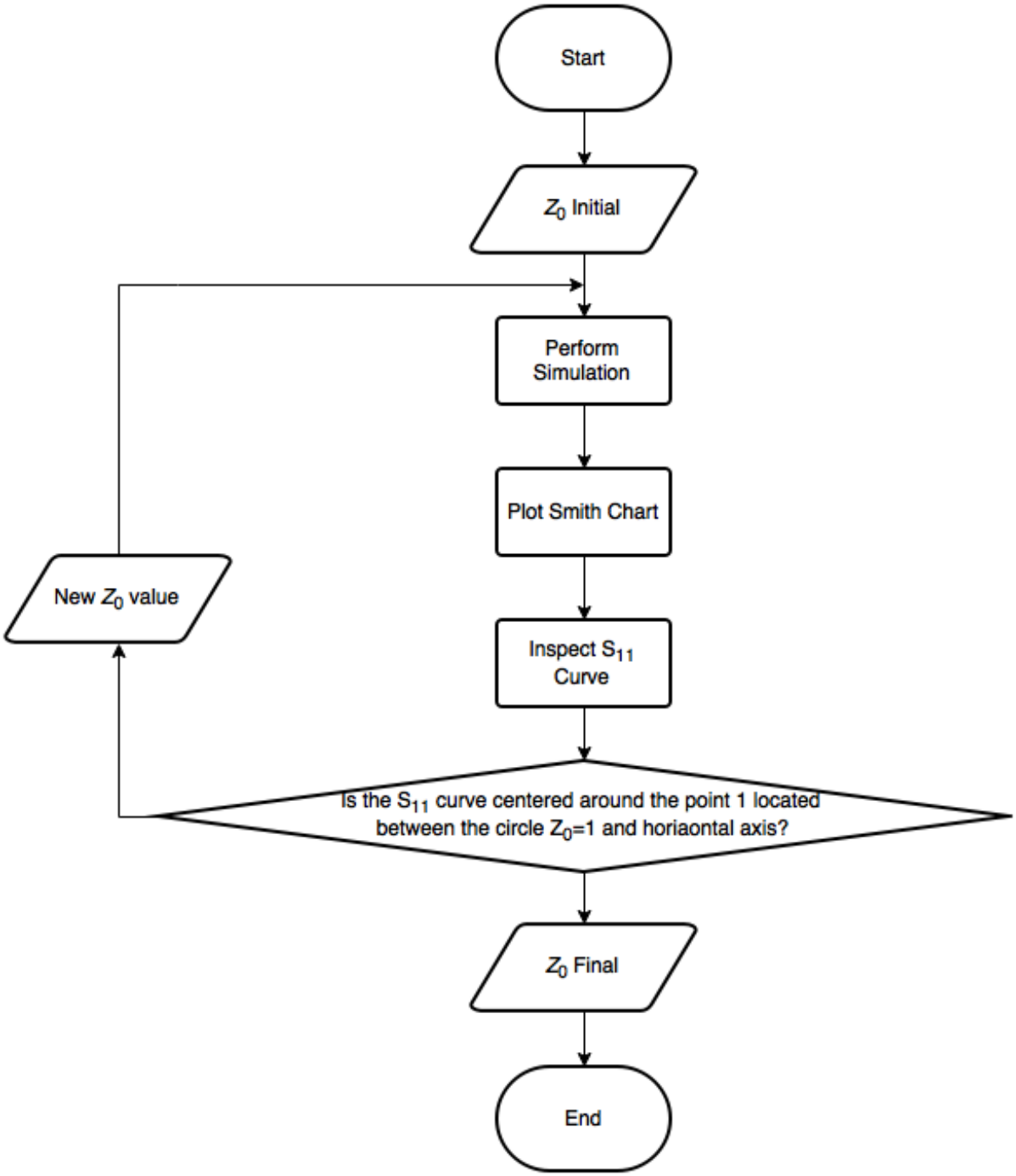

Figure 3.2. Flowchart diagram explaining the procedure to get the best characteristic impedance of the transmission line by simple visual inspecting of the Smith Chart.

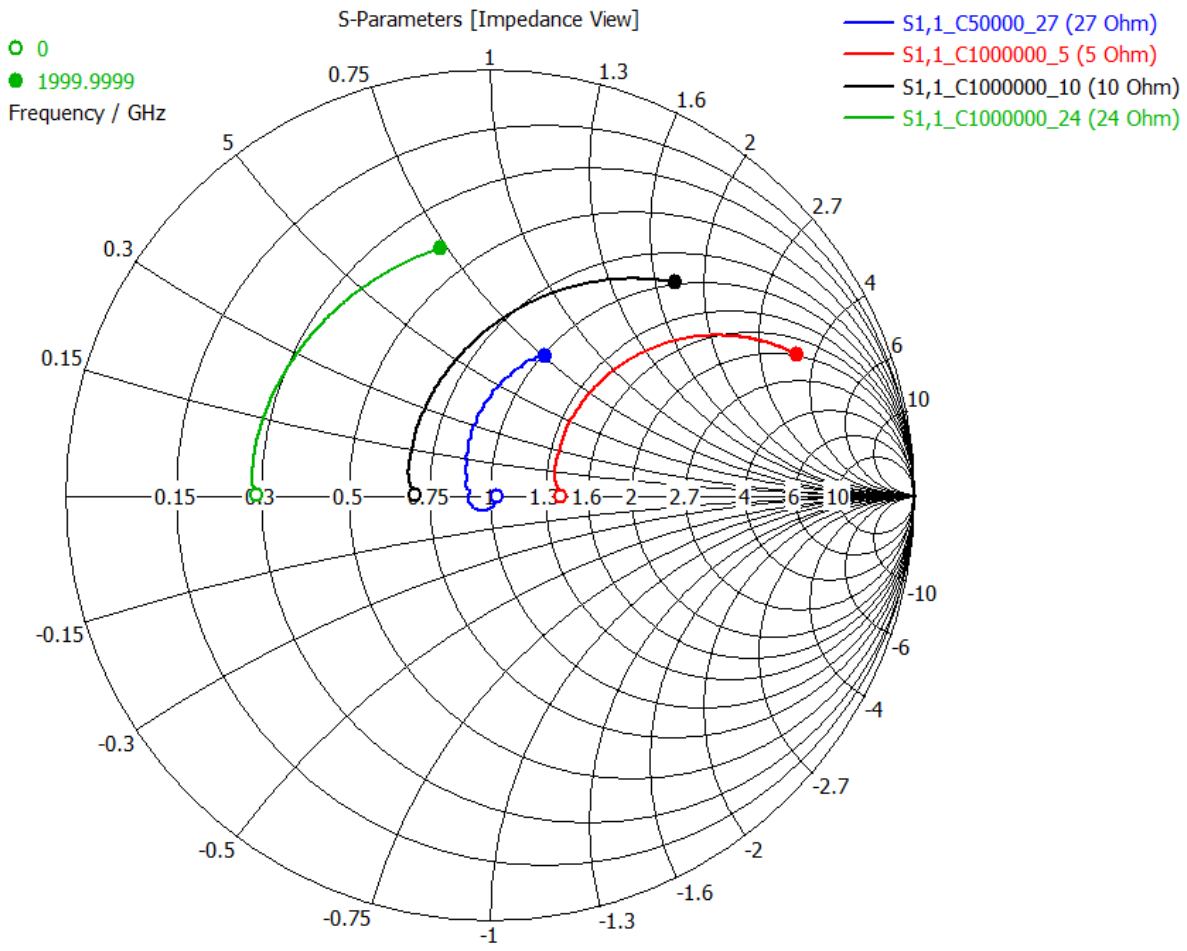

Figure 3.3. Smith chart showing the results of the procedure depicted in Figure 3.2.

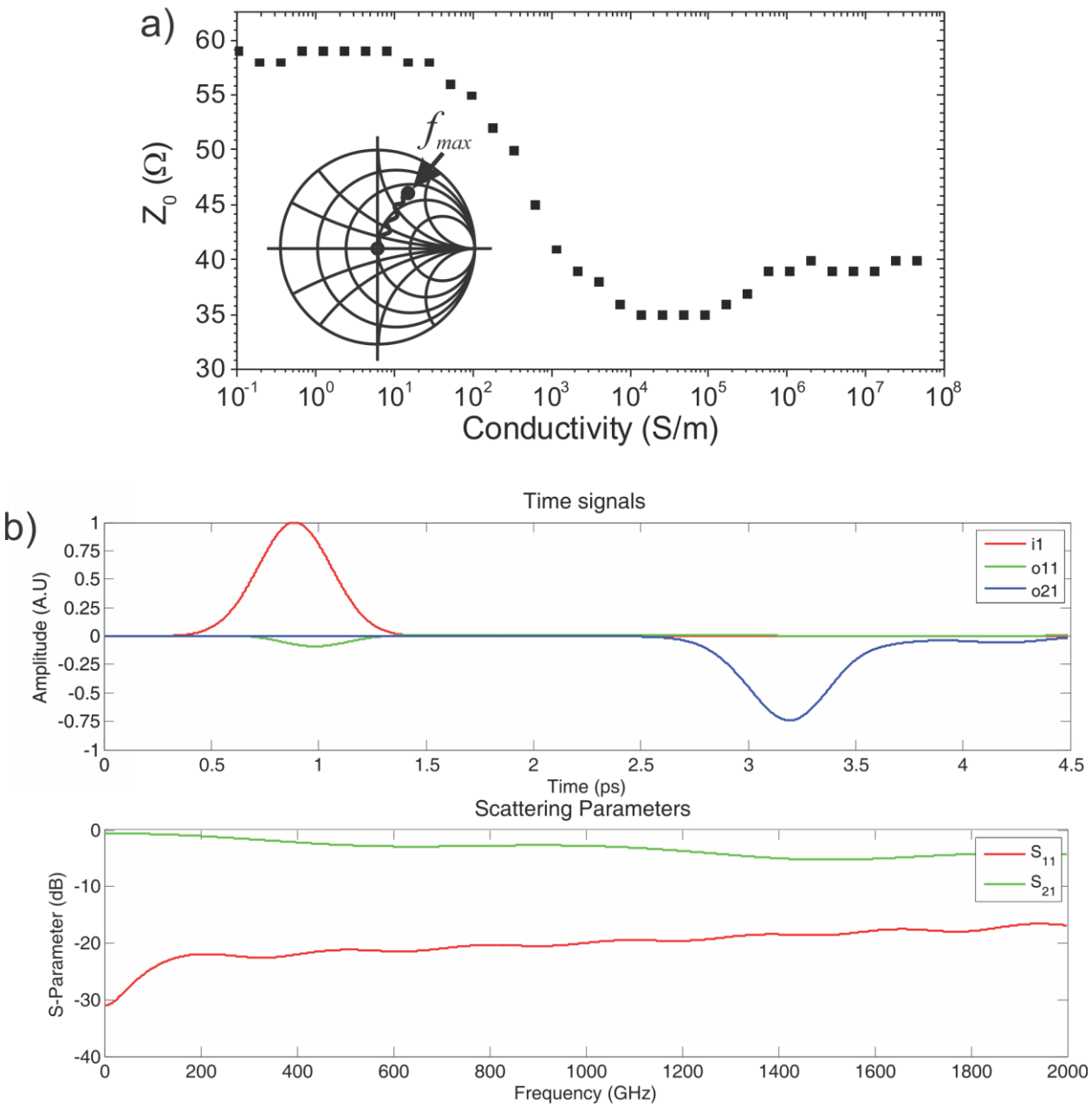

Figure 3.4. a) Port 1 impedances versus conductivity determined by centering the Smith chart (left inset) using CST Microwave Studio™ in the pulsed domain with a frequency range of $0 - \mathrm{f}_2$, with $\mathrm{f}_2 = 1, 2,$ or $4000\ \mathrm{GHz}$. There was the problem that the reflected pulse was not anymore Gaussian for $\mathrm{f}_2 > 1000\ \mathrm{GHz}$ in b). These values were confirmed in HFSS™.

3.3.2. Dependence of the dark THz-absorption on the base n-layer conductivity

Two types of waveguides have been used for sub-mm and THz generation. The first type of waveguide consists of planar metal-semiconductor-metal (MSM) CPS for (non-polar) one-layer photoconductors where the electron-trap phenomenon dominates (e.g. LT-GaAs). The second type of waveguide illustrated in Figure 3.5(a) and (b), is a coplanar waveguide (CPW) for polar vertical (mesa) photodiode semiconductor structures where the transit time phenomenon dominates (e.g. the InGaAs/InP system). In this second case, the mesa structure is contained under the central stripline.

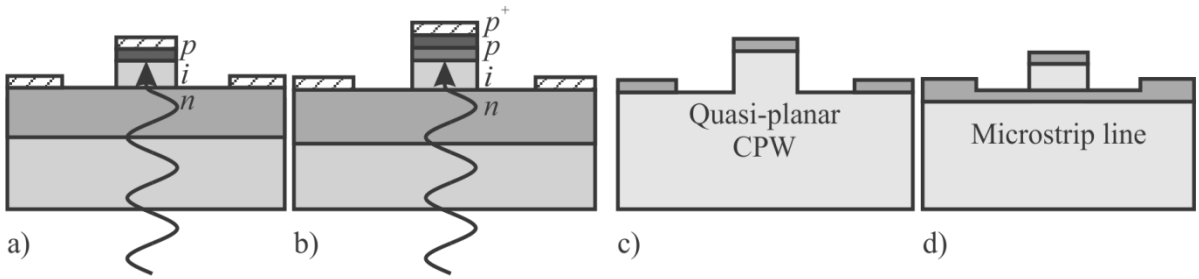

Figure 3.5. Photodiodes fabricated in the form of mesa structures grown on semiconductor substrates, a) p-i-n and b) UTC (simplified). There are two limiting cases for these structures, one where the n-layer becomes a dielectric ($\sigma = 0$) (c), and the other when it becomes a perfect conductor (d).

In the first analytical and simulated evaluations of TW photodiodes [27], the signal-collecting microwave waveguide was regarded as a vertical MSM microstrip waveguide, which is a vertical arrangement of metal stripline followed by a semiconductor layer and again a metal stripline ("a vertical sandwich MSM"). However, since semiconductor layers cannot be grown on a metal bottom layer, they can only be realized through a flip-chip process [88] which further complicates the already difficult fabrication process. Therefore, the bottom conductor stripline of the vertical (mesa) structure is normally realized by a highly doped semiconductor layer (*n*-layer in Figure 3.5), connecting the central mesa structure to the outer metal CPW-striplines. For either p-i-n or UTC lumped-element and TW photodiodes, this doping was usually taken in the range of 1×10^{19} cm^{-3} [39][50], roughly corresponding to a conductivity of 1.6×10^{5} S/m [50]. Figure 3.5 shows these two types of photodiodes. Therefore, this conductivity range was analyzed so as to find an absorption in the sub-mm and THz range as low as possible, i.e. for obtaining the highest possible THz output power. The *n*-layer in Figure 3.5 is the underlying doped layer for which the effect of changing the conductivity is investigated in this work.

The Drude model, $\sigma(n_e) = e \cdot \mu(n_e) \cdot n_e$, can be used to estimate the conductivity, assuming that the electron concentration equals the doping concentration. The decaying tendency of the mobility, $\mu(n_e)$, as a function of doping, can be estimated for example from Kopf et al. [89].

However, the full-wave simulations described in the present paper work with the conductivity σ. The correct conversion in doping levels is secondary and not analyzed further here. In the simulations presented, the conductivity range corresponds roughly to a carrier concentration range from 10^{12} cm^{-3} (intrinsic semiconductor) to 10^{22} cm^{-3} (value for gold). Such very high doping values cannot be reached in a practical semiconductor since structural problems will occur. Doping levels as high as 7×10^{19} cm^{-3} can be achieved in InP, and 5×10^{19} cm^{-3} in InGaAs, using metal organic chemical vapor phase deposition (MOCVD) [90].

By varying the conductivity of this *n*-layer from 0 to ∞, the effective waveguide structure changes from a quasi-planar co-planar waveguide (Figure 3.5c) to a vertical microstrip arrangement (Figure 3.5d). Since the *i*-layer is ideally an insulator, both limiting cases have low losses. However, the intermediate cases, the real cases of p-i-n or UTC-TW photodiodes with intermediate conductivity in the *n* layer, should have higher losses. This can be understood as follows. Generally, the ohmic losses per length unit result from the cross-sectional overlap of electric field and current density pattern $\vec{j}(\vec{r})$,

$$\begin{aligned} v_{ph} \cdot \frac{dW}{dz} = \frac{dW}{dt} &\approx -\int_V \vec{j} \cdot \vec{E}\, dV \approx -\int_V \sigma(\vec{r}) \cdot \left|\vec{E}\,(\vec{r})\right|^2 dV \\ &\approx -\bar{\sigma} \int_V \left|\vec{E}(\vec{r})\right|^2 dV \approx -\frac{2\bar{\sigma}}{\varepsilon_0 \bar{\varepsilon}} W, \end{aligned} \tag{3.1}$$

where $W = \epsilon_0/2 \cdot \int_V \varepsilon(\vec{r}) \left|\vec{E}(\vec{r})\right|^2 dV \approx \epsilon_0 \bar{\varepsilon}/2 \cdot \int_V \left|\vec{E}(\vec{r})\right|^2 dV$ is the energy stored in a volume V with a sufficiently large cross section, A, outside of which the field can be neglected. The length of the test volume may be chosen to be half of the wavelength to account for one whole current pattern, i.e. $V = A \cdot \lambda/2$. Then, we can write $dW/dz = -\alpha W$, where $\alpha = 2\bar{\sigma}/c\epsilon_0\sqrt{\bar{\varepsilon}}$ is the absorption constant. Note that $\bar{\sigma}$, the average conductivity, increases first with low values of σ. In contrast, $\bar{\sigma}$ does not necessarily increase when σ increases further in sub-volumes (high-doping areas and metal contacts), since the penetration depth of the electric field is increasingly reduced (skin depth effect), so that the overlap integral is dominated by the intermediate and low conductivity areas. This expression may also provide the possibility to determine the absorption constant directly from the numerical electric field and current density solution or the σ profile at a specific position on the transmission line. However, for

high conductivities, the spatial resolution required in the thin overlap regions between high E-field (and low current density) and low E-field (and high current density) must be appropriately high to obtain a sufficiently precise numerical solution in this way. This constitutes a difficulty in terms of computational time, so that in praxis we could not show that this method produces consistent results.

The way the waveguide losses develop when the underlying "sub-collector" n layer changes from an insulating layer to a perfectly conducting one, is therefore investigated in the present work by using full-wave simulations in two different simulation platforms via Ansoft's High Frequency Structural Simulator (HFSS™) and CST's Microwave Studio™.

These simulations were originally deemed worthwhile because a previous experiment, with travelling-wave photomixers based on planar electrodes on LT-GaAs, revealed increased sub-mm transmission-line losses when the free-electron density below the transmission line was increased by optical absorption [91].

We first develop an idealized analytical transmission line model and derive the model parameters from first principles. Then we describe the structural model used for the simulations and compare the absorption constant results obtained with two different methods.

3.3.2.1. Analytical Model

A simplified analytical model of the structures, presented in Figure 3.6 was set up to support the full-wave analysis described further below. Although the analytical model is not showing all the features of the full-wave analysis, it still justifies the overall behavior.

Note that in the following analysis no radiation losses (Poynting vector) are included. From the simulation results and from earlier work [6][92] it can be seen that they are small in comparison with the level of absorption losses discussed here. Nevertheless, they complicate the simulations and are discussed accordingly.

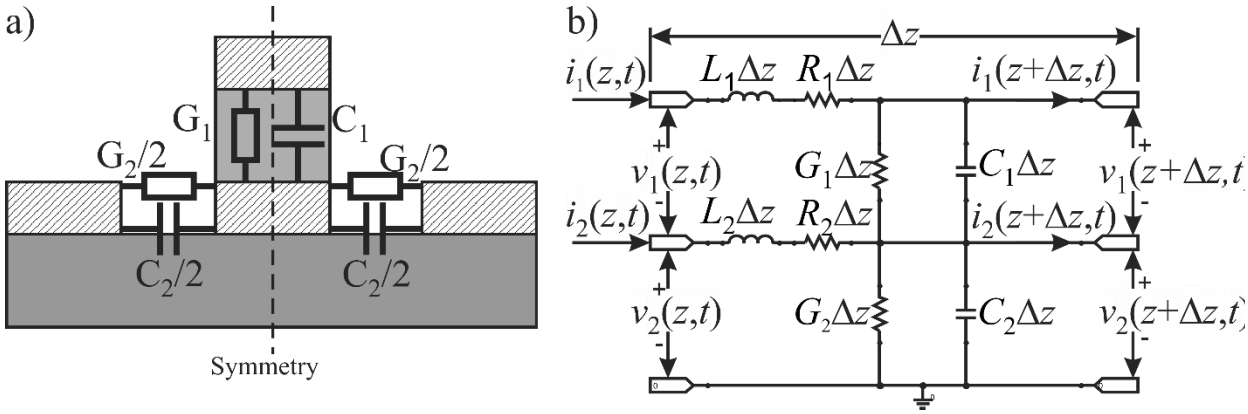

Figure 3.6. a) Conductances and capacitances represented on the waveguide. b) Voltage and current definitions and equivalent circuit for an incremental length Δz of transmission line. The reduced geometry is obtained from the symmetry in a).

Figure 3.6a shows the cross-section of a waveguide structure, which represents the intermediate cases between a coplanar waveguide and a microstrip line. In the cross-section, the equivalent conductances and capacitances, taken into account in the analytical model, are represented. A longitudinal representation of an infinitesimal Δz-length section of this waveguide is illustrated in Figure 3.6b. Its cross-sectional symmetry can be modeled as a lumped-element circuit for which the following quantities per unit of length are defined:

R_1 and R_2 = series resistances,
L_1 and L_2 = series inductances,
G_1 and G_2 = shunt conductances,
C_1 and C_2 = shunt capacitances.

The series inductances L_1 and L_2 represent mainly the mutual inductances between the two inner striplines and the ground line (outer CPW striplines), respectively. On the other hand, the mutual inductance between the two inner striplines is neglected due to a much lower separation. A finite length of the waveguide is viewed as a series of sections of the form shown in Figure 3.6b.

The replacement geometry in Figure 3.6b is now equivalent to an asymmetric CPW. Although the Eigen-modes of a symmetric CPW (as in Figure 3.6a) are the symmetric mode and the anti-symmetric mode, those of an asymmetric one (as in Figure 3.6b) should be hybrid combinations of both. The following linear differential equation system is established:

$$\begin{bmatrix} dV_1(z)/dz \\ dV_2(z)/dz \\ dI_1(z)/dz \\ dI_2(z)/dz \end{bmatrix} = \begin{bmatrix} 0 & 0 & A & B \\ 0 & 0 & 0 & -B \\ C & 0 & 0 & 0 \\ -C & D & 0 & 0 \end{bmatrix} \begin{bmatrix} V_1(z) \\ V_2(z) \\ I_1(z) \\ I_2(z) \end{bmatrix} \quad \text{with} \quad \begin{matrix} A = -(R_1 + j\omega L_1) \\ B = -(R_2 + j\omega L_2) \\ C = -(G_1 + j\omega C_1) \\ D = -(G_2 + j\omega C_2). \end{matrix} \tag{3.2}$$

The normalized general solution of this system for one propagation direction, determined in Matlab™ using symbolic evaluation, is given by:

$$\begin{bmatrix} V_1(z) \\ V_2(z) \\ I_1(z) \\ I_2(z) \end{bmatrix} = c_1 \begin{bmatrix} \gamma_1 \dfrac{\gamma_1^2 + BC + BD}{AC^2} \\ \gamma_1 \dfrac{\gamma_1^2 + BC - AC + BD}{ACD} \\ -\dfrac{\gamma_1^2 + BC + BD}{AC} \\ 1 \end{bmatrix} e^{-\gamma_1 z} + c_2 \begin{bmatrix} \gamma_2 \dfrac{\gamma_2^2 + BC + BD}{AC^2} \\ \gamma_2 \dfrac{\gamma_2^2 + BC - AC + BD}{ACD} \\ -\dfrac{\gamma_2^2 + BC + BD}{AC} \\ 1 \end{bmatrix} e^{-\gamma_2 z} \tag{3.3}$$

where the two complex propagation constant distinguish two wave modes and are given by:

$$\begin{aligned} \gamma_q(f,\sigma) &= \alpha_q(f,\sigma) + j\beta(f,\sigma) \\ &= \sqrt{\frac{AC}{2} \mp \frac{\sqrt{A^2C^2 - 2ABC^2 + 2ABCD + B^2C^2 + 2B^2CD + B^2D^2}}{2} - \frac{BC}{2} - \frac{BD}{2}} \end{aligned} \tag{3.4}$$

where the subscripts $q = 1{,}2$ refers to complex propagation constant 1 and 2. α_q is the absorption constant and it arises from Ohmic losses in the conductors and the dielectric materials. The dielectric losses dominate when the substrate is highly conductive due to, for example, free carriers coming from the doping of the semiconductor substrate. β_q is the phase constant, and it determines the degree of dispersion a signal experiences, and it is affected primarily by the geometry of the transmission line, its dimensions, and the substrate permittivity. The two solutions obtained for the two complex propagation constants, γ_1 and γ_2, correspond to two different propagation modes. This section will show that the second mode has a much higher absorption constant than the first mode which suggests that propagation will occur in the first mode.

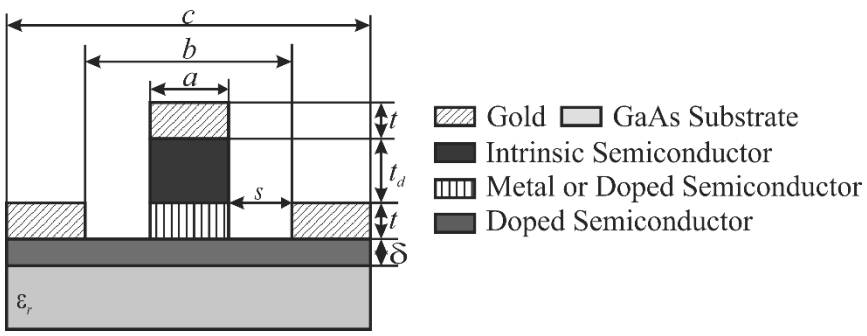

Figure 3.7. Cross-sectional view of the CPW structure with relevant parameters. Specific dimensions are given in Table 3.1.

The parameters G_1, G_2, R_1, R_2, L_1, L_2, C_1, and C_2 must be determined to find the coefficients A, B, C, and D. The resistances per length, R_1 and R_2, are found from the gold conductivity of $\sigma = 4.5 \times 10^7$ S/m, using the geometry of Figure 3.7 and $R = \rho/A = 1/(\sigma A)$, where A is the area of the transversal cross section of each conductor. The capacitance C_1 is found from $C_1 = \varepsilon_0 \varepsilon_r a/t_d$, where a and t_d are defined in Figure 3.7. The second capacitance per length is given by $C_2 \approx \pi \cdot (1+\varepsilon_r)\varepsilon_0 s/\left[2(d+s)\log[2\left(1+\sqrt{\kappa}\right)/\left(1-\sqrt{\kappa}\right)]\right]$, where ε_r is the relative permittivity of the substrate, $d = (c-b)/2 \approx a$ is the electrode width of both outer conductors, $s = (b-a)/2$ is the gap width between the electrodes, and $\kappa = \{1 - \tan^4[\pi d/4(d+s)]\}^{1/2}$ is a dimensionless quantity [3]. The inductance L_2 is calculated as $L_2 = \mu_0\{t_d^2 + ((b-a)/2\,)^2\}^{1/2}/a$ [93]. In the same manner, L_1 is calculated as $L_1 = \mu_0 t_d/t$ [93]. If we regard the layer corresponding to C_1 and G_1 as intrinsic, then we have $G_1 = 0$. If there is an average photo-illumination, the conductivity per length can be calculated from the photocurrent per length as $G_1 = \partial I_{ph}/\partial z/V_{bias}$ while it can also be expressed as $G_1(\omega) \approx \sigma_{illu}(\omega) \cdot a/t_d$. The conductance G_2 is estimated as $G_2(\omega) \approx \sigma(\omega) \cdot \delta/2s$, where $\delta \coloneqq \min(\delta(\omega), \delta_{DC})$ is the minimum function between the skin depth, $\delta^2(\omega) = 2\left(\sqrt{1+(\omega\varepsilon/\sigma)^2} + \omega\varepsilon/\sigma\right)/\sigma\omega\mu$ [94], and the DC E-field penetration depth, δ_{DC}, which depends only on the gap s and not on the frequency. The *ab-initio* values of these circuit parameters are given in Table 3.2, using the geometry of Figure 3.7 and the dimensions of Table 3.1, where typical dimensions of waveguides used for microwave, sub-mm, and THz generation are compared. The dimensions of our waveguide were considered the smallest possible to be reliably reached in micro-fabrication over larger areas, to access the highest possible frequencies. Later, the present model is fitted to the simulation results in order to determine a second set of constants.

Table 3.1: Overview of coplanar waveguide parameters used in literature ($b = a + 2s$).

Maximum intended frequency	a	s	c	Mesa thickness t_d	Metal thickness t	Substrate thickness t_s	Ref.
(GHz)	(μm)	(μm)	(μm)	(μm)	(μm)	(μm)	---
	16	12		-	0.1	200	[95]
300	10	10		-		500	[96]
500	36	3	342	-		500	[97]
2000	4	1 (3)*	10	1	0.1	500	our work

* The present study is made with $s = 1$ µm, but $s = 3$ µm is also discussed.

Figure 3.8 summarizes the main results of this model plotted over the conductivity range $1 \times 10^{-1} - 4.5 \times 10^{7}$ S/m. The absorption constant α_1 is found to be constant up to 10 S/m, and exhibits a peak beginning well before 1×10^{3} S/m which has an increasing maximum towards higher frequencies (Figure 3.8a). Up to the conductivity value of that maximum of α_1, α_2 is constant, but much larger than it, but then begins to increase without limit.

Table 3.2: Parameter values of the analytical model as determined from material constants and geometry.

Parameter	Unit	Calculated Value
R_1	Ω/m	1.2×10^{5}
R_2	Ω/m	6.1×10^{4}
L_1	$\mathrm{H/m}$	4.4×10^{-7}
L_2	$\mathrm{H/m}$	1.3×10^{-5}
C_1	$\mathrm{F/m}$	4.6×10^{-10}
C_2	$\mathrm{F/m}$	2.6×10^{-11}
G_1	$\mathrm{S/m}$	0 or $<10^{3}$
G_2	$\mathrm{S/m}$	$0.1 - 4.5 \times 10^{7}$

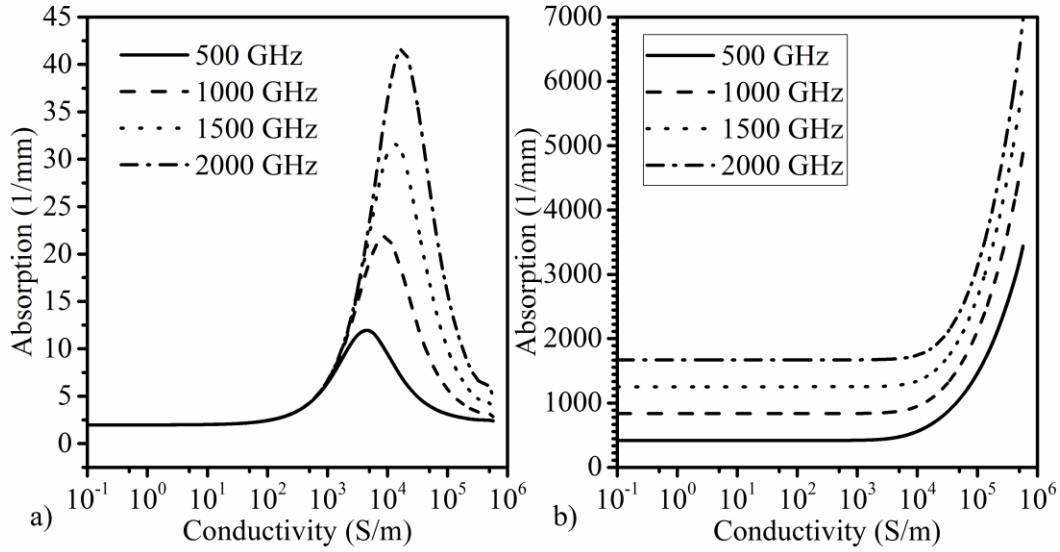

Figure 3.8. Analytical solutions for the absorption constants a) α_1 and b) α_2 (real parts of γ_1 and γ_2) plotted versus conductivity for 0.5, 1.0, 1.5, and 2.0 THz.

Figure 3.9 shows a spectral comparison between α_1 (Figure 3.9a) and α_2 (Figure 3.9b) for various conductivities. The absorption constant α_1 has a square-root dependence up to a frequency of 10 GHz as shown in Figure 3.9a, where it starts to saturate. For the conductivity values of 4.8×10^4 and 1.7×10^5 S/m, it starts to rise again at frequencies of 200 GHz and 300 GHz, respectively. From that standpoint, higher conductivities seem to be favorable. In Figure 3.9b it can be seen that α_2 increases linearly for frequencies up to 1 GHz and then with the square-root of the frequency, except for very low conductivities. α_2 is larger than α_1 starting from a given frequency in the sub-GHz range where they cross. This crossing frequency decreases as the *n*-layer conductivity increases (Figure 3.9c). These findings at low frequencies may be just of academic interest, as the present article is aimed at the sub-mm and THz range. Nevertheless, they were followed to find the parameters which could lead to the identification of the second mode in the simulations. However, interestingly this was not successful.

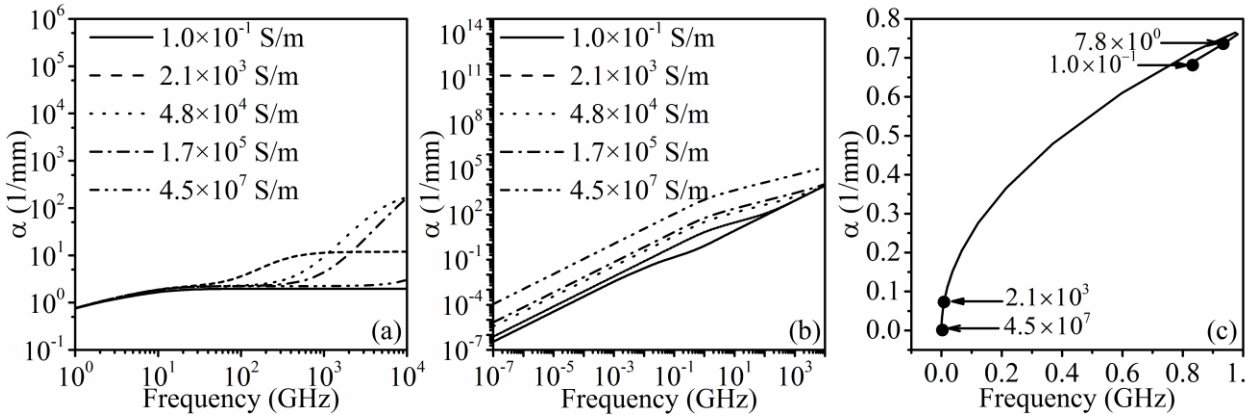

Figure 3.9. Absorption constant versus frequency for different conductivities for a) α_1 and b) α_2. c) Absorption and frequency of the interception points between the curves of $\alpha_1$and α_2, from the plot a) and b) within a conductivity range of $1 \times 10^{-1} - 4.5 \times 10^{7}$ S/m.

Initially simplifying the model to two coupled parallel transmission lines, the buried central stripline between the top central and outer ground striplines (see the layer labeled as metal or doped semiconductor in Figure 3.7) was assumed to have the conductivity of gold. The results have been described above. As a straightforward approach to making the model more realistic, the central buried stripline was also assumed to have the medium conductivity of the underlying highly doped semiconductor layer. In this case, this line would be unified with the *n*-layer and virtually insignificant. This is the case in the numerical simulations. Modeling in this manner, the graph of absorption vs. conductivity was surprisingly almost identical. This suggests that basically no longitudinal (i.e. in the z-direction) currents are flowing in this central buried conductor. Analysis of the current density animations of the doped semiconductor (see Appendix E) renders that assumption reasonable. We also varied G_1 instead of G_2, keeping the latter at a constant intermediate value. This gives, as expected from the symmetry of the solution in equations (3.2)-(3.4), a similar curve as in Figure 3.8a. This situation is important for considering the photonic excitation of sub-mm waves along the stripline, since a modulation of the conductivity G_1 in time and in the z-direction (phase-match [7]) of a TW-UTC or TW-p-i-n also implies an average stationary conductivity. Assuming that a photocurrent would not be larger than 100 mA per 100 µm stripline length, this would correspond to a conductivity G_1 of less than 1×10^3 S/m, and, therefore would, according to Figure 3.8a, give an absorption constant of less than 5 mm^{-1}. Additionally, according to the following simulation results, the absorption constant would give less than 15 mm^{-1}. Moreover, it should be possible to measure the illumination-induced absorption by a pump-probe experiment on vertically illuminated distributed photomixers [91].

3.3.2.2. Simulations in CST Microwave Studio™ and High-Frequency Structural Simulator (HFSS™)

Simulations performed in CST Microwave Studio™ and in HFSS™ are reported for the dimensions indicated in Table 3.1. Results as a function of frequency and n-layer conductivity are given here.

3.3.2.2.1. Structural Model

Figure 3.10a and Figure 3.10b show the model of a given CPW structure (cross-sectional and top view, respectively) used in HFSS™ and CST™. This is a mesa structure where losses are introduced by the medium conductivity ($0.1 - 4.5 \times 10^7$ S/m) of the underlying doped semiconductor. The mesa structure corresponds to a p-i-n or UTC photodiode as shown in Figure 3.5, in which the intrinsic semiconductor layer thickness is on the order of 1 µm. Since it is representative for those cases, the doped semiconductor layer, located below the intrinsic layer, is assumed to be 0.5 µm thick and 7 µm wide, with an unchanged dielectric permittivity of $\varepsilon = 12$. The central gold CPW line is 100 nm thick. The dimensions according to Figure 3.10a are: $s = 1$ µm, $a = 4$ µm and each of the outer striplines is about 2 µm wide. The length L is chosen appropriately for the range of absorption values (e.g. 300 µm). Figure 3.10b shows the ports used in CST™ and HFSS™. Figure 3.10d displays a typical scattering parameter S_{12} obtained in HFSS™.

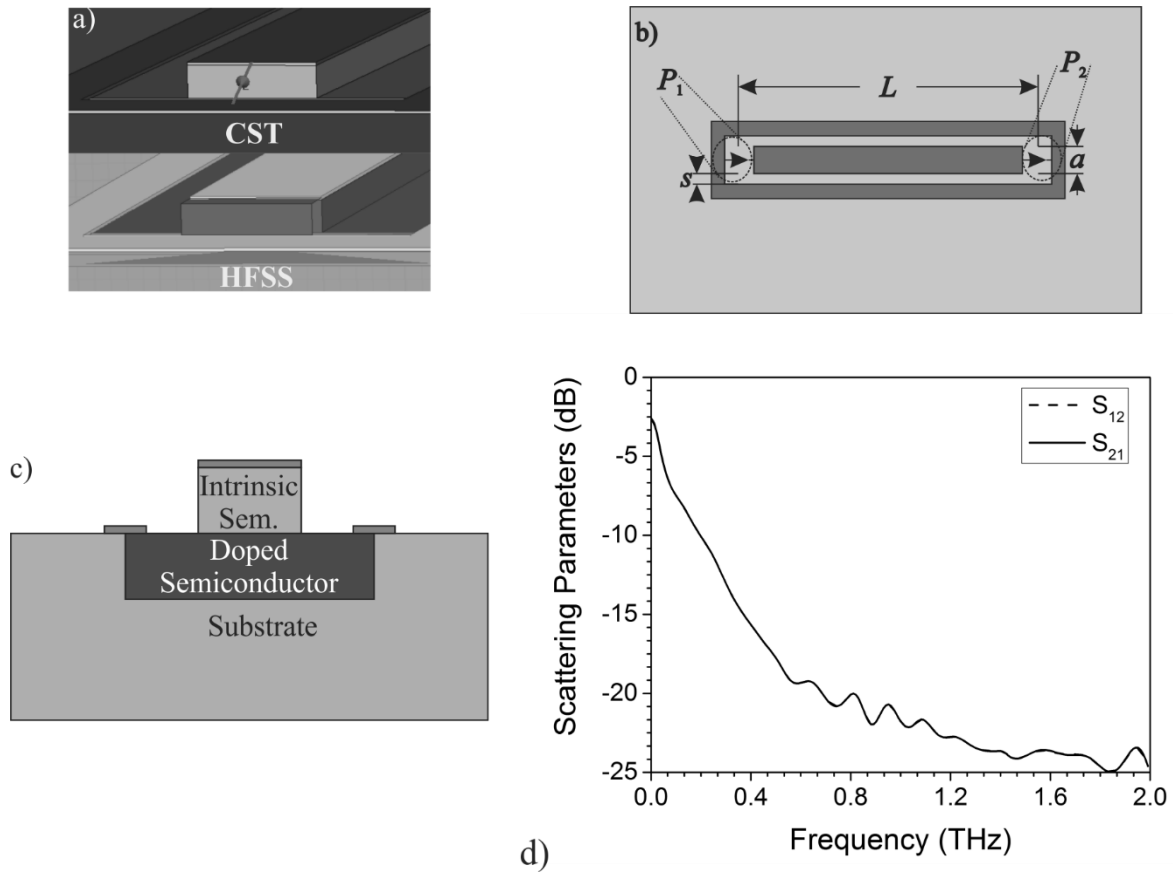

Figure 3.10. The geometry of the simulations. a) Port geometry used in CST™ (discrete port) and HFSS™ (distributed port). b) Top view of the quasi-CPW model to simulate characteristic impedance and absorption constant where P_1 and P_2 are the ports. c) A cross-sectional view of the quasi-CPW model. d) An example of a simulation result in HFSS™ for $\sigma = 5 \times 10^4\ S/m$ (the ripple is due to residual standing waves).

3.3.2.2.2. Extraction of the absorption constant from S-parameter simulations

Under the assumption that the port impedances are matched to the stripline, and defining L as the length of the CPW, the absorption coefficient α is determined in the first approach from S_{12} by equating $e^{-\alpha L} = I_2/I_1 = |S_{12}|^2$, or

$$\alpha(f) = -\frac{2}{L}\ln(|S_{12}(f)|) \tag{3.5}$$

To obtain the optimum value for the CPW characteristic impedance Z_0, at which the power from port 1 is transferred best to the waveguide (and extracted from it at port 2 of equal impedance), the Smith chart for S_{11} was inspected in CST Microwave Studio™, and centered on each conductivity value by adjusting the port impedance. For this, the simulation is stopped after the

seed pulse is coupled in completely, so that multiple reflections and thus resonances are ignored (see section 3.3.1).

Figure 3.11 shows the absorption coefficient as a function of conductivity and frequency. They were obtained by first computing the S_{12} parameters (through the simulations explained in section 3.3.2.2.1), then the absorption values are calculated using equation (3.5). Only the results from HFSS™ are displayed, as those from CST™ are strikingly similar. The most interesting feature of the result is the presence of a "central valley" of minimum losses appearing around a conductivity value of 5×10^4 S/m. The estimated doping value to obtain this conductivity is a doping level of approximately 2×10^{18} cm^{-3} [39][50]. From the absence of a second peak in the theoretical model, and from naïve thinking, one would expect the best conductivity to be the highest possible value achievable with heavy doping. In contrast, the result presented here shows that such doping values should be on top of the second peak, thus not giving the least possible absorption.

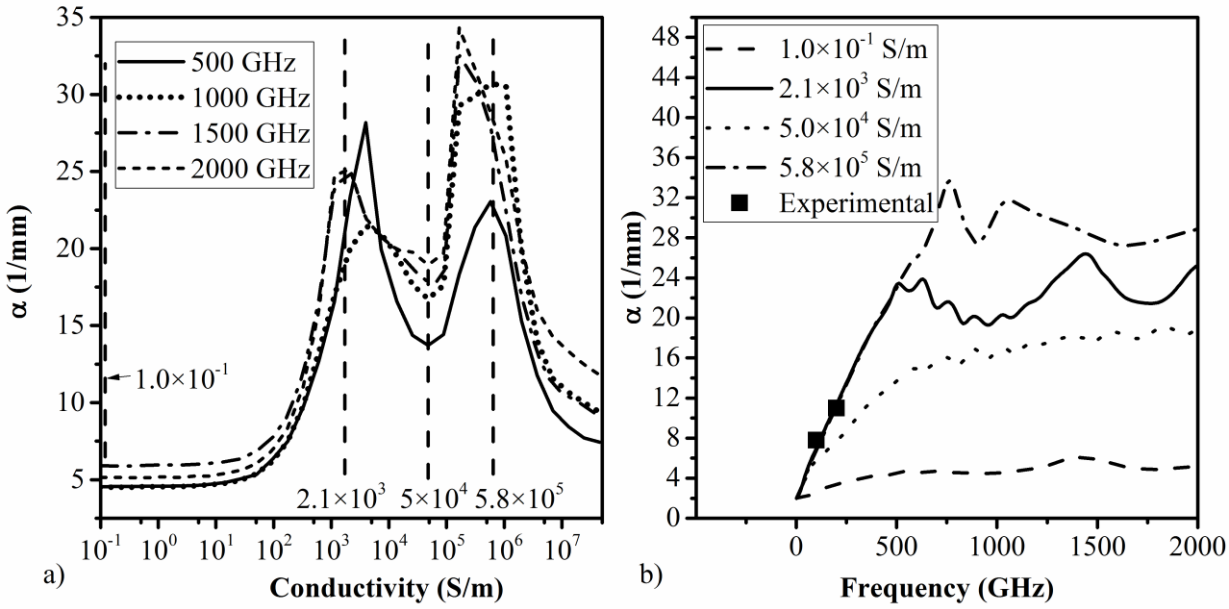

Figure 3.11. THz-absorption as a function of a) conductivity and b) frequency. The results shown are obtained using HFSS™. A couple of experimental values from own measurements on a distributed UTC-photodiode [30] are also inserted. The n-layer doping level of the measured devices is 1×10^{19}cm^{-3}, which corresponds to a conductivity of roughly 1.6×10^5 S/m.

As an explanation of the two peaks, Figure 3.11a can be subdivided in three regions. In the first region, 1×10^{-1}-2.1×10^3 S/m, the absorption is due to dielectric losses. In the second region, 2.1×10^3 - 5×10^4 S/m, the absorption starts to decrease due to that the THz wave travels in a slow-wave regime in

which the electric field does not pass through the doped layer but only the magnetic field [98]. Indeed, we observe in the simulations a drop in group-velocity over this region. This decreasing absorption reaches a minimum at a conductivity $\sigma_{min}=5\times10^4$ S/m. For larger conductivities, the doped layer acts as a poor conductor with associated skin-effect, and the absorption rises again. Finally, at metal-like conductivities for the doped semiconductor layer the absorption is that of a microstrip line without dielectric losses. Furthermore, it is clear that this two-fold behavior of the electric and magnetic field penetration cannot be reflected in the analytical model with one set of constants. Rather, two different sets of constants would be necessary for the two regimes.

3.3.2.2.3. Calculation of the absorption constant from the decay of the central stripline current

The results from Figure 3.11a were supported by plots of current density vs distance obtained as follow. First, the volume current density was calculated in HFSS™. Second, an imaginary line was placed parallel to the contact center stripline main axis, centered and located 0.1 um below its surface. Third, the current density was measured along this imaginary line and plotted as shown in Figure 3.12. Finally, the current density was fitted using the equation $y = a\exp(-bx) + c$ to obtain the current decay, where a represents the RMS current value at zero distance, b is the absorption constant, and c represents the background current. The power absorption constant $2b$, which is obtained in this way, is plotted against conductivity for 500 GHz and 2000 GHz, as shown in Figure 3.13a and Figure 3.13b. Again, two peaks of maximum absorption appear.

A background current is observed in Figure 3.12, whose values are in the range of a few percent. This remnant current could be explained by coupling from the CPW into the lossless substrate (radiation losses), formation of substrate modes in the lossless substrate, and re-coupling of those to the rear part of the CPW. The increasing value of the remnant current, i.e. radiation (output and input) coupling, with frequency, supports this view. To confirm this explanation, a waveguide port was inserted at the bottom of the substrate and indeed a transmission through this port was detected.

Due to this background current, the S_{12} parameter may be perturbed and so the determination of the absorption constant according to equation (3.5) may be not reliable in the case of high absorption values. In particular, the absorption peaks in Figure 3.11 are expected to be underestimated by the approach presented in this section.

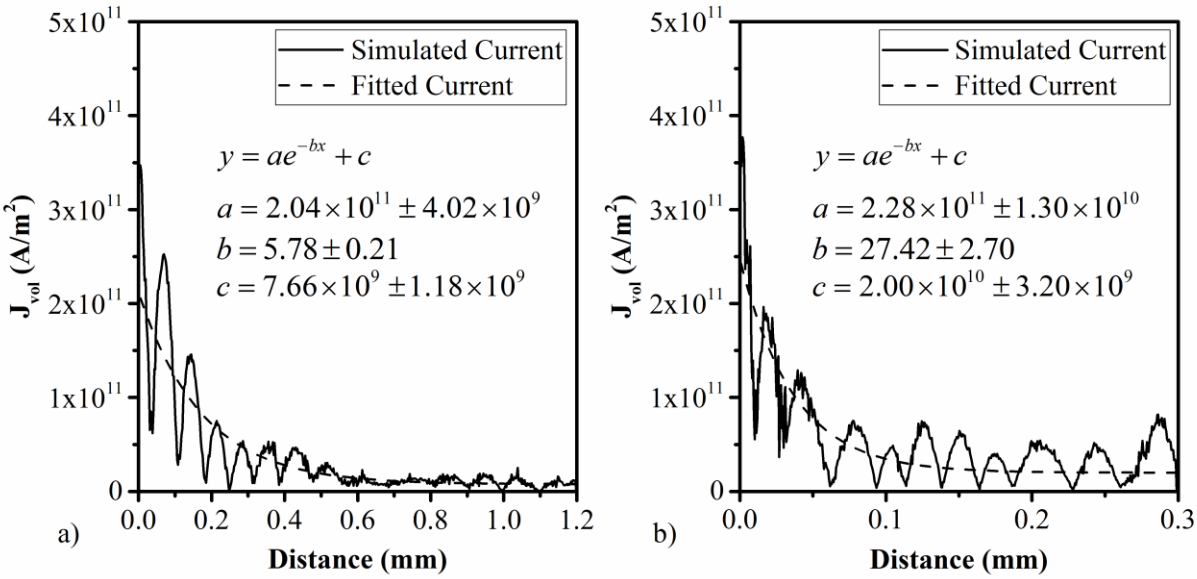

Figure 3.12. The instantaneous current density on the central stripline for a lossy layer with 5.0×10^4 S/m, as simulated in HFSS™ for the 1-μm gap device. The maxima move with time to the right (see movie in the supplemental material). An exponential function with offset is fitted to it. a) device simulated at 500 GHz and b) device simulated at 2000 GHz.

Superior values for the parameters R_1, R_2, L_1, L_2, C_1, and C_2 were obtained by fitting the analytical model for the absorption expressed by equations (3.4). To fit the analytical model, the plots shown in Figure 3.12 were used in such a way that the parameter values, which were used to calculate the absorption value in the analytical model, fit consistently for both frequencies 500 GHz and 2000 GHz, simultaneously. The results of the fit are shown in Figure 3.13 for 500 GHz and 2000 GHz, respectively. The fitted values for the parameters R_1, R_2, L_1, L_2, C_1, and C_2 are summarized Table 3.3.

Table 3.3. Parameter values as determined by fitting the analytical model to the simulation result.

Parameter	Unit	Calculated Value
R_1	Ω/m	5×10^{5}
R_2	Ω/m	6.1×10^{4}
L_1	H/m	5×10^{-6}
L_2	H/m	1.3×10^{-5}
C_1	F/m	4×10^{-10}
C_2	F/m	1×10^{-9}
G_1	S/m	0
G_2	S/m	$1.0\times10^{-1} - 4.5\times10^{7}$

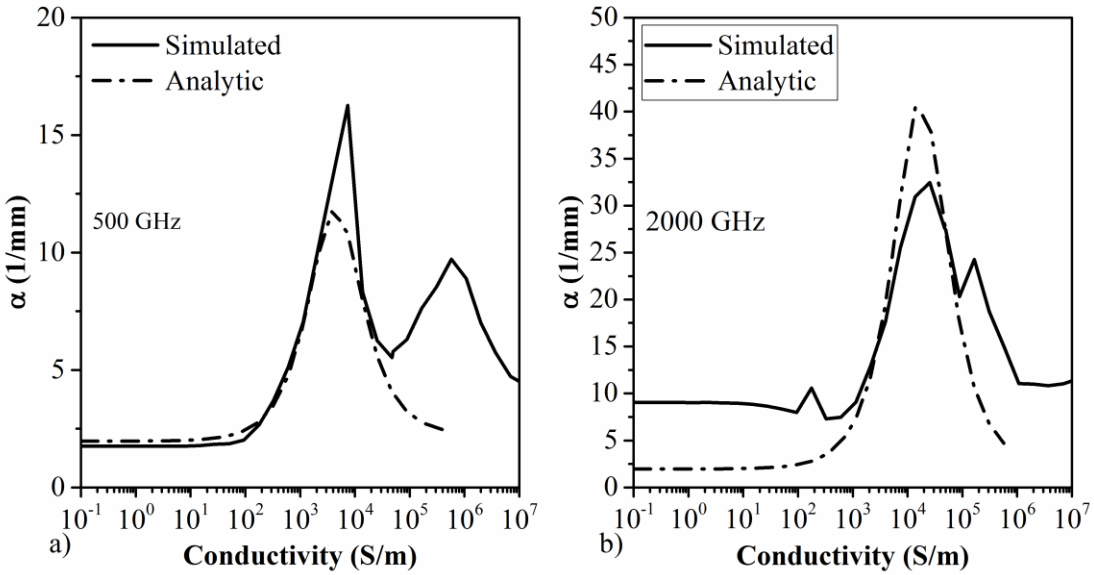

Figure 3.13. Line: Simulated absorption α_1 against conductivity σ is obtained as the fitting constant from current density vs. length plots as shown in Figure 3.12 for the 1-μm gap device. Dash-Dot: Fitting the analytical model to the simulation results for a) for 500 GHz b) for 2000 GHz.

The gap width of 1 μm for which we determined the full picture of the absorption may not be realistic to fabricate in many cases. Therefore, we made a spot check with a 3 μm gap which is compared in Figure 3.14 with the result for 1 μm. The important result is the position of the valley and, therefore, the optimum conductivity and the absorption value at that conductivity does not appear to change with the gap width. Only the strengths of the absorption peaks vary.

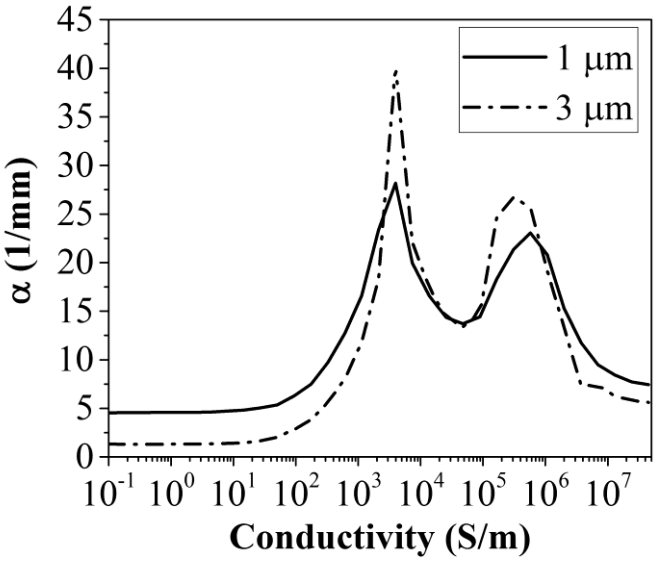

Figure 3.14. THz absorption as a function of conductivity for a 1-μm-gap and a 3-μm-gap between the center and lateral striplines at a frequency of 500 GHz indicating their differences in THz values. The results shown are obtained using HFSS™.

We did additional simulations varying parameters like a, s, c, t_d, and the permittivity ε of the substrate and doped layer, but the position of the valley at $\sigma = 5\times10^4$ S/m remains practically constant. This was verified for the four different frequencies used through this investigation.

3.3.2.3. Discussion

The numerical results were compared with those related to a distributed circuit model to calculate the propagation constant $\gamma(f,\sigma)$. The general current solution was obtained from the differential equations using *a-priori* parameter values for the equivalent circuit (Table 3.1) that represent the quasi-planar CPW transmission line. The dependence of the bottom layer conductivity was substituted into G_2. That way, the numerical results illustrated in Figure 3.14 were verified. Nevertheless, the analytical model gives just one peak, whereas the simulations show the same two peaks of the absorption constant as a function of conductivity in both platforms (HFSS™ and CST Microwave Studio™). The *a priori* values of the analytical model parameters were also used as initial values to fit the analytical model to the simulation results. The fitting results are summarized in Table 3.3 and are close to the *a priori* values except for the parameters L_1 and C_2 because they differ by two orders of magnitude from the a priori values. C_2 may be underestimated because in the original derivation of the cited expression for C_2 of an interdigitated structure [3] there probably have been used approximations. L_1 may have been

underestimated because we assumed that just the distance between the two conductors matters.

In the simulations, the absorption constant α was extracted from the S_{12} parameter (Figure 3.11, both simulation programs) and from the decay of the current-density traveling along the center stripline (Figure 3.12 and Figure 3.13, only HFSS™) and shows a significant "central valley" near 5×10^4 S/m. The results obtained by HFSS™ and CST™ were consistently similar, despite them employing two different numerical methods. Even the various side-peaks in the (α,f)–plane occur in both simulations, therefore it is unlikely that they are artifacts. The analytical model predicts two modes (see equation (3.4)). The first mode has a maximum of absorption whereas the absorption of the second mode is increasing with conductivity without limit according to Figure 3.8. These second-mode absorption values are constant and proportional to frequency for conductivity values lower than 1×10^4 S/m, because the transmission line acts as a low-pass filter. Beyond this conductivity value, the second-mode absorption value increases without limit. This could be understood by assuming that it is the CPW mode between the buried center conductor and the outer striplines which is increasingly shortened out towards larger values of G_2. In this picture, the first mode should then be more related to the pure microstrip mode between the two vertically separated center conductors. For the asymmetric CPW-substitution circuit of Figure 3.6b, both modes should then rather be linear combinations of the two Eigen-mode solutions, the symmetric and the anti-symmetric, of a planar symmetric CPW. However, the appearance of any second mode could not be identified from the simulations (see Appendix E). This is probably because its absorption constant is very high (see Figure 3.8b and Figure 3.9), so that even very close to the input port it is too weak to be noticed. The simulation of the case of 1.0×10^{-1} S/m at 1.0×10^{-2} GHz (see Figure 3.9a), where the absorption of the second mode should be less, did not reveal a different mode. The question then remains as to why it exhibits that much absorption. Therefore, the analytical model appears to be too simple to explain this unseen second mode and the second absorption peak appearing in the plots versus conductivity. Nevertheless, the described model fits fairly well with the first absorption peak. From the symmetry of the replacement circuit model of Figure 3.6b, it is not surprising that by varying G_1 in the range in which previously G_2 was varied, and keeping G_2 constant, produces a result similar to that of Figure 3.8. As G_1 can be steered by the optical illumination of the diode structures, this effect could be studied in the future in an optical experiment with vertically illuminated distributed photodiodes, similar to that demonstrated previously [91].

Full-wave numerical calculations of the sub-millimeter and THz losses of a quasi-planar, coplanar waveguide (CPW) of a distributed (travelling-wave) p-i-n-like photodiode were performed in CST™ and HFSS™ as a function of the ground layer conductivity and frequency. Additionally, an analytical model was implemented to validate the absorption values obtained by the simulations. Plots of absorption versus conductivity were made in three ways. The first method was by using equation (3.5). The second was by fitting plots of current density versus distance with the exponential function; the argument of the exponential function represents the absorption constant. The third approach was by obtaining a closed-form expression for the propagation constant from an equivalent-circuit model. The first two methods showed a local minimum in the absorption plot around a conductivity of 5×10^4 S/m. The third way, after obtaining *a priori* parameter values followed for a second iteration by fitting them with the absorption plot of the second method, showed a single peak instead of two peaks. Despite this, the absorption values are consistently similar to those from the first and second way, for frequencies of 500 and 2000 GHz. A possible physical reason for a second peak arising is the slow-wave transition, where the first peak corresponds to a transition to just the electric field being shield, while the second corresponds to a transition to the complete electromagnetic field being shielded by the semi-conducting layer. This shows that the equivalent-circuit model cannot be precise enough to describe the THz-absorption behavior of the quasi-planar, coplanar waveguide (CPW) of a distributed (travelling-wave) p-i-n-like photodiode.

According to this research the maximum possible doping value in InP of 5×10^{19} cm^{-3} should be on top of the second peak, thus not giving the least possible absorption value. Doping levels higher than 5×10^{20} cm^{-3}, equivalent to a conductivity value of 8.0×10^5 S/m and still on the second peak, are generally not physically possible in doped semiconductors. Therefore, the valley-value of 5×10^4 S/m, corresponding to a doping of $\approx 2 \times 10^{18}$ cm^{-3}, is the best practical conductivity value in distributed photodiode structures for THz-applications. However, to draw more precise conclusions as to which exact doping level to use in practice, the accurate dependence of the conductivity on the doping level must be known for the specific semiconductor used.

3.3.3. Achievable sub-millimeter THz-power

As a continuation of the previous section, where analytical models and simulations were performed to study the behavior of the conductivity change of the underlying doped layer on the THz absorption, here we develop a theoretical model describing the THz power generated from the devices depicted in Figure 3.15. Figure 3.15 also shows two new structures (Figure 3.15b and Figure 3.15c) additional to the structure depicted in Figure 3.10.

These structures were simulated in HFSS with the purpose of making a comparison in THz loss and THz power. Their dimensions are defined in Table 3.4. The analytical model for the THz power was developed taking into account the underlying-doped-layer conductivity, the THz absorption and impedance obtained by the RF simulations performed in Microwave CST Studio™ and HFSS™. This chapter will start with a description of the theoretical model employed to model the THz power originated from three different structures defined in Figure 3.15, followed from the results and explanation of the results obtained from this theoretical model.

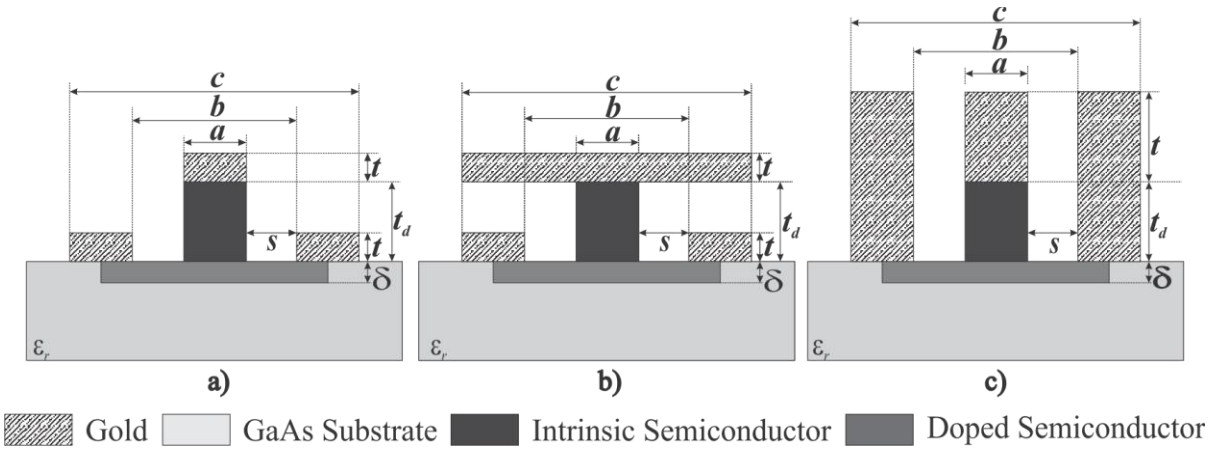

Figure 3.15. The geometry for the simulations performed in CST™ and HFSS™. a) Quasi-CPW structure[70]. b) Mushroom structure. c) Wall structure geometry.

Table 3.4: CPW parameters.

Structure	**a**	**s**	**c**	**Mesa thickness** t_d	**Metal thickness** t	**Substrate thickness** t_s
	(μm)	(μm)	(μm)	(μm)	(μm)	(μm)
Quasi CPW Structure	4	1	10	1	0.1	200
Mushroom-CPW Structure	4	1	10	1	0.1	500
Wall-CPW Structure [70]	4	1	10	1	6	500

Figure 3.16 shows a VI-TW-UTC photomixer, where the transmission line (CPW) and its antenna is clearly depicted. This picture shows the axis coordinates, where the z axis is parallel to the CPW, and the y axis is perpendicular to the photomixer surface. The origin of this system coordinates is located at the intersection between the backward wave attenuator and the

CPW. This transmission line has a length L. The antenna is located at position L. The antenna of this device is similar to a slot bow tie, but with transmission lines substituting all edges. The motivation to do this is to allow laser illumination (on the left side) to enter from above into the chip (with a reflection at a Bragg-reflector at the bottom of the chip, to be focused onto the waveguide from below). From symmetry reasons for the antenna the same is introduced also on the right side.

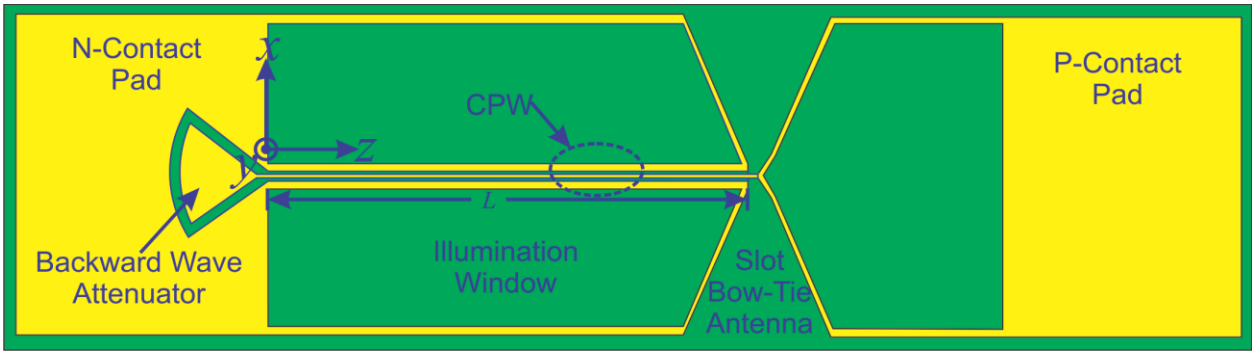

Figure 3.16. Transmission line geometry used in the computation of the achievable THz power. This is a micrograph of the fabricated mixers in the stage before the air-bridge is fabricated which connects the top of the mesa diode structure with the right side of the antenna.

The THz power generated at the position of the antenna of a vertically illuminated traveling-wave photomixer is given by:

$$P_{THz}(\omega) = \frac{1}{2} Z \cdot \left| I_{ph,ant}(\omega) \right|^2 \tag{3.6}$$

where

$$I_{ph,ant}(\omega) = \frac{I_{ph,ant}(0)}{1 + i\omega\tau_{tr}} \tag{3.7}$$

is the peak-value of the modulation part at angular frequency $\omega = \omega_2$-ω_1 of the photocurrent obtained by the beat of the two lasers (see section 1.2.1). Its theoretical maximum at $\omega \to 0$ is:

$$\begin{aligned} I_{ph,ant}(0) &= 2\Re(0)\sqrt{P_{NIR1} \cdot P_{NIR2}} = \Re(0) P_{NIR,tot} \\ &= \frac{\eta e}{h\nu}(1-R)(1-e^{-\alpha L}) P_{NIR,tot} \end{aligned} \tag{3.8}$$

as the maximum THz-power is obtained at $P_{NIR1} = P_{NIR2} = 0.5 P_{NIR,tot}$. η is the quantum-efficiency, which is given mainly by the photoconductive gain, $G \leq \tau_{rec}/\tau_{tr}$. The responsivity $\Re$ was simulated in Synopsis TCAD. Details about these simulations are explained in chapter 2. The total responsivity for a 3 µm diameter UTC-PD was found to be $\Re \approx 0.2$ A/W (see Figure 2.3), and

experimentally observed by us on a 5-μm-diameter UTC PD (focus from a with 4mm-diameter illumination of an aspheric lens with f=6.25mm) to be 0.05 A/W at $V_b = -1.6$ V, while the quantum limit is $\Re_{max}(1.5\mu m) \approx 1.25$ A/W.

τ_{tr} is the transit time between the doped absorption layer and the highly doped "sub-collector" bottom layer as shown in Figure 3.15 (a, b, or c), I_{ph} is the total photocurrent, Z is the characteristic transmission line impedance (ideally matched to the antenna impedance). τ_{tr} is calculated as $\tau_{tr} = t_d/v_e$, where t_d is the mesa thickness, as shown in Figure 3.15 and listed in Table 3.5, v_e is the electron velocity which can be as high as the overshoot velocity, which is v_e=4×10^7 cm/s in InGaAs. Therefore, τ = 2.5 ps, whose value corresponds to $f_m = 1/(2\pi\tau_{tr}) = 64$ GHz.

The total photocurrent superimposed at the antenna (at location $z = L$) from all contributions along the transmission line shown in Figure 3.16 is calculated as the convolution of the total photocurrent at:

$$I_{ph,ant}(\omega) = \int_0^L i(\omega, z) e^{-\gamma_{THz}(\omega)\cdot(L-z)}\, dz \qquad (3.9)$$

where $\gamma_{THz} \coloneqq \alpha_{THz} + j\beta_{THz}$ is the propagation constant defined in section 3.3.2.1, $i(\omega, z)$ is the incremental part of the photocurrent generated over an interval Δz at the position z. In equation (3.9) the propagation phase delay on the transmission line is modeled as $e^{-\gamma_{THz}(\omega)\cdot z}$.

To realize phase matching, i.e. the coincident arrival of all the partial current waves at the foot-point of the antenna, the additional phase shift to impose on the incremental photocurrents should be $i(\omega, z) = |i(\omega, z)| \cdot e^{-j\beta_{THz}\cdot z}$. This phase cancels the phase in eq. (3.9), so that one can leave out the imaginary part of the exponential term (the "phasor") and set γ_{THz} to be just α_{THz}. This phase-match ($\Delta k = 0$ between the optical fringes and the submm-signal propagation) is obtained from the angle tuning between the two laser beams as described in section 1.2.3.1.1 and is fulfilled if $v_{opt} = v_{THz}$, where v_{opt} is the velocity of the interference fringes along the surface, and v_{THz} is the group velocity of a THz wave generated in a dispersionless transmission line [7]. The attenuation α_{THz} is obtained from the simulations done in CST Microwave Studio™ y HFSS™ as explained in section 3.3.2.2.2.

Using with the conductivity, the total photocurrent over the stripline is

$$I(\omega) = V_b \cdot G_{TOTAL}(\omega) \qquad (3.10)$$

and the incremental part of it over an interval Δz, $i(z, \omega)$, is computed as:

$$i(\omega, z) = V_b \cdot g_{TOTAL}(\omega, z) \tag{3.11}$$

where $G_{TOTAL}(\omega)$ would be equal to $g_{TOTAL}(\omega, z) \cdot L$ in case of uniform illumination. But as there is an illumination profile, the following considerations should be taken into account. V_b is the applied voltage, $g_{TOTAL}(\omega, z)$ is the conductivity modulated by the illumination. The modulated conductivity due to the optical illumination results from two resistances in series. Written in conductances per length:

$$g_{TOTAL} = \frac{g_{ph} \cdot g_0}{g_{ph} + g_0} \tag{3.12}$$

where g_{ph} is the length-specific conductance due to the optical illumination in the absorption layer, and g_0 is the intrinsic conductance due to the doped bottom layer. The intrinsic conductivity due to the effective current cross section of the doped layer is approximately

$$g_0 = 2 \cdot \sigma \cdot \frac{A_{eff}}{s\, L} = 2\sigma \frac{\delta}{s} \tag{3.13}$$

where $s \approx (b + c)/2$ is the effective distance traveled by the electrons between the lateral two (therefore the factor of 2) striplines and the center stripline of the devices shown in Figure 3.15, and their values are listed in table Table 3.4. A_{eff} is approximated as $A_{eff} = \delta \cdot L$, where δ is the doped layer thickness. σ is the conductivity of the bottom layer.

The incremental THz photocurrent per length generated at the position z of a vertically illuminated traveling-wave photomixer is given by:

$$\left|i_{ph}(P, \omega, z)\right| \coloneqq \frac{dI_{ph}(P, \omega, z)}{dz} = \Re(\omega) \cdot p(P, z) \tag{3.14}$$

where

$$p(P, z) = \frac{P}{\sqrt{\pi} w_{NIR}} \cdot \exp\left(-\left(\frac{z - z_0}{w_{NIR}}\right)^2\right) \tag{3.15}$$

is the astigmatic Gaussian beam illumination one-dimensional intensity distribution along the transmission line whose maximum is located at z_0, expressed in [W/m], the other direction is integrated over the lateral dimension of the central stripline mesa structure. $\Re$ is the responsivity related to the vertical mesa-structure explained and simulated in section 1.2, which is now here in series with the doped bottom layer. P is the total optical power. The (two-dimensional) photocurrent density is obtained from equation (3.14), by dividing it through the central stripline width, a,

$$\left|J_{ph}(z)\right| = \frac{\left|i_{ph}(z)\right|}{a} \coloneqq \frac{1}{a}\frac{dI_{ph}}{dz} = \Re \cdot \frac{p(z)}{a} = \Re \cdot \frac{dP}{dA} \tag{3.16}$$

The total photocurrent of a LE-device would be

$$I_{ph} = J_{ph} \cdot \frac{\pi}{4} D^2 = \Re_{LE} \cdot P \tag{3.17}$$

From the TCAD simulations of a cylindrical device of diameter $D = 3$ μm (without a bottom layer which connects to a sideward metal electrode!) the lumped-element responsivity $\Re_{LE}$ was obtained to be 0.2 A/W under 2V of reverse bias and an optical input power of 1.8×10^{-4} W. We assume here that a TW-device of 4 μm central stripline (mesa) width would have a similar responsivity per area. However, note that simulations for a $D = 10$ μm device gave a slightly higher responsivity, see Figure 2.2, although the optical power was confined to the devices (no radiation spill-over in the simulation).

Therefore, we estimate that the TW responsivity $\Re$ would be similar, though somewhat higher. Under the simplifying assumption that $\widetilde{\Re} \coloneqq \Re/V_b$ is a constant, which would be 0.025 A/WV at -2V, we obtain

$$G_{ph}(P, \omega) = \widetilde{\Re}(\omega) \cdot P \tag{3.18}$$

$$g_{ph}(P, \omega, z) = \widetilde{\Re}(\omega) \cdot p(P, z) \tag{3.19}$$

using eq. (3.12),

$$g_{total}(P, \omega, z) = \frac{\widetilde{\Re}(\omega) \cdot p(P, z)}{1 + \frac{\widetilde{\Re}(\omega)}{g_0} \cdot p(P, z)} \tag{3.20}$$

This represents also the modulation amplitude, since the dark conductivity is zero. In case of $P \to \infty$ we have $g_{total}(P, \omega, z) \to g_0$, so that a saturated output power limit is given. The NIR input saturation power is then $P_{sat}(P, \omega) = g_0/\widetilde{\Re}(\omega)$. Note that this infrared power level might be beyond the thermal damage threshold we observe (13mA/250mW for a 5-μm diameter LE device).

The THz-power is now given from eq. (3.6), using eq. (3.20) and (3.15),

$$P_{THz} = \frac{Z}{2}\left[\Delta I_{ph,ant}(P, \omega)\right]^2 = \frac{Z}{2}\left[\int_0^L g_{total}(P, \omega, z)dz \cdot V_b\right]^2 \tag{3.21}$$

The values used in this research are described in Table 3.5.

Table 3.5. Parameter values used (D is the cylindrical diameter used in TCAD simulations).

	Symbol	Value	Units
Lumped element device in the TCAD simulations			
Applied voltage	V_b	2	V
Responsivity	$\Re$	2.9×10^{-2}	A/W
Optical Power	P	2.5×10^{-1}	W
Device area ($D = 3\ \mu m$)	$A = 4\pi(D/2)^2$	1.8×10^{-12}	m^2
Device area ($D = 10\ \mu m$)	$A = 4\pi(D/2)^2$	2.0×10^{-11}	m^2
TW device			
Length	L	3×10^{-4}	m
illumination waist	w_{NIR}	1×10^{-4}	m

The steps used to obtain the THz power are as follows. First, the impedance Z is obtained through the procedure used in section 3.3.1 for the structures depicted in Figure 3.15. A responsivity value $\Re \approx 0.2$ A/W and optical power of 2.1×10^{-2} W were used. This value was chosen because this is the optical input power before the responsivity falls abruptly for the 3-μm diameter device (see Figure 2.3). The next step is to plot $P_{THz}(z, \omega)$ vs z_0 through equation (3.9) to obtain the value of z_0 where $I_{ph,ant}(z, \omega)$ is maximum. This z_0 value is used to compute $P_{THz}(z, \omega)$ again, which will be used to obtain the THz power from equation (3.21).

Figure 3.17a shows the Gaussian beam pattern $p(P, z)$ used to excite the devices of Figure 3.15. The Gaussian beam has a maximum of 120 W/m, computed with a power of 2.1×10^{-2} W, which corresponds to a responsivity of 0.2 A/W, according to the results for the 3-μm diameter device shown in Figure 2.3. Before showing the results, an optimization should be carried, and this is the position z_0 where the terahertz power is maximum. Figure 3.17b shows the photocurrent as a function of the position z_0. The maximum terahertz power occurs at $z_0 = 3 \times 10^{-4}$ m. The underlying-doped layer conductivity was also varied. For all the conductivities, the position z_0 where the terahertz power is maximum were the same. Therefore, the value $z_0 = 3 \times 10^{-4}$ m will be used for all the computation. Figure 3.17c and Figure 3.17d show the terahertz power $P_{THz}(\sigma, f)$ as a function of the underlying-doped layer conductivity and frequency, respectively.

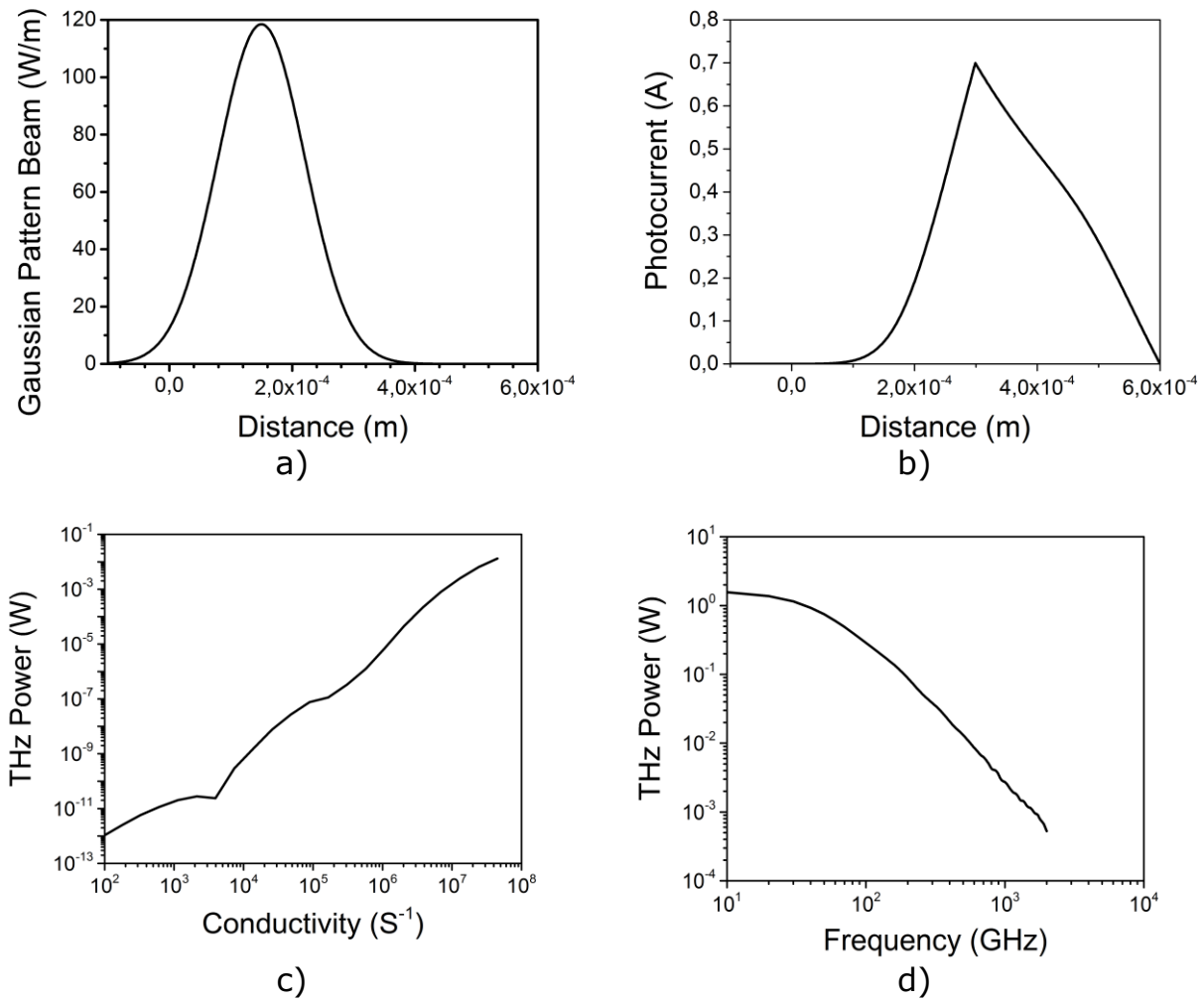

Figure 3.17. a) Gaussian Beam pattern $p(z)$ from equation (3.15). b) Photocurrent $I_{ph,ant}$ obtained from equation (3.9) as a function of the Gaussian beam maximum position z_0. c) Plot of terahertz power versus the underlying-doped layer conductivity at 500 GHz. d) Plot of terahertz power vs frequency with the doped layer at a conductivity of 4.5×10^7 S/m.

Figure 3.11a shows the absorption versus conductivity for the Quasi-CPW structure. As was stated earlier, there is a valley where a minimum of absorption exist. Figure 3.18 shows the plots of THz absorption vs doped layer conductivity for the Wall-CPW and Mushroom-CPW structures (see Figure 3.15) at frequencies of 500, 1000, 1500, and 2000 GHz. These plots were obtained using the procedure described in section 3.3.2.2 with the HFSS™ software. Different from the THz absorption in the Quasi-CPW structure, the minimum of the absorption valley is not clearly defined.

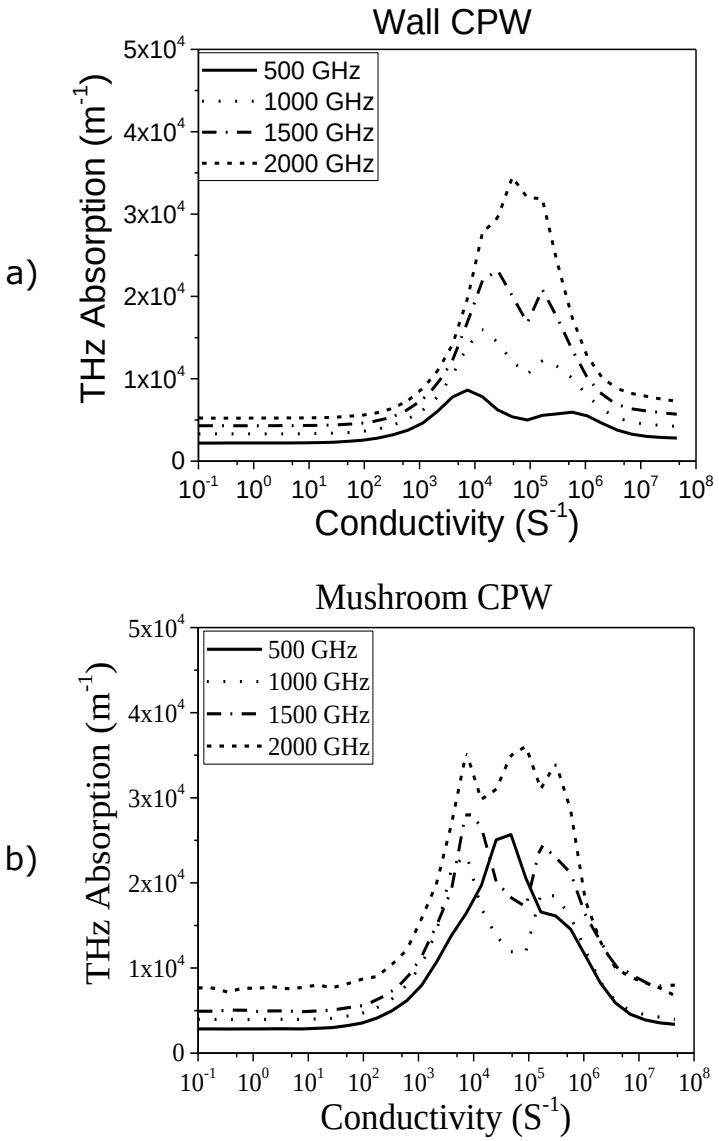

Figure 3.18. THz absorption as a function conductivity for the Wall-CPW (left), and Mushroom-CPW (right) structures.

Figure 3.19 shows the THz power vs the doped-layer conductivity with both axes in logarithmic scale, values for 500, 1000, 1500, and 2000 GHz and for all the three devices specified in Figure 3.15. The THz power increases as the *n*-layer conductivity increases for all the three devices. This figure also shows an approximately linear log-log plot with small deviations from this behavior. These deviations suggest the influence of the THz absorption in the THz power by the three devices. Figure 3.20 shows double-axis plots, in which the left axis is the THz absorption and the right axis is the THz absorption. The maximum deviations from the approximately linear log-log behavior appears to happen when the THz absorption is maximum in both peaks as shown in Figure 3.20, for the QCPW device. These deviations are also shown in Figure 3.20b y Figure 3.20c, which instead of two deviations as the case of the QCPW

device, appears to be one clearly defined on a small n-layer conductivity interval. Figure 3.19 also shows the decreasing nature of the THz power as the frequency increases from 500 to 2000 GHz. This decreasing nature of the THz Power with the frequency is observed also in Figure 3.21. Figure 3.21 shows the behavior of the THz power vs the frequency for conductivities of 1.0×10^{-1}, 2.1×10^{3}, 5.0×10^{4}, 5.8×10^{5}, and 4.5×10^{7} S/m.

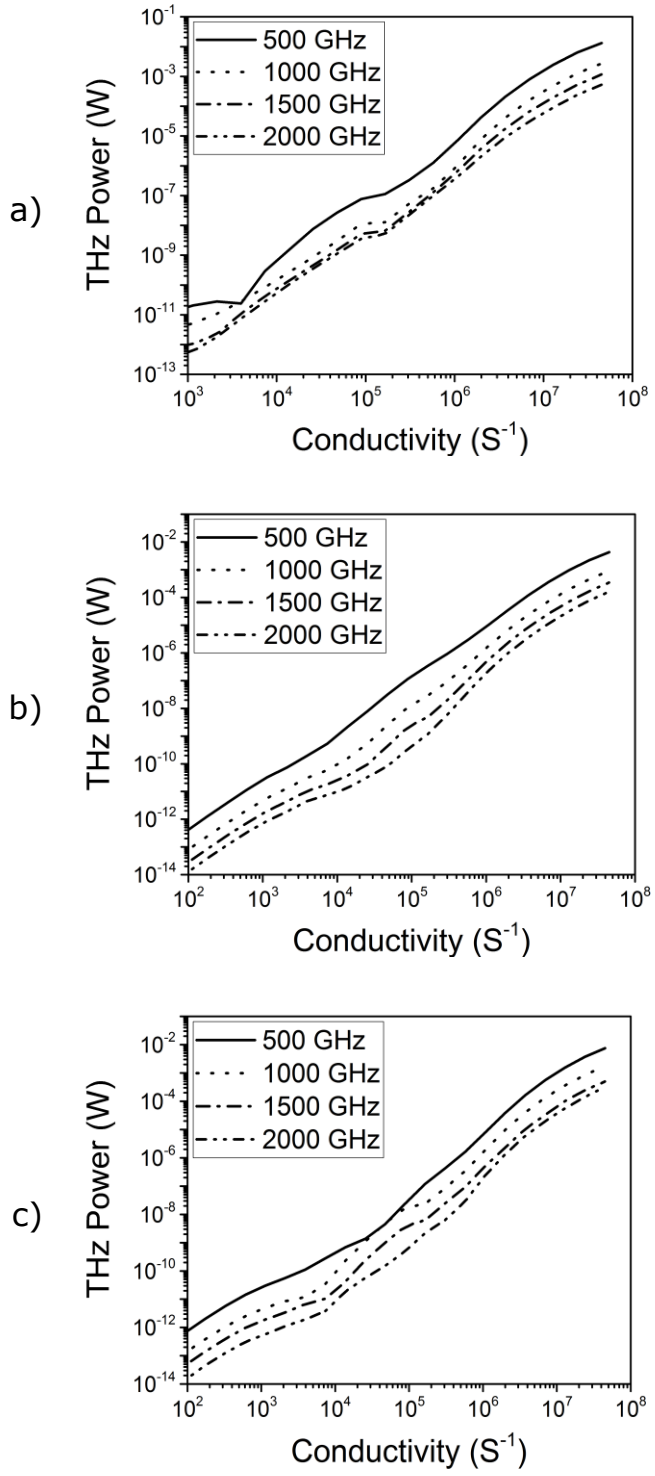

Figure 3.19. Curves of THz Vs doped-layer conductivity for 500, 1000, 1500 and 2000 GHz for a) Quasi-CPW structure, b) Wall-CPW structure, and c) Mushroom-CPW structure.

a)

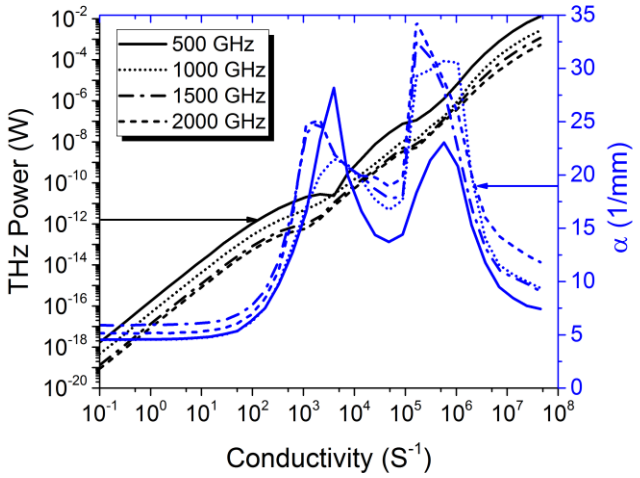

b)

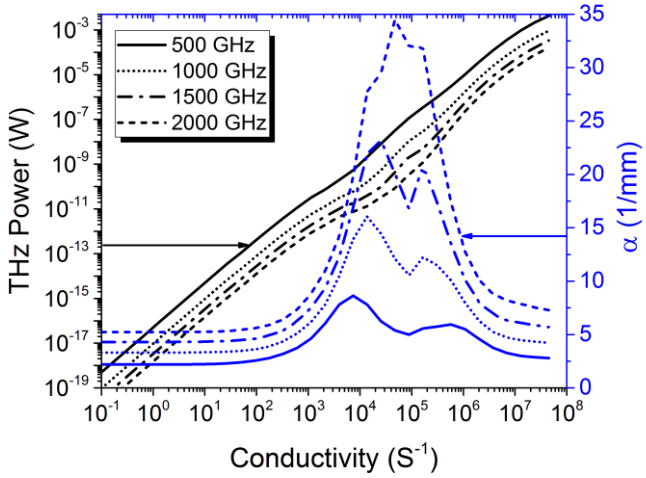

c)

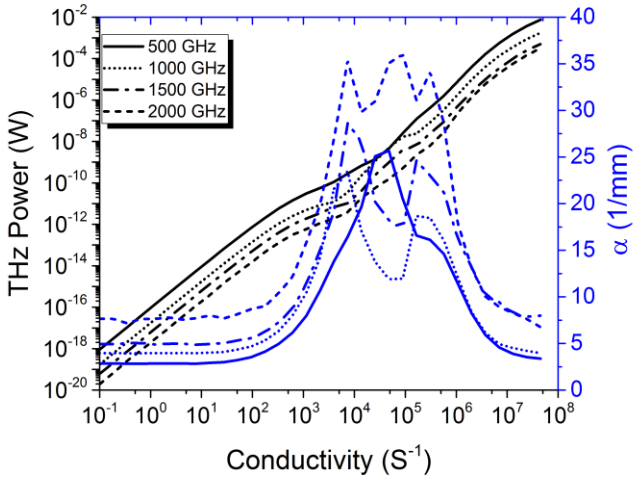

Figure 3.20. Curves of double axis showing the THz absorption (left axis) and THz absorption (right axis) Vs doped-layer conductivity for 500, 1000, 1500 and 2000 GHz for a) Quasi-CPW structure, b) Wall-CPW structure, and c) Mushroom-CPW structure.

a)

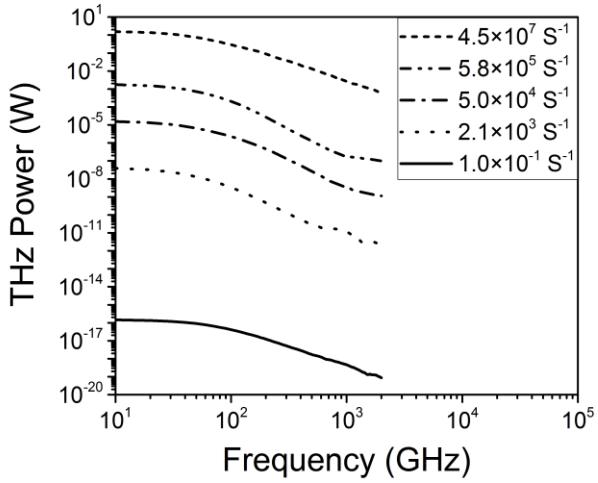

b)

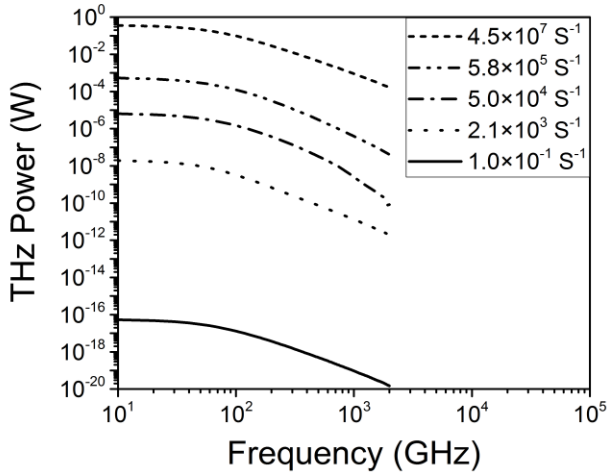

c)

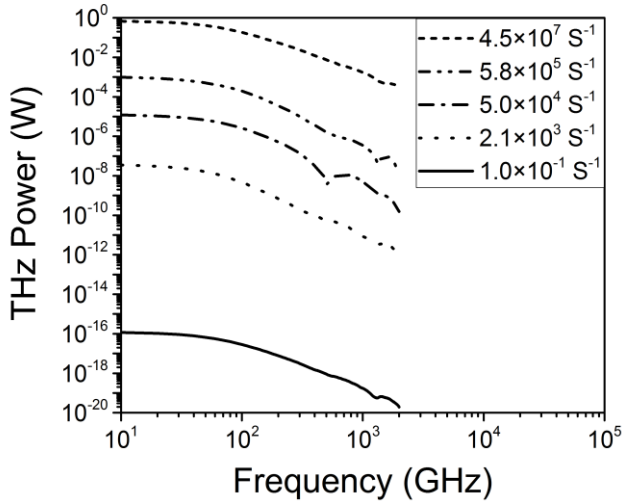

Figure 3.21. Curves of THz Power vs frequency for five doped-layer conductivities for a) Quasi-CPW structure, b) Wall-CPW structure, and c) Mushroom-CPW structure.

Figure 3.22 shows the behavior of the THz power vs the frequency for conductivities of 1.0×10^{-1}, 2.1×10^{3}, 5.0×10^{4}, 5.8×10^{5}, and 4.5×10^{7} S/m by making a comparison between the three devices defined in Figure 3.15. The comparison between the three devices with the *n*-layer conductivity of 1.0×10^{-1} and 4.5×10^{7} S/m, which correspond with the ideal cases of microstrip line and CPW (see Figure 3.5), shows that the Quasi CPW device have a higher output THz power than the Wall- and Mushroom-CPW devices. The Mushroom-CPW device also has a higher output power than the Wall-CPW device. This is explained using Figure 3.23. This picture shows that for all the *n*-conductivities, the Quasi-CPW characteristic impedance is always higher than the Mushroom-CPW and Wall-CPW characteristic impedance; the Mushroom-CPW characteristic impedance is also higher than the Wall-CPW characteristic impedance. The advantages of higher THz output power for any of the three devices is not clear with the *n*-layer conductivities of 2.1×10^{3}, 5.0×10^{4} and, 5.8×10^{5}.

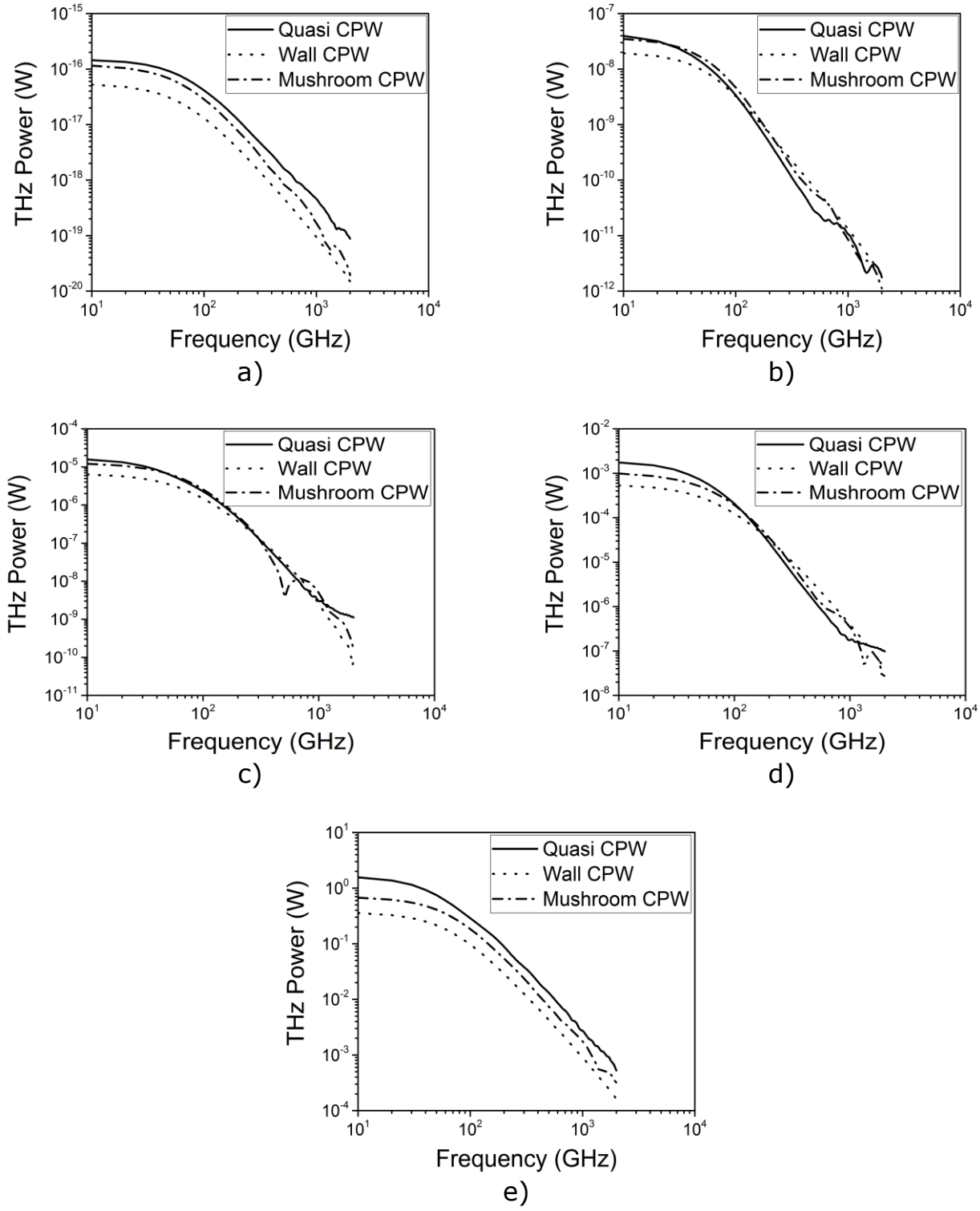

Figure 3.22. Curves of photocurrent vs frequency for Quasi-CPW, Wall-CPW, and Mushroom-CPW devices for the following *n*-layer conductivities a) 1.0×10^{-1}, b) 2.1×10^{3}, c) 5.0×10^{4}, d) 5.8×10^{5} and, e) 4.5×10^{7} S/m.

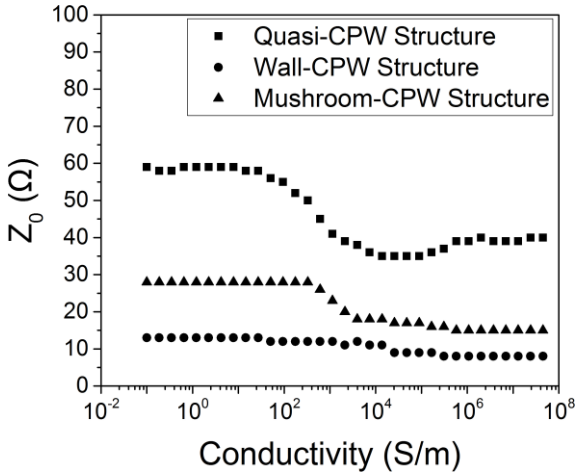

Figure 3.23. Plot of impedance vs the underlying layer conductivity

Therefore, the main way to reach reasonable THz power at the antenna position according to the above described model is by increasing the *n*-layer conductivity. Note that other than suspected from the beginning, the effect of the THz absorption shown in Figure 3.18 is not appreciable.

Geometries in which a metal layer replaces the semiconductor layer should lead, according to Figure 3.21, to a significant increase in output power. Unfortunately, conventional microfabrication architectures exclude this. Flip-chip techniques should be the way to introduce a metal bottom layer, but those techniques are extremely complicated and unreliable. Though, a metal-semiconductor-metal sandwich structure is not to be illuminated anymore vertically, so that then only edge-illuminated designs would make sense.

Note that the finding that the influence of the conductivity on the output power is stronger through the responsivity than through the waveguide absorption, is also very relevant for the discussion of the output power of lumped-element devices. Similarly, here designs with a bottom electrode from metals instead from highly-doped semiconductors should also then bring a breakthrough in output power.

The structures depicted in Figure 3.13b and Figure 3.13c, which are the Mushroom-CPW and Wall-CPW structure respectively, are characterized by a lower characteristic impedance, as showed in Figure 3.19. Therefore, despite they modify the distributed parameters, they do not contribute significantly in THz output power. Additionally, equation (3.22) marks the way to improve the THz output power: The research of high-impedance characteristic transmission lines.

4. Conclusions

4.1. Discussion

To reach our goal of performing simulations to analyze and design of VI TW UTC photomixers the following simulations areas were done: Semiconductor Carrier Transport and High-Frequency and Electromagnetic simulations.

DC carrier transport were done using the Hydrodynamic Carrier Transport Model with the aid of the numerical simulator Sentaurus TCAD. For this study, a cylindrical UTC photodiode of 3-μm diameter LE UTC device was studied. The physical behavior of the LE-UTC device was investigated at both low and high light levels. Under high light levels, the electrons start to accumulate at the cliff layers due to the discontinuities present at the cliff layers in the energy bandgap structure. Under this situation, the space charge effect become strong reducing the linearity of the LE-UTC devices and maximum output power. This suggest also the way in which the LE-UTC devices can be improved by the change of the material of the absorption layer from InGaAs to GaAsSb. This makes the junction between the absorption and collection layer a heterojunction type 2, by which the conduction and valence band energies from the absorption layer are higher than the energies from the collection layer. This allows a smooth transition for the carrier transport between these layers. The 3-μm diameter LE UTC device showed a maximum responsivity of 0.2 A/W. A velocity overshoot of 4×10^7 cm/s was obtained at the absorption layer. A maximum electron temperature of 7000 K was obtained at the collection layer. Despite the electron velocity is maximum at the absorption layer, the highest electron temperature is due to the intervalley scattering present at the collection layer and strong electric field. Finally, due to the complex carrier transport, several planned simulations were not successful carried out.

Full-wave numerical calculations of the sub-millimeter and THz losses of a quasi-planar, coplanar waveguide (CPW) of a distributed (travelling-wave) p-i-n-like photodiode were performed in CST™ and HFSS™ as a function of the ground layer conductivity and frequency. Additionally, an analytical model was implemented to validate the absorption values obtained by the simulations. Plots of absorption versus conductivity were made in three ways. The first method was by using equation (3.5). The second was by fitting plots of current density versus distance with the exponential function; the argument of the exponential function represents the absorption constant. The third approach was by obtaining a closed-form expression for the propagation constant from

an equivalent-circuit model. The first two methods showed a local minimum in the absorption plot around a conductivity of 5×10^4 S/m. The third way, after obtaining *a priori* parameter values followed for a second iteration by fitting them with the absorption plot of the second method, showed a single peak instead of two peaks. Despite this, the absorption values are consistently similar to those from the first and second way, for frequencies of 500 and 2000 GHz. A possible physical reason for a second peak arising is the slow-wave transition, where the first peak corresponds to a transition to just the electric field being shield, while the second corresponds to a transition to the complete electromagnetic field being shielded by the semi-conducting layer. This shows that the equivalent-circuit model cannot be precise enough to describe the THz-absorption behavior of the quasi-planar, coplanar waveguide (CPW) of a distributed (travelling-wave) p-i-n-like photodiode.

According to this research the maximum possible doping value in InP of 5×10^{19} cm^{-3} should be on top of the second peak, thus not giving the least possible absorption value. Doping levels higher than 5×10^{20} cm^{-3}, equivalent to a conductivity value of 8.0×10^5 S/m and still on the second peak, are generally not physically possible in doped semiconductors. Therefore, the valley-value of 5×10^4 S/m, corresponding to a doping of $\approx 2 \times 10^{18}$ cm^{-3}, is the best practical conductivity value in distributed photodiode structures for THz-applications. However, to draw more precise conclusions as to which exact doping level to use in practice, the accurate dependence of the conductivity on the doping level must be known for the specific semiconductor used.

An analytical model to account the THz output generated by three type of devices, Quasi-CPW, Wall-CPW, and Mushroom-CPW devices was developed at the input of the photomixer antenna. This analytical model takes into account the optical responsivity measured through the photocurrent delivered by the hydrodynamic carrier transport simulation, the characteristic impedance, the optical input power, the operating frequency, the *n*-layer doping (measured indirectly through the conductivity). This analytical model showed an increasing terahertz output power as the *n*-layer conductivity increases. The maximum THz output power is reached when the *n*-layer is replaced by a metal, but at the current state of the art, the conventional microfabrication excludes this possibility.

4.2. Future Work

The simulations based in carrier transport modeling and high-frequency RF simulations have proved to be of great help in the understanding of the physical functioning of VI-TW-UTC-PD devices. As a continuation of this project, several further steps can be taken.

One step is the simulation of UTC-PD devices in which the transition between the collection and absorption layer uses a junction of the type homojunction to study the performance in which the cliff layers are suppressed and, consequently, the transition between the collection and absorption layer is smooth.

A second step, simulations using the Silvaco TCAD tools are proposed to understand the differences with Synopsys Sentaurus TCAD.

The third step was a consequence that more different semiconductor analysis was needed and were not possible to develop in this thesis. These are mixed simulations like AC analysis, small-signal analysis and, transient response analysis.

The fourth step comes from the fact that the VI-TW-UTC-PD device is a transmission line based in UTC-PD device, it is known that both kind of simulations are needed to develop knowledge of performance. This doctoral thesis developed both simulations separately. The next step will be the integration between the semiconductor modeling and high-frequency RF simulations by use of the tools like Comsol Multiphysics. The software not only allows to simulate both types of physical phenomena, but also other phenomena such as optical and thermal simulations. Therefore, a future work will include the simulations of the vertical illumination by the two lasers and the simulation of the optical lenses needed to elaborate the photomixer experiment. The last version of Comsol (5.2a, year 2016) only supports the Drift-Diffusion Carrier Transport Model. Therefore, the integration with carrier transport modeling will be limited to the Drift-Diffusion Model. Other ways to integrate the different physical phenomena will be the use of programming tools like Visual Studio (C++, C#, Visual Basic, Java), Matlab, and Python.

The fifth step comes from analyzing equation (1.9), which shows that one way to improve the THz-power output is by increasing the antenna resistance. But, to increase the antenna resistance it is needed to develop new high-frequency structures for the transmission line that have a high characteristic impedance value assuming that this is perfectly coupled to the VI-TW-UTC-PD device. As they are developed, the behavior of the absorption versus the n-layer conductivity is proposed as part of the study to understand the performance of these new structures.

5. Bibliography

[1] E. R. Brown, K. A. McIntosh, F. W. Smith, M. J. Manfra, and C. L. Dennis, "Measurements of optical-heterodyne conversion in low-temperature-grown GaAs," *Appl. Phys. Lett.*, vol. 62, no. 11, pp. 1206–1208, Mar. 1993.

[2] E. R. Brown, K. a. McIntosh, F. W. Smith, K. B. Nichols, M. J. Manfra, C. L. Dennis, and J. P. Mattia, "Milliwatt output levels and superquadratic bias dependence in a low-temperature-grown GaAs photomixer," *Appl. Phys. Lett.*, vol. 64, no. 24, p. 3311, 1994.

[3] E. Brown, K. McIntosh, K. Nichols, and C. L. Dennis, "Photomixing up to 3.8 THz in low-temperature-grown GaAs," *Appl. Phys. Lett.*, vol. 66, no. 3, pp. 285–287, 1995.

[4] K. a. McIntosh, E. R. Brown, K. B. Nichols, O. B. McMahon, W. F. DiNatale, and T. M. Lyszczarz, "Terahertz photomixing with diode lasers in low-temperature-grown GaAs," *Appl. Phys. Lett.*, vol. 67, no. 26, p. 3844, 1995.

[5] S. Verghese, K. a. K. A. McIntosh, and E. R. Brown, "Optical and terahertz power limits in the low-temperature-grown GaAs photomixers," *Appl. Phys. Lett.*, vol. 71, no. 19, pp. 2743–2745, 1997.

[6] S. Verghese, E. Duerr, K. McIntosh, and SM, "A photomixer local oscillator for a 630-GHz heterodyne receiver," *IEEE Microw. Guid. Wave Lett.*, vol. 9, no. 6, pp. 245–247, 1999.

[7] S. Matsuura, G. a. Blake, R. A. Wyss, J. c. C. Pearson, C. Kadow, A. W. Jackson, and A. C. Gossard, "A traveling-wave THz photomixer based on angle-tuned phase matching," *Appl. Phys. Lett.*, vol. 74, no. 19, p. 2872, 1999.

[8] S. Duffy, S. Verghese, A. McIntosh, and A, "Accurate modeling of dual dipole and slot elements used with photomixers for coherent terahertz output power," *IEEE Trans. Microw. Theory Tech.*, vol. 49, no. 6, pp. 1032–1038, 2001.

[9] K. Giboney, J. Rodwell, and JE, "Traveling-wave photodetector theory," *IEEE Trans. Microw. Theory Tech.*, vol. 45, no. 8, pp. 1310–1319, 1997.

[10] K. S. K. Giboney, M. J. W. M. Rodwell, and J. J. E. Bowers, "Traveling-wave photodetector design and measurements," *IEEE J. Sel. Top. Quantum Electron.*, vol. 2, no. 3, pp. 622–629, 1996.

[11] D. Saeedkia, "Modeling and design of photoconductive and

superconductive terahertz photomixer sources," University of Waterloo, 2005.

[12] A. W. M. Lee, Q. Qin, S. Kumar, B. S. Williams, Q. Hu, and J. L. Reno, "Real-time terahertz imaging over a standoff distance (>25 meters)," *Appl. Phys. Lett.*, vol. 89, no. 14, p. 141125, 2006.

[13] J. Danielson, Y.-S. Lee, J. Prineas, J. Steiner, M. Kira, and S. Koch, "Interaction of Strong Single-Cycle Terahertz Pulses with Semiconductor Quantum Wells," *Phys. Rev. Lett.*, vol. 99, no. 23, Dec. 2007.

[14] N. Shimizu, N. Watanabe, T. Furuta, and T. Ishibashi, "Improved Response of Uni-Traveling-Carrier Photodiodes by Carrier Injection," *Jpn. J. Appl. Phys.*, vol. 37, pp. 1424–1426, 1998.

[15] H. Ito, T. Furuta, F. Nakajima, K. Yoshino, and T. Ishibashi, "Photonic generation of continuous THz wave using uni-traveling-carrier photodiode," *J. Light. Technol.*, vol. 23, no. 12, pp. 4016–4021, Dec. 2005.

[16] G. Torrese, I. Huynen, J. Raskin, and A. Vander Vorst, "Analysis and Design of pin Traveling-Wave Photodetectors for High Power and Wide-Bandwidth Applications," *IEEE Trans. Microw. Theory Tech.*, vol. 29, no. 11, pp. 1174–1182, 1981.

[17] S. Kodama and H. Ito, "UTC-PD-Based Optoelectronic Components for High-Frequency and High-Speed Applications," *IEICE Trans. Electron.*, vol. E90–C, no. 2, pp. 429–435, Feb. 2007.

[18] K. Sakai, *Terahertz optoelectronics*. Heidelberg: Springer, 2005.

[19] T. G. Phillips, "Submillimeter astronomy (heterodyne spectroscopy)," *Proc. IEEE*, vol. 80, no. 11, pp. 1662–1678, 1992.

[20] P. H. Siegel, "Terahertz Technology in Biology and Medicine," *IEEE Trans. Microw. Theory Tech.*, vol. 29, no. 6, pp. 575–2447, Oct. 2004.

[21] A. Fitzgerald, E. Pickwell, V. Wallace, A. Purushotham, S. Pinder, M. Linan, R. Pye, and T. Ha, "Medical Applications of Broadband Terahertz Pulsed Radiation," in *Lasers and Electro-Optics Society, 2005. LEOS 2005. The 18th Annual Meeting of the IEEE*, 2005, vol. 3, pp. 103–104.

[22] E. Peytavit, S. Arscott, D. Lippens, G. Mouret, S. Matton, P. Masselin, R. Bocquet, J. F. Lampin, L. Desplanque, and F. Mollot, "Terahertz frequency difference from vertically integrated low-temperature-grown GaAs photodetector," *Appl. Phys. Lett.*, vol. 81, no. 7, p. 1174, 2002.

[23] T. Ishibashi, S. Kodama, N. Shimizu, and T. Furuta, "High-speed

response of uni-traveling-carrier photodiodes," *Jpn. J. Appl. Phys.*, vol. 36, no. 10, pp. 6263–6268, 1997.

[24] N. Shimizu, Y. Muramoto, Y. Miyamoto, and T. Ishibashi, "High speed InP/InGaAs uni-traveling-carrier photodiodes," *Conf. Proceedings. 2000 Int. Conf. Indium Phosphide Relat. Mater. (Cat. No.00CH37107)*, pp. 313–316, 2000.

[25] T. Noguchi, A. Ueda, H. Iwashita, S. Takano, Y. Sekimoto, M. Ishiguro, T. Ishibashi, H. Ito, and T. Nagatsuma, "Millimeter wave generation using a uni-traveling-carrier photodiode," in *12th Int. Space Terahertz. Technol. Symp., San Diego, CA*, 2001.

[26] J. Liu, *Photonic devices*, First. New York: Cambridge University Press, 2005.

[27] K. S. Giboney, M. J. W. Rodwell, and J. E. Bowers, "Traveling-wave photodetectors," *IEEE Photonics Technol. Lett.*, vol. 4, no. 12, pp. 1363–1365, 1992.

[28] V. M. Hietala, G. a. Vawter, T. M. Brennan, and B. E. Hammons, "Traveling-wave photodetectors for high-power, large-bandwidth applications," *IEEE Trans. Microw. Theory Tech.*, vol. 43, no. 9, pp. 2291–2298, 1995.

[29] D. Lasaosa, J. Shi, D. Pasquariello, K.-G. Gan, M.-C. Tien, H.-H. Chang, S.-W. Chu, C.-K. Sun, Y.-J. Chiu, and J. E. Bowers, "Traveling-wave photodetectors with high power-bandwidth and gain-bandwidth product performance," *IEEE J. Sel. Top. Quantum Electron.*, vol. 10, no. 4, pp. 728–741, 2004.

[30] C. Barrientos Z, V. Calle, M. Diaz, F. P. Mena, J. Vukusic, J. Stake, and E. a Michael, "Vertically illuminated TW-UTC photodiodes for terahertz generation," in *Proceedings of SPIE*, 2012, vol. 8452, no. 1, p. 84522I–84522I–11.

[31] J. E. Giboney, K.S.; Rodwell, Mark J W; Bowers, "Traveling-wave photodetector," *IEEE Photonics Technol. Lett.*, vol. 4, no. 12, pp. 1363–1365, Jul. 1992.

[32] J. E. Bowers and C. A. Burrus, "High-speed zero-bias waveguide photodetectors," *Electronics Letters*, vol. 22, no. 17. p. 905, 1986.

[33] K. S. K. Giboney, R. L. Nagarajan, T. T. E. Reynolds, S. T. S. Allen, R. R. P. Mirin, M. J. W. M. Rodwell, J. E. J. Bowers, and R. Ngarajan, "Travelling-wave photodetectors with 172-GHz bandwidth and 76-GHz bandwidth-efficiency product," *IEEE Photonics Technol. Lett.*, vol. 7, no.

4, pp. 412–414, Apr. 1995.

[34] E. A. Michael, "Travelling-wave photonic mixers for increased continuous-wave power beyond 1 THz," *Semicond. Sci. Technol.*, vol. 20, no. 7, pp. S164–S177, Jul. 2005.

[35] H. R. Khazaei, O. Berolo, R. James, W. J. Wang, P. Maigné, M. Young, K. Ozard, M. Reeves, and F. M. Ghannouchi, "Charge carrier effect on the microwave losses observed on traveling-wave electrodes used in electro-optic modulators," *Microw. Opt. Technol. Lett.*, vol. 17, no. 4, pp. 236–241, 1998.

[36] T. Ishibashi, N. Shimizu, S. Kodama, H. Ito, T. Nagatsuma, and T. Furuta, "Uni-Traveling-Carrier Photodiodes - OSA Trends in Optics and Photonics Series," in *Ultrafast Electronics and Optoelectronics*, 1997, vol. 13, pp. 83–87.

[37] D. Pasalic and R. Vahldieck, "A hybrid drift-diffusion-TLM analysis of traveling-wave photodetectors," *IEEE Trans. Microw. Theory Tech.*, vol. 53, no. 9, pp. 2700–2706, Sep. 2005.

[38] Y. Hirota, T. Hirono, T. Ishibashi, and H. Ito, "Traveling-wave photodetector for 1.55 um wavelength fabricated with unitraveling-carrier photodiodes," *Appl. Phys. Lett.*, vol. 78, no. 24, pp. 3767–3769, 2001.

[39] E. Rouvalis, C. C. Renaud, D. G. Moodie, M. J. Robertson, and A. J. Seeds, "Continuous wave terahertz generation from ultra-fast InP-based photodiodes," *IEEE Trans. Microw. Theory Tech.*, vol. 60, no. 3, pp. 509–517, 2012.

[40] E. A. Michael, B. Vowinkel, R. Schieder, M. Mikulics, M. Marso, and P. Kordoš, "Large-area traveling-wave photonic mixers for increased continuous terahertz power," *Appl. Phys. Lett.*, vol. 86, no. 11, p. 111120, 2005.

[41] J. DiDomenico M., R. H. Pantell, O. Svelto, and J. N. Weaver, "Optical Frequency Mixing in Bulk Semiconductors," *Appl. Phys. Lett.*, vol. 1, no. 4, pp. 77–79, Dec. 1962.

[42] I. C. Mayorga, "Photomixers as tunable terahertz local oscillators," Rheinischen Friedrich-Wilhelms-Universität Bonn, 2008.

[43] S. Y. Chou, Y. Liu, W. Khalil, T. Y. Hsiang, and S. Alexandrou, "Ultrafast nanoscale metal-semiconductor-metal photodetectors on bulk and low-temperature grown GaAs," *Appl. Phys. Lett.*, vol. 61, no. 7, pp. 819–821, 1992.

[44] B. E. A. Saleh and M. C. Teich, *Fundamentals of photonics*, Second., vol. 13. Hoboken, New Jersey.: WILEY SERIES IN PURE AND APPLIED OPTICS, 2007.

[45] M. C. Beard, G. M. Turner, and C. A. Schmuttenmaer, "Subpicosecond carrier dynamics in low-temperature grown GaAs as measured by time-resolved terahertz spectroscopy," *J. Appl. Phys.*, vol. 90, no. 12, 2001.

[46] E. a. Michael, I. Cámara Mayorga, R. Gu¨sten, a. Dewald, and R. Schieder, "Terahertz continuous-wave large-area traveling-wave photomixers on high-energy low-dose ion-implanted GaAs," *Appl. Phys. Lett.*, vol. 90, no. 17, p. 171109, 2007.

[47] N. Vieweg, M. Mikulics, M. Scheller, K. Ezdi, R. Wilk, H. W. Hübers, and M. Koch, "Impact of the contact metallization on the performance of photoconductive THz antennas.," *Opt. Express*, vol. 16, no. 24, pp. 19695–19705, 2008.

[48] Sheila Prasad, H. Schumacher, and A. Gopinath, *High-Speed Electronics and Optoelectroncs*. New York, 2009.

[49] T. Ishibashi, S. Kodama, N. Shimizu, and T. Furuta, "High-speed response of uni-traveling-carrier photodiodes," *Jpn. J. Appl. Phys.*, vol. 36, pp. 6263–6268, 1997.

[50] T. Ishibashi, T. Furuta, H. Fushimi, S. Kodama, H. Ito, T. Nagatsuma, N. Shimizu, and Y. Miyamoto, "InP/InGaAs uni-traveling-carrier photodiodes," *IEICE Trans. Electron. E Ser. C*, vol. 83, no. 6, pp. 938–949, 2000.

[51] M. Shur, *Physics of semiconductor devices*. New Jersey: Prentice Hall, 1990.

[52] M. N. Feiginov, "Analysis of limitations of tetrahertz pin uni-traveling-carrier photodiodes," *J. Appl. Phys.*, vol. 102, no. 8, pp. 84510-1-12, 2007.

[53] B. Van Zeghbroeck, "Thermionic emission current," 1997. [Online]. Available: http://ecee.colorado.edu/~bart/book/msthermi.htm. [Accessed: 19-Jan-2016].

[54] B. Banik, J. Vukusic, H. Hjelmgren, and J. Stake, "Optimization of the UTC-PD Epitaxy for Photomixing at 340 GHz," *Int. J. Infrared Millimeter Waves*, vol. 29, no. 10, pp. 914–923, 2008.

[55] H. Ito, S. Kodama, Y. Muramoto, T. Furuta, T. Nagatsuma, and T. Ishibashi, "High-Speed and High-Output InP–InGaAs Unitraveling-Carrier

Photodiodes," *IEEE J. Sel. Top. Quantum Electron.*, vol. 10, no. 4, pp. 709–727, Jul. 2004.

[56] J. E. Bjarnason, T. L. J. Chan, A. W. M. Lee, E. R. Brown, D. C. Driscoll, M. Hanson, A. C. Gossard, and R. E. Muller, "ErAs:GaAs photomixer with two-decade tunability and 12 μW peak output power," *Appl. Phys. Lett.*, vol. 85, no. 18, p. 3983, 2004.

[57] D. Pasalic and R. Vahldieck, "A hybrid drift-diffusion-TLM analysis of traveling-wave photodetectors," Swiss Federal Institute of Technology Zurich, 2005.

[58] K. S. Giboney, "Travelling-wave photodetectors," University of California, 1995.

[59] L. Y. Lin, M. C. Wu, T. Itoh, T. a. Vang, R. E. Muller, D. L. Sivco, and A. Y. Cho, "High-power high-speed photodetectors-design, analysis, and experimental demonstration," *IEEE Trans. Microw. Theory Tech.*, vol. 45, no. 8, pp. 1320–1331, 1997.

[60] T. Chau, N. Kaneda, T. Jung, A. Rollinger, S. Mathai, Y. Qian, T. Itoh, M. C. Wu, W. P. Shillue, and J. M. Payne, "Generation of Millimeter Waves by Photomixing at 1.55 um Using InGaAs-InAlAS-InP Velocity-Matched Distributed Photodetectors," *IEEE Photonics Technol. Lett.*, vol. 12, no. 8, pp. 1055–1057, 2000.

[61] S. Iezekiel, *Microwave photonics*, First. Chichester: John Wiley & Sons, 2009.

[62] S. Matsuura, G. A. Blake, R. A. Wyss, J. c. Pearson, C. Kadow, A. W. Jackson, and A. C. Gossard, "Free-space traveling-wave thz photomixers," in *IEEE 7th Int. Conference on Terahertz Electronics*, 1999, pp. 24–27.

[63] S. Preu, S. Malzer, G. H. Do¨hler, Q. Z. Zhao, M. Hanson, J. D. Zimmerman, A. C. Gossard, L. J. Wang, and G. H. Döhler, "Interference between two coherently driven monochromatic terahertz sources," *Appl. Phys. Lett.*, vol. 92, no. 22, p. 221107, 2008.

[64] S. Verghese, "Highly tunable fiber-coupled photomixers with coherent terahertz output power," *IEEE Trans. Microw. Theory Tech.*, vol. 45, no. 8, pp. 1301–1309, 1997.

[65] E. R. Brown, F. W. Smith, and K. A. Mcintosh, "Coherent millimeter-wave generation by heterodyne conversion in low-temperature-grown GaAs photoconductors," *J. Appl. Phys.*, vol. 73, no. 3, pp. 1480–1484, 1993.

[66] T. Nagatsuma, H. Ito, and T. Ishibashi, "High-power RF photodiodes and their applications," *Laser Photonics Rev.*, vol. 3, no. 1–2, pp. 123–137, 2009.

[67] K. Kato, "Ultrawide-band/high-frequency photodetectors," *IEEE Trans. Microw. Theory Tech.*, vol. 47, no. 7, pp. 1265–1281, Jul. 1999.

[68] C. Renaud, M. Robertson, D. Rogers, R. Firth, P. Cannard, R. Moore, and A. Seeds, "A high responsivity, broadband waveguide uni-travelling carrier photodiode," *Proc. SPIE*, vol. 6194, no. 1, pp. C1940–C1940, 2006.

[69] D. Saeedkia and S. Safavi-Naeini, "Terahertz Photonics: Optoelectronic Techniques for Generation and Detection of TerahertzWaves," *J. Light. Technol.*, vol. 26, no. 15, pp. 3–27, 2008.

[70] V. H. Calle and E. A. Michael, "Free-electron THz-reabsorption in distributed photodiode structures," *J. Phys. D. Appl. Phys.*, vol. 48, no. 39, p. 395104, Oct. 2015.

[71] C. Barrientos Z., V. Calle, M. Diaz, F. P. Mena, J. Vukusic, J. Stake, E. a. Michael, and C. Barrientos, "Vertically illuminated TW-UTC photodiodes for terahertz generation," in *Millimeter, Submillimeter, and Far-Infrared Detectors and Instrumentation for Astronomy V*, 2010, vol. 7741, no. 1, p. 77412L–6.

[72] A. Beck, G. Ducournau, M. Zaknoune, E. Peytavit, T. Akalin, F. Mollot, F. Hindle, C. Yang, and G. Mouret, "High-efficiency uni-travelling-carrier photomixer at 1.55 μm and spectroscopy application up to 1.4 THz," *Electron. Lett.*, vol. 44, no. 22, pp. 1320–1321, 2008.

[73] H.-J. Song;, K. Ajito, Y. Muramoto, A. Wakatsuki, T. Nagatsuma, and N. Kukutsu, "Uni-Travelling-Carrier Photodiode Module Generating 300 GHz Power Greater Than 1 mW," *Microw. Wirel. Components Lett. IEEE*, vol. 22, no. 7, pp. 363–365, 2012.

[74] F. Nakajima, T. Furuta, and H. Ito, "High-power continuous-terahertz-wave generation using resonant-antenna-integrated uni-travelling-carrier photodiode," *Electron. Lett.*, vol. 40, no. 20, pp. 1297–1298, 2004.

[75] H. Ito, T. Furuta, S. Kodama, S. Watanabe, and T. Ishibashi, "InP/lnGaAs uni-travelling-carrier photodiode with 220GHz bandwidth," *Electron. Lett.*, vol. 35, no. 18, pp. 1556–1557, 1999.

[76] T. J. Maloney and J. Frey, "Transient and steady-state electron transport properties of GaAs and InP," *J. Appl. Phys.*, vol. 48, no. 2, p. 781, 1977.

[77] Synopsys, "Sentaurus™ Device User Guide," *System*, no. September. Synopsys, p. 1536, 2014.

[78] D. Pasalic and R. Vahldieck, "Hybrid drift-diffusion-TLM analysis of high-speed and high-output UTC traveling-wave photodetectors," *Int. J. Numer. Model. Electron. Networks, Devices Fields*, vol. 21, no. 1–2, pp. 61–76, 2007.

[79] D. Vasileska and S. M. Goodnick, *Computational Electronics : Semiclassical and quantum device modeling and simulation*, vol. 1, no. 1. 2006.

[80] S. M. M. Rahman, H. Hjelmgren, J. Vukusic, J. Stake, P. A. Andrekson, and H. Zirath, "Hydrodynamic Simulations of Unitraveling-Carrier Photodiodes," *IEEE J. Quantum Electron.*, vol. 43, no. 11, pp. 1088–1094, Nov. 2007.

[81] S. Srivastava, "Simulation Study of In-Based Uni-Traveling Carrier Photodiode," University of Cincinnati, 2003.

[82] S. R. Tatavarti, S. P. Watkins, C. R. Bolognesi, S. Demiguel, and J. C. Campbell, "Demonstration of high-speed staggered lineup GaAsSb-InP unitraveling carrier photodiodes," *IEEE Photonics Technol. Lett.*, vol. 17, no. 3, pp. 651–653, Mar. 2005.

[83] S. M. Sze and M.-K. Lee, *Semiconductor Devices: Physics and Technology*, 3rd ed. Wiley.

[84] M. Achuthan, *Fundamental of Semiconductor Devices*. 2006.

[85] W. Yu, X. Yang, Y. Liu, R. Mittra, and A. Muto, *Advanced FDTD methods: Parallelization, Acceleration, and Engineering Applications*. Norwood, MA: Artech House, 2011.

[86] "CST STUDIO SUITE help documentation." Computer Simulation Technology, 2014.

[87] L. Ansoft, "AN INTRODUCTION TO HFSS Fundamental Principles, Concepts, and Use." Ansoft, Pittsburgh, p. 88, 2009.

[88] J. H. Lau, *Flip Chip Technologies*, First. McGraw-Hill Professional, 1995.

[89] C. Kopf, G. Kaiblinger-Grujin, H. Kosina, and S. Selberherr, "Influence of dopant species on electron mobility in InP," in *International Conference on Indium Phosphide and Related Materials, 1997.*, 1997, pp. 280–283.

[90] W. S. Marek Wesolowski, "Private Communication." ITME Institute, Warshaw, 2014.

[91] E. a. Michael and M. Mikulics, "Losses from long-living photoelectrons in terahertz-generating continuous-wave photomixers," *Appl. Phys. Lett.*, vol. 100, pp. 1–5, 2012.

[92] J.-H. Son, H.-H. Wang, J. F. Whitaker, and G. . Mourou, "Picosecond pulse propagation on coplanar striplines fabricated on lossy semiconductor substrates: Modeling and experiments," *IEEE Trans. Microw. Theory Tech.*, vol. 41, no. 9, pp. 1574–1580, 1993.

[93] M. Takeda, T. Kojima, A. Saito, and K. Makise, "Evaluation of kinetic-inductance nonlinearity in a single- crystal NbTiN-based coplanar waveguide," in *JJAP Conference Proceedings*, 2015, vol. 4, pp. 1–6.

[94] E. C. Jordan and K. G. Balmain, *Electromagnetic Waves and Radiating Systems*, Second. London: Prentice Hall, 1968.

[95] F. Schnieder, T. Tischler, and W. Heinrich, "Modeling Dispersion and Radiation Characteristics of Conductor-Backed CPW With Finite Ground Width," *IEEE Trans. Microw. Theory Tech.*, vol. 51, no. 1, pp. 137–143, 2003.

[96] J. Zhang, "Attenuation characteristics of coplanar waveguides at subterahertz frequencies," *IEEE Trans. Microw. Theory Tech.*, vol. 53, no. 11, pp. 3281–3287, 2005.

[97] L. Cao, A.-S. Grimault-Jacquin, N. Zerounian, and F. Aniel, "Design and VNA-measurement of coplanar waveguide (CPW) on benzocyclobutene (BCB) at THz frequencies," *Infrared Phys. Technol.*, vol. 63, pp. 157–164, Mar. 2014.

[98] H. Guckel, P. A. Brennan, and I. Palocz, "A Parallel-Plate Waveguide Approach to Microminiaturized, Planar Transmission Lines for Integrated Circuits," *IEEE Trans. Microw. Theory Tech.*, vol. 15, no. 8, pp. 468–476, 1967.

[99] P. Schwab, "Electron-Electron Interactions and Charge Transport in Mesoscopic Conductors," 2002.

[100] J. Zou and A. Balandin, "Phonon heat conduction in a semiconductor nanowire," *J. Appl. Phys.*, vol. 89, no. 5, pp. 2932–2938, 2001.

[101] B. G. Streetman and S. K. Banerjee, *Solid State Electronic Devices*, Sixth. New Delhi: Prentice Hall India, 2009.

[102] NSM, "Semiconductors on NSM," 2016. [Online]. Available: http://www.ioffe.ru/SVA/NSM/Semicond/index.html.

[103] L. W. Molenkamp and M. J. M. de Jong, "Electron-electron-scattering-

induced size effects in a two-dimesional wire," *Physical Review B*, vol. 49, no. 7. p. 5038, 1994.

[104] N. W. Ashcroft and N. D. Mermin, *Solid State Physics*, vol. 2, no. ISBN 0-471-92805-4. 1976.

[105] M. O. Manasreh, *InP and Related Compounds: Materials, Applications and Devices*. CRC Press, 2000.

[106] E. Schöll, *Theory of Transport Properties of Semiconductor Nanostructures*. Springer Science+Business Media Dordrecht, 1998.

Appendix A. Photomixer Circuit Analysis

Figure 1.7 shows a THz photomixer with a small active area and its equivalent electrical model. The photocurrent is given by

$$i_{ph} = \frac{q\eta_e}{\hbar\omega}\left(P_1 + P_2 + 2\sqrt{mP_1P_2}\cos(\omega_2 - \omega_2)t\right) \quad \text{(A.1)}$$

where η_e is the external quantum efficiency, P_1 and P_2 are the optical power of the laser beams. $\omega_2 - \omega_2$ is the frequency difference of the laser beams.

The photoconductance can be written as

$$G_p(t) = G_0(1 + \beta\sin(\omega_{THz}t)\ ) \quad \text{(A.2)}$$

where G_0 is the DC-photoconductance, ω_{THz} is the difference frequency $\omega_2 - \omega_2$, used in equation (A.1), and β is the frequency-dependent parameter given by

$$\beta = \frac{2\sqrt{mP_1P_2}}{(P_1 + P_2)\sqrt{1 + \omega^2\tau^2}} \quad \text{(A.3)}$$

where τ is the carrier lifetime.

At low power levels where the saturation is not an issue, G_0 is given by

$$G_0 = \frac{\mathcal{R}_0 P_{abs}}{V_b} \quad \text{(A.4)}$$

where $\mathcal{R}_0$ is the responsivity as defined in equation (1.3) and P_{abs} is the absorbed optical power. Using Kirchoff's current law at the node between R_d, C, and R_A, we got the following dynamic current equation for the equivalent circuit of the photomixer shown in figure 1.7:

$$G_p(t)V_C + C\frac{dV_C}{dt} = \frac{V_b - V_C}{R_A} \quad \text{(A.5)}$$

where G_p is the photoconductance modulated at angular frequency ω (represented by R_d in Figure 1.7, and they are related by $G_p = 1/R_d$), C the capacitance across the antenna gap, R_A the antenna-radiation resistance and V_b is the DC bias voltage.

$$C\frac{dV_C}{dt} + \left[G(t) + \frac{1}{R_A}\right]V_C = \frac{V_b}{R_A} \quad \text{(A.6)}$$

where the photoconductance is expressed by equation (A.2).

The steady-state first harmonic solution to equation (A.6) can be written as

$$V_c(t) = V_0 + V_1 \sin(\omega t + \phi) + V_2 \cos(\omega t + \phi) \tag{A.7}$$

with

$$V_0 = \frac{[(1 + G_0 R_A)^2 + (\omega R_A C)^2]}{(1 + G_0 R_A)\left[(1 + G_0 R_A)^2 + (\omega R_A C)^2 - \frac{1}{2}(G_0 R_A \beta)^2\right]} V_b \tag{A.8}$$

$$V_1 = \frac{G_0 R_A \beta}{(1 + G_0 R_A)^2 + (\omega R_A C)^2 - \frac{1}{2}(G_0 R_A \beta)^2} V_b \tag{A.9}$$

$$V_2 = \frac{(\omega R_A C)(G_0 R_A \beta)}{(1 + G_0 R_A)\left[(1 + G_0 R_A)^2 + (\omega R_A C)^2 - \frac{1}{2}(G_0 R_A \beta)^2\right]} V_b \tag{A.10}$$

The delivered THz power to the antenna is

$$\begin{aligned} P_{THz} &= \frac{1}{2R_A}[V_1^2 + V_2^2] \\ &= \frac{\frac{1}{2}(V_b G_0 \beta)^2 R_A [(1 + G_0 R_A)^2 + (\omega R_A C)^2]}{(1 + G_0 R_A)\left[(1 + G_0 R_A)^2 + (\omega R_A C)^2 - \frac{1}{2}(G_0 R_A \beta)^2\right]} \end{aligned} \tag{A.11}$$

When $G_0 R_A \ll 1$, equation (A.11) reduces to

$$P_{THz} = \frac{1}{2} V_b^2 \frac{G_0^2 R_A}{1 + (\omega R_A C)^2} \frac{1}{1 + \omega^2 \tau^2} \tag{A.12}$$

The DC photocurrent is $I_{ph} = G_0 V_b$, the output THz-radiation power P_{THz} is transformed finally into,

$$P_{THz} = \frac{I_{ph}^2 R_A}{2(1 + \omega^2 \tau^2)(1 + (\omega R_A C)^2)} \tag{A.13}$$

Appendix B. Appendix: Optical heterodyne power

The optical photocurrent is given by

$$I_{ph}(t) = I_{DC} + I_{THz}(t) \tag{B.1}$$

Where $I_{DC}(t)$ is the DC component, $I_{THz}(t)$ is given by

$$I_{THz}(t) \ = 2\mathcal{R}_{THz} \cdot \sqrt{mP_1P_2}\cos\{\omega_{THz}t\} \tag{B.2}$$

The RMS photocurrent $I_{ph_{RMS}}$ is,

$$I_{ph_{RMS}}{}^2 = \frac{1}{T}\int_0^T |I_{THz}(t)|^2 dt = \frac{1}{T}\int_{T_1}^{T_2} \left|2\mathcal{R}_{THz} \cdot \sqrt{mP_1P_2}\cos\{\omega_{THz}t\}\right|^2 dt \tag{B.3}$$

The squared complex modulus of the THz photocurrent is computed as:

$$|I_{THz}(t)|^2 = \left(I_{THz}(t)\right)\overline{\left(I_{ph}(t)\right)} \tag{B.4}$$

Replacing equation (B.2) in (B.4), and this one in (B.3) yields,

$$I_{ph_{RMS}}{}^2 = \frac{2mP_1P_2\mathcal{R}_0^2}{[1+(\tau_{el}\omega)^2][1+(\tau_{RC}\omega)^2]} \tag{B.5}$$

Then, the THz power is given by,

$$P_{THz} = \tfrac{1}{2}R_A I_{ph_{RMS}}{}^2 \tag{B.6}$$

Replacing equation(B.5) in (B.6) yields,

$$P_{THz} = \frac{mP_1P_2\mathcal{R}_0^2R_A}{[1+(\tau_{el}\omega)^2][1+(\tau_{RC}\omega)^2]} \tag{B.7}$$

Because $P^2 = P_1P_2$, $P_1 > 0$ and, $P_2 > 0$, equation (B.7) is simplified as:

$$P_{THz} = \frac{mR_A(\mathcal{R}_0P)^2}{[1+(\tau_{el}\omega)^2][1+(\tau_{RC}\omega)^2]} \tag{B.8}$$

Appendix C. Relevant Scattering lengths

The electron-phonon scattering length is calculated as [99]:

$$L_{e-ph} = \sqrt{D_e \tau_{e-ph}} \tag{C.1}$$

where D_e is the coefficient diffusion for electrons, τ_{e-ph} is the electron-phonon scattering time which is calculated as [100]:

$$\frac{1}{\tau_{e-ph}} = \frac{n_e \epsilon_1^2 \omega}{\rho V^2 k_B T} \sqrt{\frac{\pi m^* V^2}{2 k_B T}} \exp\left(-\frac{m^* V^2}{2 k_B T}\right) \tag{C.2}$$

where n_e is the concentration of conduction electrons, ϵ_1 is the deformation potential, ρ is the mass density, m^* is the effective mass, V is the phonon group velocity, ω is the phonon frequency, k_B is the Boltzmann equation, T is the temperature. The electron conductions for InP was assumed to be equal to InGaAs Absorption layer because it is assumed that there is not electron-phonon pairs and it is calculated by the mass action law ($n_0 \cong n_i^2/N_A$, were n_0 is the minority carriers concentration, n_i the intrinsic carrier concentration and, N_A the concentration of aceptor atoms) [101, pp. 90–95].

Table Appendix C.1. Value parameters and results used in equation (C.1) and (C.2).

	units	$In_{1-x}Ga_xAs$	InP
n_i	cm^{-3}	6.3×10^{11}	1.3×10^{7}
n_e	cm^{-3}	4.0×10^{9}	4.0×10^{9}
ϵ_1	eV	7	7
ρ	g/cm^3	5.5	4.81
m^*	Kg	3.7×10^{-32}	7.28×10^{-32}
V	cm/s	3.7×10^{-32}	3.7×10^{-32}
T	K	300	300
ω	Hz	7.2×10^{12}	9.95×10^{12}
D_e	cm^2/s	300	130
τ_{e-ph}	s	8.1×10^{-15}	3.9×10^{-15}
L_{e-ph}	m	1.6×10^{-8}	7.1×10^{-9}

The data were obtained from reference [102].

The electron-electron scattering length is calculated as [103]:

$$L_{e-e} = v_F \tau_{e-e} \tag{C.3}$$

where v_F is the Fermi velocity, τ_{e-e} is the electron-electron scattering time and it is calculated as [103]:

$$\frac{1}{\tau_{e-e}} = \frac{E_F}{h}\left(\frac{k_B T}{E_F}\right)^2 \left[\ln\left(\frac{E_F}{k_B T}\right) + \ln\left(\frac{2q}{k_F}\right) + 1\right] \tag{C.4}$$

Here q is the 2D Thomas-Fermi screening wave vector ($q = m^* e^2 / 2\pi\varepsilon_r \varepsilon_0 \hbar^2$), E_F is the Fermi-level energy, k_F is the Fermi wave vector ($k_F = (9\pi/4)^{1/3}/r_s$, with $r_s = (3/4\pi n)^{1/3}$ and, n the number of conduction electrons per cubic centimeter[104]). The Fermi velocity is calculated as $v_F = \hbar k_F / m^*$[105, p. 333] [106, p. 13]. The Fermi energy value used here was the intrinsic value because it was impossible to get real Fermi values for doped-semiconductors in literature. The Fermi level was calculated as:

$$E_F = \frac{E_g}{2} + \frac{k_B T}{2} \ln\left(\frac{N_V}{N_C}\right) \tag{C.5}$$

where E_g is the energy bandgap, N_V and N_C are the effective density of states for the valence and conduction bands.

Table Appendix C.2. Value parameters and results used in equation (C.3) and (C.4).

	units	$In_{0.53}Ga_{0.47}As$	InP
N	cm^{-3}	1×10^{18}	1×10^{16}
n	cm^{-3}	1×10^{18}	1×10^{16}
N_C	cm^{-3}	2.1×10^{17}	5.7×10^{17}
N_V	cm^{-3}	7.7×10^{18}	1.1×10^{19}
n_i	cm^{-3}	6.3×10^{11}	8.6×10^{7}
T	K	300	300
τ_{e-e}	s	2.0×10^{-13}	3.1×10^{-13}
L_{e-e}	m	1.3×10^{-9}	1.0×10^{-9}

Appendix D. Analytical model

Figure Appendix D-1a shows the transversal section of a Coplanar Waveguide where inside this is represented the conductance and the capacitance. The piece of waveguide of infinitesimal length Δz of Figure Appendix D-1a can be modeled as a lumped-element circuit, as shown in Figure Appendix D-1b, where R, L, G, C per unit length quantities defined as follows:

R_1 and R_2 = series resistances per unit length, for both conductors, in Ω/m.

L_1 and L_2 = series inductances per unit length, for both striplines conductors, in H/m.

G_1 and G_2 = shunt conductances per unit length, in S/m.
C_1 and C_2 = shunt capacitances per unit length, in F/m.

The series inductance L_1 and L_2 represent the total self-inductance of the two stripline conductors, and the shunt capacitance C_1 and C_2 is due to the close proximity of the stripline conductors. The series resistances R_1 and R_2 represents the resitance due to the finite conductivity of the conductors, and the shunt conductances G_1 and G_2 is due to dielectric loss in the material between the conductors. A finite length of waveguide can be viewed as a cascade of sections of the form shown in Figure Appendix D-1b.

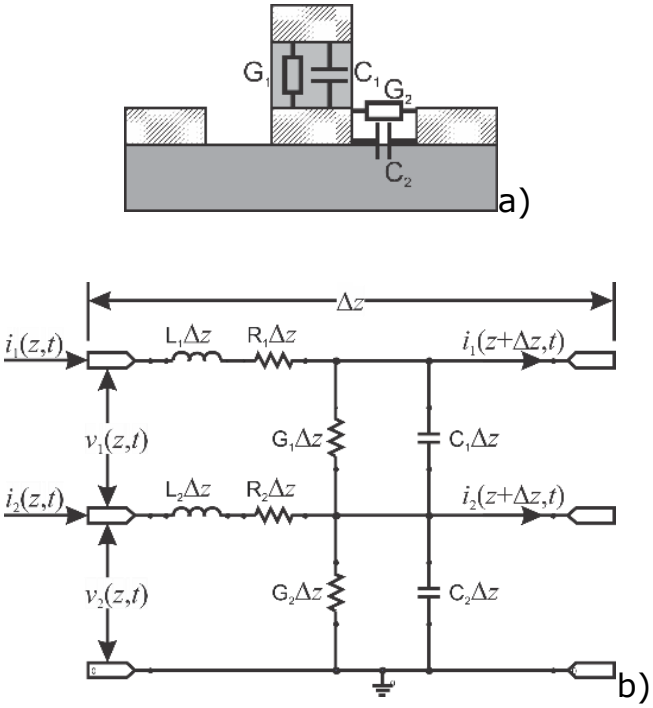

Figure Appendix D-1. a) Conductance and capacitance represented on the waveguide. b) Voltage and current definitions and equivalent circuit for an incremental length of transmission line.

Taking as a reference the Figure Appendix D-2, applying the Kirchhoff's voltage law to the mesh for the current i_a, the following equations:

$$-v_1(z,t)+L_1\Delta z\frac{\partial i_a}{\partial t}+R_1\Delta Z i_a+v_1(z+\Delta z,t)+R_2\Delta z(i_a-i_b)+L_2\Delta z\frac{\partial(i_a-i_b)}{\partial t}=0 \quad (1.1)$$

$$i_1=i_a \quad (1.2)$$

$$i_a=i_2+i_b \quad (1.3)$$

Equation (1.2) is replaced in (1.3) and this result together equation (1.2) is replaced in equation (1.1) to get:

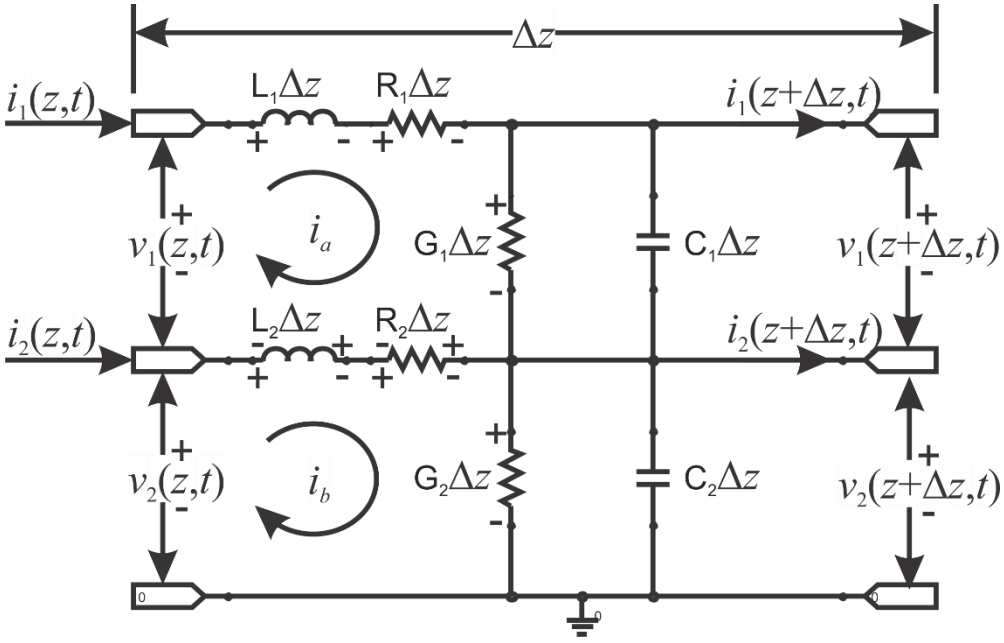

Figure Appendix D-2. Kirchhoff's voltage law circuit.

$$-v_1(z,t)+L_1\Delta z\frac{\partial i_1}{\partial t}+R_1\Delta Z i_1+v_1(z+\Delta z,t)+R_2\Delta z(i_1-i_1+i_2)+L_2\Delta z\frac{\partial(i_1-i_1+i_2)}{\partial t}=0 \quad (1.4)$$

Therefore, after symplifying equation (1.4) the next equation follows:

$$-v_1(z,t)+L_1\Delta z\frac{\partial i_1}{\partial t}+R_1\Delta Z i_1+v_1(z+\Delta z,t)+R_2\Delta z i_2+L_2\Delta z\frac{\partial i_2}{\partial t}=0 \quad (1.5)$$

Equation (1.5) is rewritten as follow:

$$v_1(z+\Delta z,t)-v_1(z,t)=-L_1\Delta z\frac{\partial i_1}{\partial t}-R_1\Delta Z i_1-R_2\Delta z i_2-L_2\Delta z\frac{\partial i_2}{\partial t} \quad (1.6)$$

Equation (1.6) is divided by Δz:

$$\frac{v_1(z+\Delta z,t)-v_1(z,t)}{\Delta z}=\frac{-L_1\Delta z\frac{\partial i_1}{\partial t}-R_1\Delta Z i_1-R_2\Delta z i_2-L_2\Delta z\frac{\partial i_2}{\partial t}}{\Delta z} \quad (1.7)$$

Equation (1.7) is simplified:

$$\frac{v_1(z+\Delta z,t)-v_1(z,t)}{\Delta z}=-L_1\frac{\partial i_1}{\partial t}-R_1 i_1-R_2 i_2-L_2\frac{\partial i_2}{\partial t} \quad (1.8)$$

The limit when Δz tends to 0 is applied to equation (1.8):

$$\lim_{\Delta z\to 0}\left(\frac{v_1(z+\Delta z,t)-v_1(z,t)}{\Delta z}\right)=\lim_{\Delta z\to 0}\left(-L_1\frac{\partial i_1}{\partial t}-R_1 i_1-R_2 i_2-L_2\frac{\partial i_2}{\partial t}\right) \quad (1.9)$$

The first differential equation as a part of a set of differential equations is defined from equation (1.9):

$$\boxed{\frac{\partial v_1}{\partial z}=-L_1\frac{\partial i_1}{\partial t}-R_1 i_1-R_2 i_2-L_2\frac{\partial i_2}{\partial t}} \quad (1.10)$$

A similar procedure is applied for the mesh of the current i_b. Therefore, after applying the Kirchhoff's voltage law, the following equation is obtained:

$$-v_2(z,t)+L_2\Delta z\frac{\partial(i_b-i_a)}{\partial t}+R_2\Delta Z(i_b-i_a)+v_2(z+\Delta z,t)=0 \quad (1.11)$$

$$i_1=i_a \quad (1.12)$$

$$i_a=i_2+i_b \quad (1.13)$$

Therefore,

(1.14)

Replacing equations (1.12) and (1.14) in equation (1.11) to get:

$$-v_2(z,t)+L_2\Delta z\frac{\partial(-i_2)}{\partial t}+R_2\Delta z(-i_2)+v_2(z+\Delta z,t)=0 \quad (1.15)$$

Simplifying and rewriting:

$$-v_2(z,t)-L_2\Delta z\frac{\partial(i_2)}{\partial t}-R_2\Delta z(i_2)+v_2(z+\Delta z,t)=0$$

$$v_2(z+\Delta z,t)-v_2(z,t)=L_2\Delta z\frac{\partial(i_2)}{\partial t}+R_2\Delta z(i_2) \quad (1.16)$$

Equation (1.16) is divided by Δz:

$$\frac{v_2(z+\Delta z,t)-v_2(z,t)}{\Delta z}=\frac{L_2\Delta z\frac{\partial(i_2)}{\partial t}+R_2\Delta z(i_2)}{\Delta z} \quad (1.17)$$

Equation (1.17) is simplified:

$$\frac{v_2\left(z+\Delta z,t\right)-v_2\left(z,t\right)}{\Delta z}=L_2\frac{\partial i_2}{\partial t}+R_2 i_2 \qquad (1.18)$$

The limit when Δz tends to 0 is applied to equation (1.18):

$$\lim_{\Delta z\to 0}\left(\frac{v_2\left(z+\Delta z,t\right)-v_2\left(z,t\right)}{\Delta z}\right)=\lim_{\Delta z\to 0}\left(L_2\frac{\partial i_2}{\partial t}+R_2 i_2\right) \qquad (1.19)$$

Finally the last equation is:

$$\boxed{\frac{\partial v_2}{\partial z}=L_2\frac{\partial i_2}{\partial t}+R_2 i_2} \qquad (1.20)$$

Taking Figure Appendix D-3 as a reference and seeing that this is a modified plot of Figure Appendix D-3 and applying Kirchhoff's current law circuit to the node (1) the following equation is obtained:

$$i_1=i_a+i_1\left(z+\Delta z,t\right) \qquad (1.21)$$

Applying Kirchhoff's current law to the node (2):

$$i_a=i_b+i_c=v_1\left(z+\Delta z,t\right)G_1\Delta z+C_1\Delta z\frac{\partial v_1\left(z+\Delta z,t\right)}{\partial t} \qquad (1.22)$$

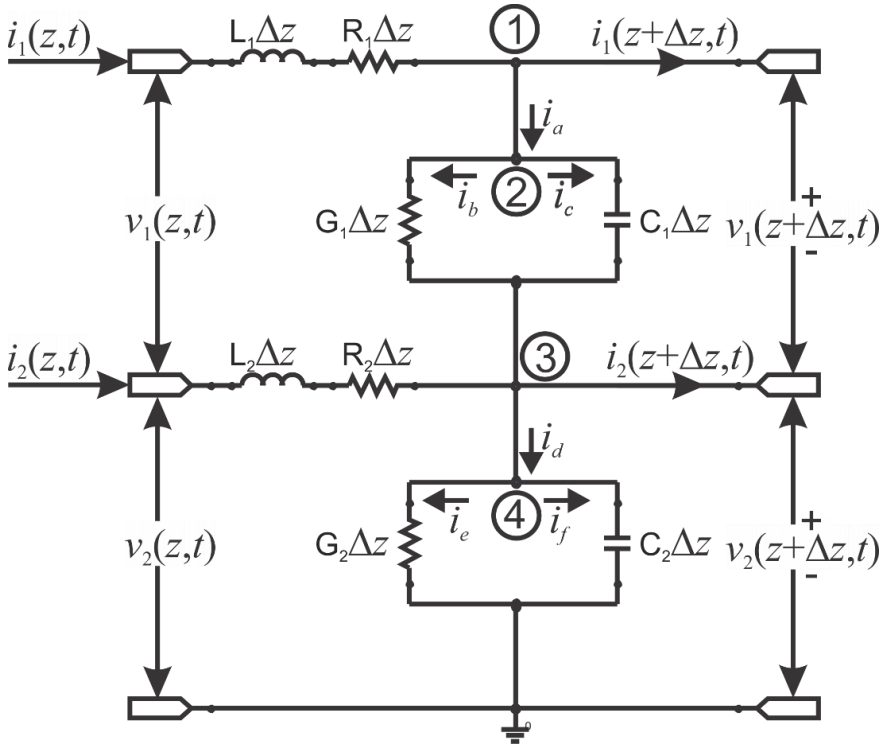

Figure Appendix D-3. Kirchhoff's current law circuit.

Equation (1.22) is replaced in equation (1.21):

$$i_1 = v_1\left(z+\Delta z,t\right)G_1\Delta z + C_1\Delta z\frac{\partial v_1\left(z+\Delta z,t\right)}{\partial t} + i_1\left(z+\Delta z,t\right) \tag{1.23}$$

Equation (1.23) is simplified as follow:

$$i_1\left(z+\Delta z,t\right) - i_1 = -v_1\left(z+\Delta z,t\right)G_1\Delta z - C_1\Delta z\frac{\partial v_1\left(z+\Delta z,t\right)}{\partial t} \tag{1.24}$$

Equation (1.24) is divided by Δz and later it is applied a limit when Δz tends to 0:

$$\lim_{\Delta z\to 0}\left(\frac{i_1\left(z+\Delta z,t\right)-i_1}{\Delta z}\right) = \lim_{\Delta z\to 0}\left(-v_1\left(z+\Delta z,t\right)G_1 - C_1\frac{\partial v_1\left(z+\Delta z,t\right)}{\partial t}\right) \tag{1.25}$$

The third equation is established:

$$\boxed{\frac{\partial i_1}{\partial z} = -G_1 v_1\left(z,t\right) - C_1\frac{\partial v_1\left(z,t\right)}{\partial t}} \tag{1.26}$$

The last equation is obtained using Kirchhoff's current law to the node (3):

$$i_2 + i_a = i_d + i_2\left(z+\Delta z,t\right) \tag{1.27}$$

The equation for the node (4) is:

$$i_d = i_e + i_f = v_2\left(z+\Delta z,t\right)G_2\Delta z + C_2\Delta z\frac{\partial v_2\left(z+\Delta z,t\right)}{\partial t} \tag{1.28}$$

The equations (1.22) and (1.28) is replaced in (1.27)

$$i_2 + v_1\left(z+\Delta z,t\right)G_1\Delta z + C_1\Delta z\frac{\partial v_1\left(z+\Delta z,t\right)}{\partial t} = v_2\left(z+\Delta z,t\right)G_2\Delta z + C_2\Delta z\frac{\partial v_2\left(z+\Delta z,t\right)}{\partial t} + i_2\left(z+\Delta z,t\right)$$

(1.29)

The equation (1.29) is rewritten as:

$$i_2\left(z+\Delta z,t\right) - i_2 = v_1\left(z+\Delta z,t\right)G_1\Delta z + C_1\Delta z\frac{\partial v_1\left(z+\Delta z,t\right)}{\partial t} - v_2\left(z+\Delta z,t\right)G_2\Delta z - C_2\Delta z\frac{\partial v_2\left(z+\Delta z,t\right)}{\partial t}$$

(1.30)

The equation (1.30) is divided by Δz and a limit when Δz tends to zero:

$$\lim_{\Delta z\to 0}\left(\frac{i_2\left(z+\Delta z,t\right)-i_2}{\Delta z}\right)=\lim_{\Delta z\to 0}\left(G_1 v_1\left(z+\Delta z,t\right)+C_1\frac{\partial v_1\left(z+\Delta z,t\right)}{\partial t}-G_2 v_2\left(z+\Delta z,t\right)-C_2\frac{\partial v_2\left(z+\Delta z,t\right)}{\partial t}\right)$$

(1.31)

Evaluating the limit finally is the last equation:

$$\boxed{\frac{\partial i_2}{\partial z}=G_1 v_1\left(z,t\right)+C_1\frac{\partial v_1\left(z,t\right)}{\partial t}-G_2 v_2\left(z,t\right)-C_2\frac{\partial v_2\left(z,t\right)}{\partial t}} \quad (1.32)$$

Therefore, the following equation set is established:

$$\frac{\partial v_1(z,t)}{\partial z}=-L_1\frac{\partial i_1(z,t)}{\partial t}-R_1 i_1(z,t)-R_2 i_2(z,t)-L_2\frac{\partial i_2(z,t)}{\partial t} \quad (1.33)$$

$$\frac{\partial v_2(z,t)}{\partial z}=L_2\frac{\partial i_2(z,t)}{\partial t}+R_2 i_2(z,t) \quad (1.34)$$

$$\frac{\partial i_1(z,t)}{\partial z}=-G_1 v_1\left(z,t\right)-C_1\frac{\partial v_1\left(z,t\right)}{\partial t} \quad (1.35)$$

$$\frac{\partial i_2(z,t)}{\partial z}=G_1 v_1\left(z,t\right)+C_1\frac{\partial v_1\left(z,t\right)}{\partial t}-G_2 v_2\left(z,t\right)-C_2\frac{\partial v_2\left(z,t\right)}{\partial t} \quad (1.36)$$

These equations are the time domain form of the transmission line, or telegrapher, equations. For the sinusoidal steady-state condition, with cosine-based phasors, equations (1.33) to (1.36) simplify to:

$$\frac{dV_1(z)}{dz}=-\left(j\omega L_1+R_1\right)I_1\left(z\right)-\left(j\omega L_2+R_2\right)I_2\left(z\right) \quad (1.37)$$

$$\frac{dV_2\left(z\right)}{dz}=\left(j\omega L_2+R_2\right)I_2\left(z\right) \quad (1.38)$$

$$\frac{dI_1\left(z\right)}{dz}=-\left(G_1+j\omega C_1\right)V_1\left(z\right) \quad (1.39)$$

$$\frac{dI_2\left(z\right)}{dz}=\left(G_1+j\omega C_1\right)V_1\left(z\right)-\left(G_2+j\omega C_2\right)V_2\left(z\right) \quad (1.40)$$

The partial differential equations system (1.37) - (1.40) can be written in vectorial notation as follows. A matrix $A(z)$:

$$A(z)=\begin{bmatrix} 0 & 0 & -(j\omega L_1+R_1) & -(j\omega L_2+R_2) \\ 0 & 0 & 0 & (j\omega L_2+R_2) \\ -(G_1+j\omega C_1) & 0 & 0 & 0 \\ (G_1+j\omega C_1) & -(G_2+j\omega C_2) & 0 & 0 \end{bmatrix} \quad (1.41)$$

The vector **X** and its derivative **X'** is written as:

$$\mathbf{x}=\begin{bmatrix} V_1(z) \\ V_2(z) \\ I_1(z) \\ I_2(z) \end{bmatrix} \quad (1.42)$$

$$\mathbf{x}'=\begin{bmatrix} \frac{dV_1(z)}{dz} \\ \frac{dV_2(z)}{dz} \\ \frac{dI_1(z)}{dz} \\ \frac{dI_2(z)}{dz} \end{bmatrix} \quad (1.43)$$

Therefore, the partial differential equations system (1.37) - (1.40):

$$\mathbf{x}'(z)=\mathbf{A}(z)\mathbf{x}(z) \quad (1.44)$$

The MuPAD solver was used:

The partial differential equations system (1.37) - (1.40) can be written in vectorial notation as follows. A matrix $A(z)$:

$$A(z)=\begin{bmatrix} 0 & 0 & -(j\omega L_1+R_1) & -(j\omega L_2+R_2) \\ 0 & 0 & 0 & (j\omega L_2+R_2) \\ -(G_1+j\omega C_1) & 0 & 0 & 0 \\ (G_1+j\omega C_1) & -(G_2+j\omega C_2) & 0 & 0 \end{bmatrix} \quad (1.45)$$

By setting the following equivalences:

$$\begin{aligned} A &= -(j\omega L_1+R_1) \\ B &= -(j\omega L_2+R_2) \\ C &= -(G_1+j\omega C_1) \\ D &= -(G_2+j\omega C_2) \end{aligned} \quad (1.46)$$

Equation is re-written as:

$$A(z)=\begin{bmatrix} 0 & 0 & A & B \\ 0 & 0 & 0 & -B \\ C & 0 & 0 & 0 \\ -C & D & 0 & 0 \end{bmatrix} \tag{1.47}$$

The vector **X** and its derivative **X'** is written as:

$$\mathbf{x}=\begin{bmatrix} V_1(z) \\ V_2(z) \\ I_1(z) \\ I_2(z) \end{bmatrix} \tag{1.48}$$

$$\mathbf{x}'=\begin{bmatrix} \frac{dV_1(z)}{dz} \\ \frac{dV_2(z)}{dz} \\ \frac{dI_1(z)}{dz} \\ \frac{dI_2(z)}{dz} \end{bmatrix} \tag{1.49}$$

Therefore, the partial differential equations system (1.37) - (1.40):

$$\mathbf{x}'(z)=\mathbf{A}(z)\mathbf{x}(z) \tag{1.50}$$

In order to solve equation (1.44), the characteristic polynomial:

$$\det(\lambda\mathbf{I}-\mathbf{A}) \tag{1.51}$$

Which solved is given by:

$$\lambda^4+(BC-AC+BD)\lambda^2-ABCD \tag{1.52}$$

Whose roots are:

$$\lambda_1 = -\sqrt{\frac{AC}{2} - \frac{\sqrt{A^2C^2 - 2ABC^2 + 2ABCD + B^2C^2 + 2B^2CD + B^2D^2}}{2} - \frac{BC}{2} - \frac{BD}{2}}$$
$$\lambda_2 = -\sqrt{\frac{\sqrt{A^2C^2 - 2ABC^2 + 2ABCD + B^2C^2 + 2B^2CD + B^2D^2}}{2} + \frac{AC}{2} - \frac{BC}{2} - \frac{BD}{2}} \quad (1.53)$$
$$\lambda_3 = \sqrt{\frac{AC}{2} - \frac{\sqrt{A^2C^2 - 2ABC^2 + 2ABCD + B^2C^2 + 2B^2CD + B^2D^2}}{2} - \frac{BC}{2} - \frac{BD}{2}}$$
$$\lambda_4 = \sqrt{\frac{\sqrt{A^2C^2 - 2ABC^2 + 2ABCD + B^2C^2 + 2B^2CD + B^2D^2}}{2} + \frac{AC}{2} - \frac{BC}{2} - \frac{BD}{2}}$$

The roots (1.53) are the eigenvalues of the matrix (1.45).

The eigenvectors for $\lambda_1, \lambda_2, \lambda_3$ and λ_4 are calculated according to:

$$\left(\lambda_1 \mathbf{I}_4 - \mathbf{A}\right)\mathbf{v} = \mathbf{0} \quad (1.54)$$

For the eigenvalue λ_1, the eigenvector is given by:

$$\mathbf{v}_1 = \begin{bmatrix} \sigma_4 + \sigma_3 \\ \sigma_5 + \sigma_1 \\ \sigma_2 \\ 1 \end{bmatrix} \quad (1.55)$$

With multiplicity 1.

The solution $\boldsymbol{X}_1$ using the eigenvector $\boldsymbol{V}_1$ is calculated as:

$$\mathbf{x}_1\left(z\right) = e^{\lambda_1 z}\mathbf{v}_1 \quad (1.56)$$

For the eigenvalue λ_2, the eigenvector is given by:

$$\mathbf{v}_2 = \begin{bmatrix} \sigma_{10} + \sigma_9 \\ \sigma_{11} + \sigma_6 \\ \sigma_8 \\ 1 \end{bmatrix} \quad (1.57)$$

With multiplicity 1.

The solution $\boldsymbol{X}_2$ using the eigenvector $\boldsymbol{V}_2$ is calculated as:

$$\mathbf{x}_2\left(z\right) = e^{\lambda_2 z}\mathbf{v}_2 \quad (1.58)$$

For the eigenvalue λ_3, the eigenvector is given by:

$$\mathbf{v}_3 = \begin{bmatrix} -\sigma_4 - \sigma_3 \\ -\sigma_5 - \sigma_1 \\ \sigma_2 \\ 1 \end{bmatrix} \tag{1.59}$$

With multiplicity 1.

The solution $\boldsymbol{X}_3$ using the eigenvector $\boldsymbol{V}_3$ is calculated as:

$$\mathbf{x}_3(z) = e^{\lambda_3 z}\mathbf{v}_3 \tag{1.60}$$

For the eigenvalue λ_4, the eigenvector is given by:

$$\mathbf{v}_4 = \begin{bmatrix} -\sigma_{10} - \sigma_9 \\ -\sigma_{11} - \sigma_6 \\ \sigma_8 \\ 1 \end{bmatrix} \tag{1.61}$$

With multiplicity 1.

The solution $\boldsymbol{X}_4$ using the eigenvector $\boldsymbol{V}_4$ is calculated as:

$$\mathbf{x}_4(z) = e^{\lambda_4 z}\mathbf{v}_4 \tag{1.62}$$

The general solution is given by:

$$\mathbf{x}(z) = c_1\mathbf{x}_1(z) + c_2\mathbf{x}_2(z) + c_3\mathbf{x}_3(z) + c_4\mathbf{x}_4(z) \tag{1.63}$$

$$\begin{bmatrix} V_1(z) \\ V_2(z) \\ I_1(z) \\ I_2(z) \end{bmatrix} = c_1 e^{\lambda_1 z}\mathbf{v}_1 + c_2 e^{\lambda_2 z}\mathbf{v}_2 + c_3 e^{\lambda_3 z}\mathbf{v}_3 + c_4 e^{\lambda_4 z}\mathbf{v}_4 \tag{1.64}$$

$$\begin{bmatrix} V_1(z) \\ V_2(z) \\ I_1(z) \\ I_2(z) \end{bmatrix} = c_1 e^{\lambda_1 z}\begin{bmatrix} \sigma_4 + \sigma_3 \\ \sigma_5 + \sigma_1 \\ \sigma_2 \\ 1 \end{bmatrix} + c_2 e^{\lambda_2 z}\begin{bmatrix} \sigma_{10} + \sigma_9 \\ \sigma_{11} + \sigma_6 \\ \sigma_8 \\ 1 \end{bmatrix} + c_3 e^{\lambda_3 z}\begin{bmatrix} -\sigma_4 - \sigma_3 \\ -\sigma_5 - \sigma_1 \\ \sigma_2 \\ 1 \end{bmatrix} + c_4 e^{\lambda_4 z}\begin{bmatrix} -\sigma_{10} - \sigma_9 \\ -\sigma_{11} - \sigma_6 \\ \sigma_8 \\ 1 \end{bmatrix} \tag{1.65}$$

$$\begin{bmatrix} V_1(z) \\ V_2(z) \\ I_1(z) \\ I_2(z) \end{bmatrix} = \begin{bmatrix} c_1 e^{\lambda_1 z}(\sigma_4 + \sigma_3) + c_2 e^{\lambda_2 z}(\sigma_{10} + \sigma_9) + c_3 e^{\lambda_3 z}(-\sigma_4 - \sigma_3) + c_4 e^{\lambda_4 z}(-\sigma_{10} - \sigma_9) \\ c_1 e^{\lambda_1 z}(\sigma_5 + \sigma_1) + c_2 e^{\lambda_2 z}(\sigma_{11} + \sigma_6) + c_3 e^{\lambda_3 z}(-\sigma_5 - \sigma_1) + c_4 e^{\lambda_4 z}(-\sigma_{11} - \sigma_6) \\ c_1 e^{\lambda_1 z}\sigma_2 + c_2 e^{\lambda_2 z}\sigma_8 + c_3 e^{\lambda_3 z}\sigma_2 + c_4 e^{\lambda_4 z}\sigma_8 \\ c_1 e^{\lambda_1 z} + c_2 e^{\lambda_2 z} + c_3 e^{\lambda_3 z} + c_4 e^{\lambda_4 z} \end{bmatrix} \tag{1.66}$$

Where the constants σ_1 to σ_{16} are defined as follow:

$$\sigma_1 = \frac{\sigma_{13}\sqrt{\sigma_{12}}}{ACD}$$
$$\sigma_2 = \frac{\sigma_{16} - \frac{AC}{2} + \frac{BC}{2} + \frac{BD}{2}}{AC} - \frac{\sigma_{14}}{AC}$$
$$\sigma_3 = \frac{\sigma_{14}\sqrt{\sigma_{12}}}{AC^2}$$
$$\sigma_4 = \frac{\sigma_{12}^{3/2}}{AC^2}$$
$$\sigma_5 = \frac{\sigma_{12}^{3/2}}{ACD}$$
$$\sigma_6 = \frac{\sigma_{13}\sqrt{\sigma_{15}}}{ACD}$$
$$\sigma_8 = -\frac{\sigma_{15}}{AC} - \frac{\sigma_{14}}{AC}$$
$$\sigma_9 = \frac{\sigma_{14}\sqrt{\sigma_{15}}}{AC^2}$$
$$\sigma_{10} = \frac{\sigma_{15}^{3/2}}{AC^2}$$
$$\sigma_{11} = \frac{\sigma_{15}^{3/2}}{ACD}$$
$$\sigma_{12} = -\sigma_{16} + \frac{AC}{2} - \frac{BC}{2} - \frac{BD}{2} \qquad (1.67)$$
$$\sigma_{13} = BC - AC + BD$$
$$\sigma_{14} = BC + BD$$
$$\sigma_{15} = \sigma_{16} + \frac{AC}{2} - \frac{BC}{2} - \frac{BD}{2}$$
$$\sigma_{16=} \frac{\sqrt{A^2C^2 - 2ABC^2 + 2ABCD + B^2C^2 + 2B^2CD + B^2D^2}}{2}$$

The MuPAD solver was used:

The partial differential equations system (1.37) - (1.40) can be written in vectorial notation as follows. A matrix $A(z)$:

$$A(z) = \begin{bmatrix} 0 & 0 & -(j\omega L_1 + R_1) & -(j\omega L_2 + R_2) \\ 0 & 0 & 0 & (j\omega L_2 + R_2) \\ -(G_1 + j\omega C_1) & 0 & 0 & 0 \\ (G_1 + j\omega C_1) & -(G_2 + j\omega C_2) & 0 & 0 \end{bmatrix} \qquad (1.68)$$

By setting the following equivalences:

$$
\begin{aligned}
A &= -\left(j\omega L_1 + R_1 \right) \\
B &= -\left(j\omega L_2 + R_2 \right) \\
C &= -\left(G_1 + j\omega C_1 \right) \\
D &= -\left(G_2 + j\omega C_2 \right)
\end{aligned}
\tag{1.69}
$$

Equation is re-written as:

$$
A(z) = \begin{bmatrix} 0 & 0 & A & B \\ 0 & 0 & 0 & -B \\ C & 0 & 0 & 0 \\ -C & D & 0 & 0 \end{bmatrix}
\tag{1.70}
$$

The vector **X** and its derivative **X'** is written as:

$$
\mathbf{x} = \begin{bmatrix} V_1(z) \\ V_2(z) \\ I_1(z) \\ I_2(z) \end{bmatrix}
\tag{1.71}
$$

$$
\mathbf{x}' = \begin{bmatrix} \dfrac{dV_1(z)}{dz} \\ \dfrac{dV_2(z)}{dz} \\ \dfrac{dI_1(z)}{dz} \\ \dfrac{dI_2(z)}{dz} \end{bmatrix}
\tag{1.72}
$$

Therefore, the partial differential equations system (1.37) - (1.40):

$$
\mathbf{x}'(z) = \mathbf{A}(z)\mathbf{x}(z)
\tag{1.73}
$$

In order to solve equation (1.44), the characteristic polynomial:

$$
\det\left(\lambda \mathbf{I} - \mathbf{A} \right)
\tag{1.74}
$$

Which solved is given by:

$$
\lambda^4 + \left(BC - AC + BD \right)\lambda^2 - ABCD
\tag{1.75}
$$

Whose roots are:

$$\lambda_1 = -\sqrt{\frac{AC}{2} - \frac{\sqrt{A^2C^2 - 2ABC^2 + 2ABCD + B^2C^2 + 2B^2CD + B^2D^2}}{2} - \frac{BC}{2} - \frac{BD}{2}}$$
$$\lambda_2 = -\sqrt{\frac{\sqrt{A^2C^2 - 2ABC^2 + 2ABCD + B^2C^2 + 2B^2CD + B^2D^2}}{2} + \frac{AC}{2} - \frac{BC}{2} - \frac{BD}{2}} \quad (1.76)$$
$$\lambda_3 = \sqrt{\frac{AC}{2} - \frac{\sqrt{A^2C^2 - 2ABC^2 + 2ABCD + B^2C^2 + 2B^2CD + B^2D^2}}{2} - \frac{BC}{2} - \frac{BD}{2}}$$
$$\lambda_4 = \sqrt{\frac{\sqrt{A^2C^2 - 2ABC^2 + 2ABCD + B^2C^2 + 2B^2CD + B^2D^2}}{2} + \frac{AC}{2} - \frac{BC}{2} - \frac{BD}{2}}$$

The roots (1.53) are the eigenvalues of the matrix (1.45).

The eigenvectors for $\lambda_1, \lambda_2, \lambda_3$ and λ_4 are calculated according to:

$$\left(\lambda_1 \mathbf{I}_4 - \mathbf{A}\right)\mathbf{v} = \mathbf{0} \quad (1.77)$$

For the eigenvalue λ_1, the eigenvector is given by:

$$\mathbf{v}_1 = \begin{bmatrix} \sigma_4 + \sigma_3 \\ \sigma_5 + \sigma_1 \\ \sigma_2 \\ 1 \end{bmatrix} \quad (1.78)$$

With multiplicity 1.

The solution $\boldsymbol{X}_1$ using the eigenvector $\boldsymbol{V}_1$ is calculated as:

$$\mathbf{x}_1\left(z\right) = e^{\lambda_1 z}\mathbf{v}_1 \quad (1.79)$$

For the eigenvalue λ_2, the eigenvector is given by:

$$\mathbf{v}_2 = \begin{bmatrix} \sigma_{10} + \sigma_9 \\ \sigma_{11} + \sigma_6 \\ \sigma_8 \\ 1 \end{bmatrix} \quad (1.80)$$

With multiplicity 1.

The solution $\boldsymbol{X}_2$ using the eigenvector $\boldsymbol{V}_2$ is calculated as:

$$\mathbf{x}_2\left(z\right) = e^{\lambda_2 z}\mathbf{v}_2 \quad (1.81)$$

For the eigenvalue λ_3, the eigenvector is given by:

$$\mathbf{v}_3 = \begin{bmatrix} -\sigma_4 - \sigma_3 \\ -\sigma_5 - \sigma_1 \\ \sigma_2 \\ 1 \end{bmatrix} \tag{1.82}$$

With multiplicity 1.

The solution $\boldsymbol{X}_3$ using the eigenvector $\boldsymbol{V}_3$ is calculated as:

$$\mathbf{x}_3(z) = e^{\lambda_3 z}\mathbf{v}_3 \tag{1.83}$$

For the eigenvalue λ_4, the eigenvector is given by:

$$\mathbf{v}_4 = \begin{bmatrix} -\sigma_{10} - \sigma_9 \\ -\sigma_{11} - \sigma_6 \\ \sigma_8 \\ 1 \end{bmatrix} \tag{1.84}$$

With multiplicity 1.

The solution $\boldsymbol{X}_4$ using the eigenvector $\boldsymbol{V}_4$ is calculated as:

$$\mathbf{x}_4(z) = e^{\lambda_4 z}\mathbf{v}_4 \tag{1.85}$$

The general solution is given by:

$$\mathbf{x}(z) = c_1\mathbf{x}_1(z) + c_2\mathbf{x}_2(z) + c_3\mathbf{x}_3(z) + c_4\mathbf{x}_4(z) \tag{1.86}$$

$$\begin{bmatrix} V_1(z) \\ V_2(z) \\ I_1(z) \\ I_2(z) \end{bmatrix} = c_1 e^{\lambda_1 z}\mathbf{v}_1 + c_2 e^{\lambda_2 z}\mathbf{v}_2 + c_3 e^{\lambda_3 z}\mathbf{v}_3 + c_4 e^{\lambda_4 z}\mathbf{v}_4 \tag{1.87}$$

$$\begin{bmatrix} V_1(z) \\ V_2(z) \\ I_1(z) \\ I_2(z) \end{bmatrix} = c_1 e^{\lambda_1 z}\begin{bmatrix} \sigma_4 + \sigma_3 \\ \sigma_5 + \sigma_1 \\ \sigma_2 \\ 1 \end{bmatrix} + c_2 e^{\lambda_2 z}\begin{bmatrix} \sigma_{10} + \sigma_9 \\ \sigma_{11} + \sigma_6 \\ \sigma_8 \\ 1 \end{bmatrix} + c_3 e^{\lambda_3 z}\begin{bmatrix} -\sigma_4 - \sigma_3 \\ -\sigma_5 - \sigma_1 \\ \sigma_2 \\ 1 \end{bmatrix} + c_4 e^{\lambda_4 z}\begin{bmatrix} -\sigma_{10} - \sigma_9 \\ -\sigma_{11} - \sigma_6 \\ \sigma_8 \\ 1 \end{bmatrix} \tag{1.88}$$

$$\begin{bmatrix} V_1(z) \\ V_2(z) \\ I_1(z) \\ I_2(z) \end{bmatrix} = \begin{bmatrix} c_1 e^{\lambda_1 z}(\sigma_4 + \sigma_3) + c_2 e^{\lambda_2 z}(\sigma_{10} + \sigma_9) + c_3 e^{\lambda_3 z}(-\sigma_4 - \sigma_3) + c_4 e^{\lambda_4 z}(-\sigma_{10} - \sigma_9) \\ c_1 e^{\lambda_1 z}(\sigma_5 + \sigma_1) + c_2 e^{\lambda_2 z}(\sigma_{11} + \sigma_6) + c_3 e^{\lambda_3 z}(-\sigma_5 - \sigma_1) + c_4 e^{\lambda_4 z}(-\sigma_{11} - \sigma_6) \\ c_1 e^{\lambda_1 z}\sigma_2 + c_2 e^{\lambda_2 z}\sigma_8 + c_3 e^{\lambda_3 z}\sigma_2 + c_4 e^{\lambda_4 z}\sigma_8 \\ c_1 e^{\lambda_1 z} + c_2 e^{\lambda_2 z} + c_3 e^{\lambda_3 z} + c_4 e^{\lambda_4 z} \end{bmatrix} \tag{1.89}$$

Where the constants σ_1 to σ_{16} are defined as follow:

$$\sigma_1 = \frac{\sigma_{13}\sqrt{\sigma_{12}}}{ACD}$$

$$\sigma_2 = \frac{\sigma_{16} - \frac{AC}{2} + \frac{BC}{2} + \frac{BD}{2}}{AC} - \frac{\sigma_{14}}{AC}$$

$$\sigma_3 = \frac{\sigma_{14}\sqrt{\sigma_{12}}}{AC^2}$$

$$\sigma_4 = \frac{\sigma_{12}^{3/2}}{AC^2}$$

$$\sigma_5 = \frac{\sigma_{12}^{3/2}}{ACD}$$

$$\sigma_6 = \frac{\sigma_{13}\sqrt{\sigma_{15}}}{ACD}$$

$$\sigma_8 = -\frac{\sigma_{15}}{AC} - \frac{\sigma_{14}}{AC}$$

$$\sigma_9 = \frac{\sigma_{14}\sqrt{\sigma_{15}}}{AC^2}$$

$$\sigma_{10} = \frac{\sigma_{15}^{3/2}}{AC^2}$$

$$\sigma_{11} = \frac{\sigma_{15}^{3/2}}{ACD}$$

$$\sigma_{12} = -\sigma_{16} + \frac{AC}{2} - \frac{BC}{2} - \frac{BD}{2} \qquad (1.90)$$

$$\sigma_{13} = BC - AC + BD$$

$$\sigma_{14} = BC + BD$$

$$\sigma_{15} = \sigma_{16} + \frac{AC}{2} - \frac{BC}{2} - \frac{BD}{2}$$

$$\sigma_{16=} \frac{\sqrt{A^2C^2 - 2ABC^2 + 2ABCD + B^2C^2 + 2B^2CD + B^2D^2}}{2}$$

Appendix E. Supplemental Material

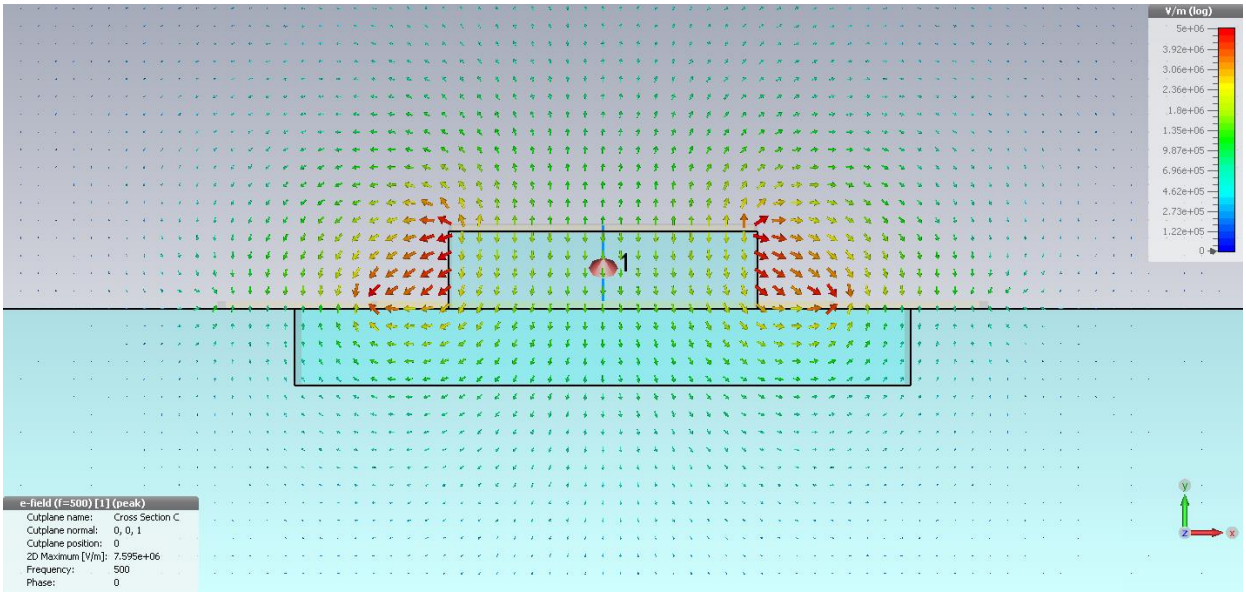

Figure Appendix E-1. Cross sectional representation of the electric field at the center of the transmission line, which have a n-layer doping of 50000 S/m, at a frequency of 500 GHz. The arrows flows symmetrical from the center stripline to the lateral striplines.

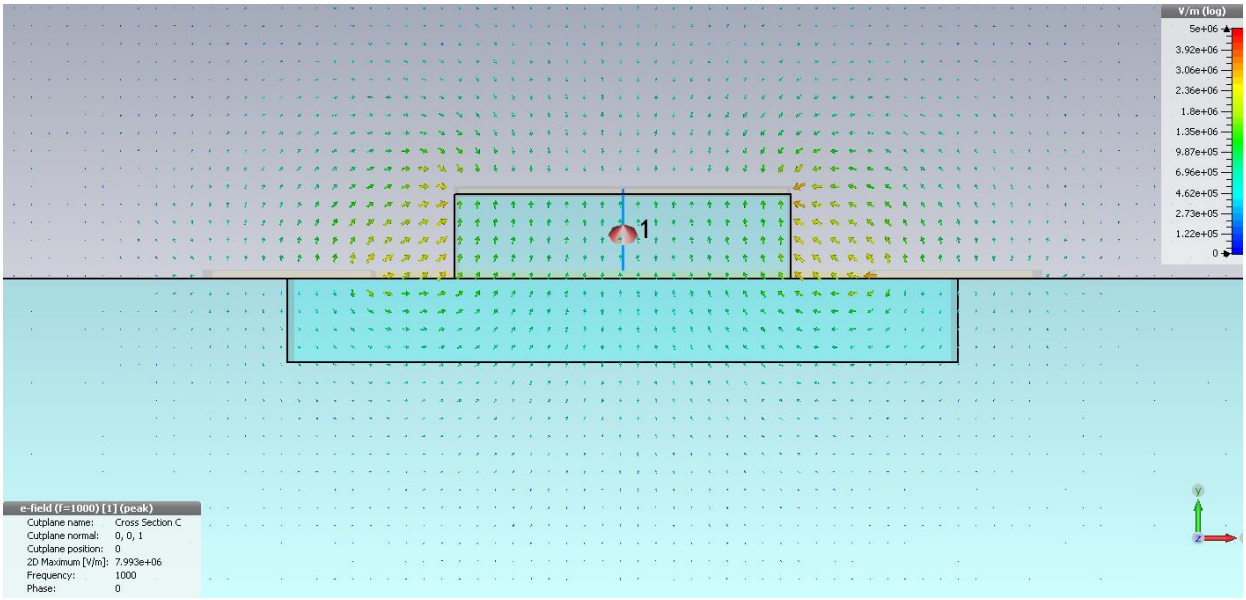

Figure Appendix E-2. Cross sectional representation of the electric field at the center of the transmission line, which have a n-layer doping of 50000 S/m, at a frequency of 1000 GHz. The arrows flows symmetrical from the center stripline to the lateral striplines.

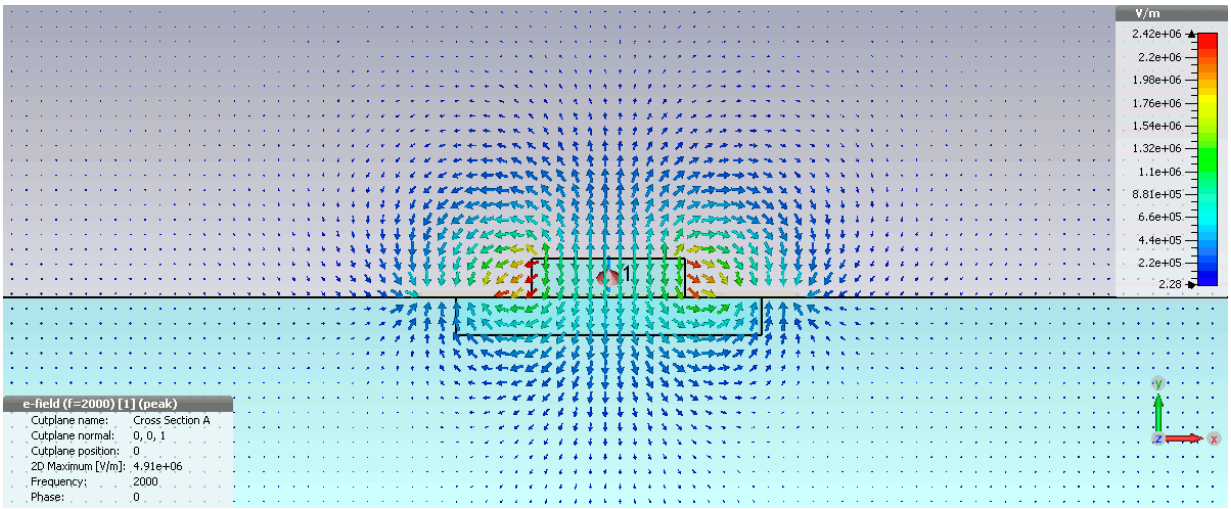

Figure Appendix E-3. Cross sectional representation of the electric field at the center of the transmission line, which have a n-layer doping of 50000 S/m, at a frequency of 2000 GHz. The arrows flows symmetrical from the center stripline to the lateral striplines.

a)

b)

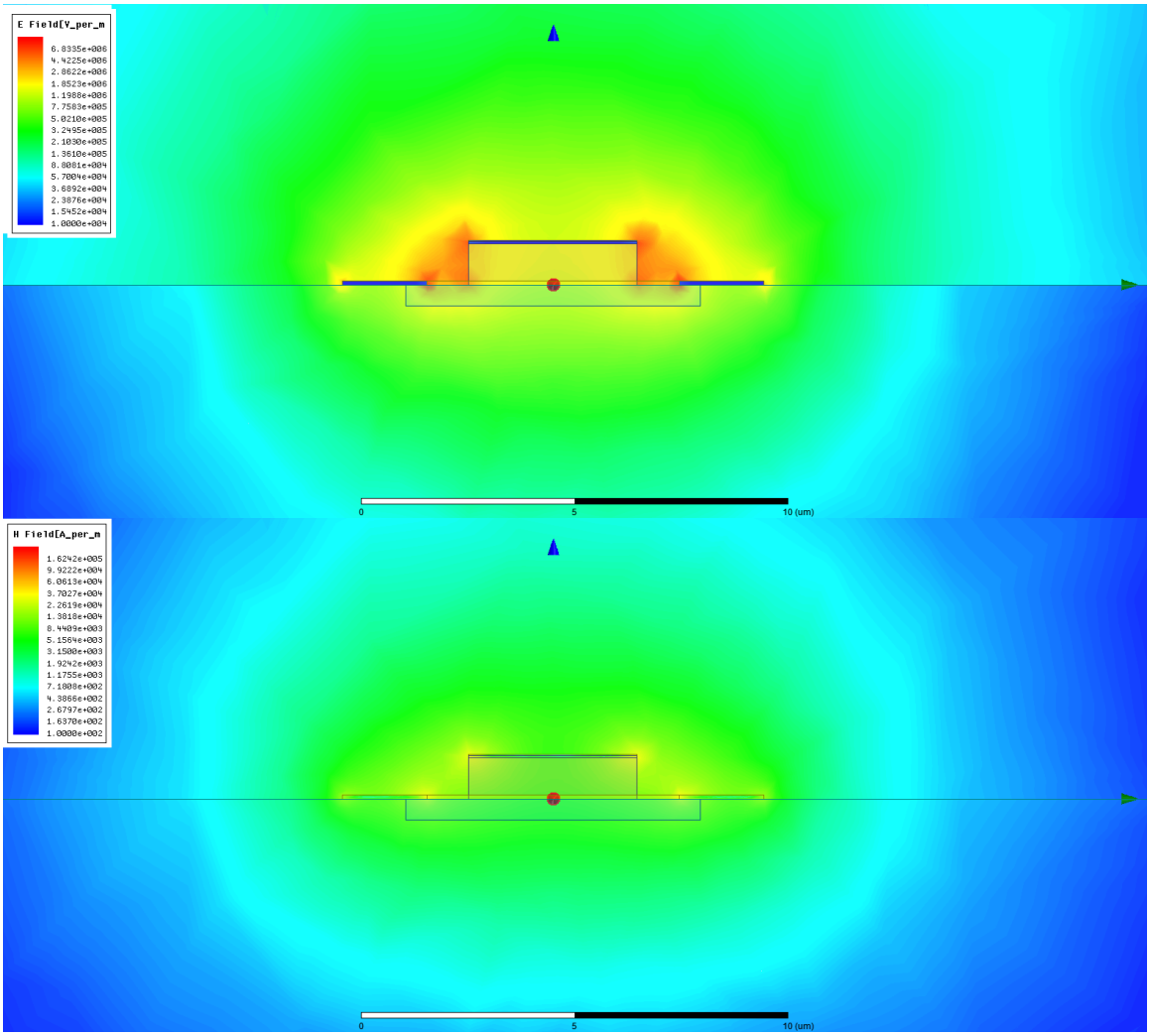

Figure Appendix E-4. Color plot of a cross-section of a UTC-PD device. The image shows an enlarged section of the device where the zoom is applied on the central stripline, lateral striplines, and the n-doped layer. This layer has a conductivity of 1.0×10^{-1} S/m and at a frequency of 100 GHz. a) Electric Field. b) Magnetic Field.

a)

b)

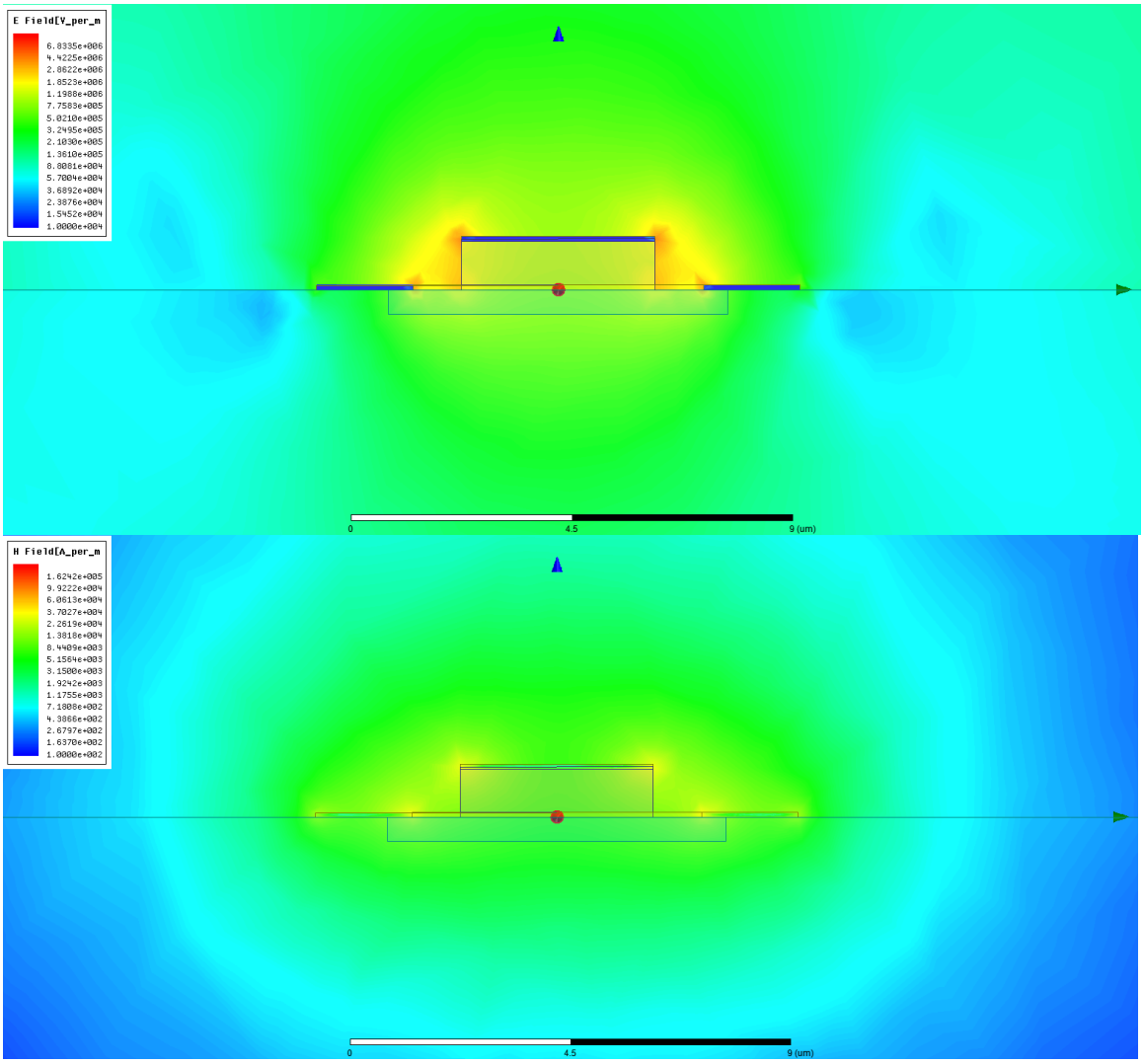

Figure Appendix E-5. Color plot of a cross-section of a UTC-PD device. The image shows an enlarged section of the device where the zoom is applied on the central stripline, lateral striplines, and the n-doped layer. This layer has a conductivity of 2.1×10^3 S/m and at a frequency of 100 GHz. a) Electric Field. b) Magnetic Field.

a)

b)

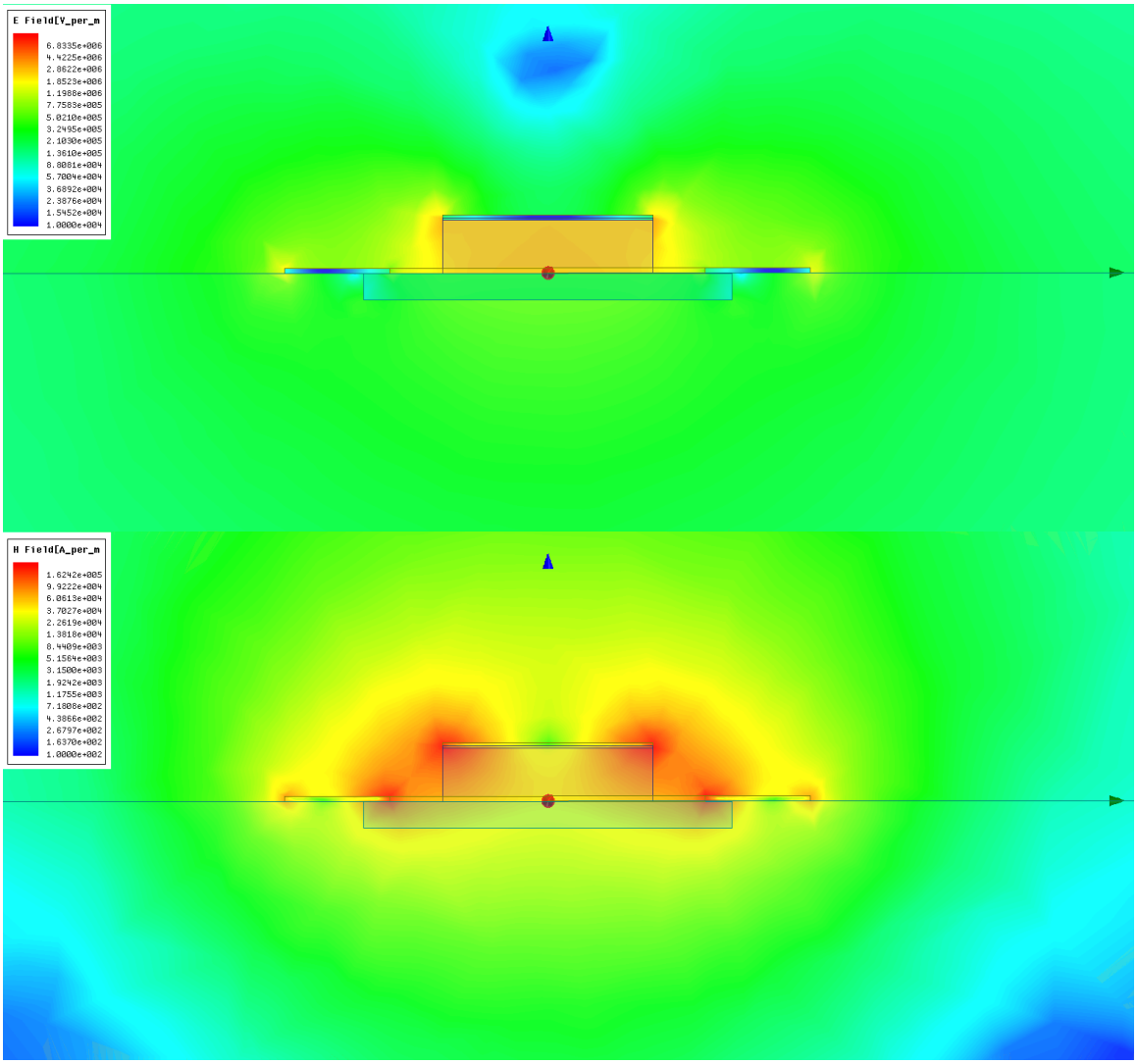

Figure Appendix E-6. Color plot of a cross-section of a UTC-PD device. The image shows an enlarged section of the device where the zoom is applied on the central stripline, lateral striplines, and the n-doped layer. This layer has a conductivity of 5×10^4 S/m and at a frequency of 100 GHz. a) Electric Field. b) Magnetic Field.

a)

b)

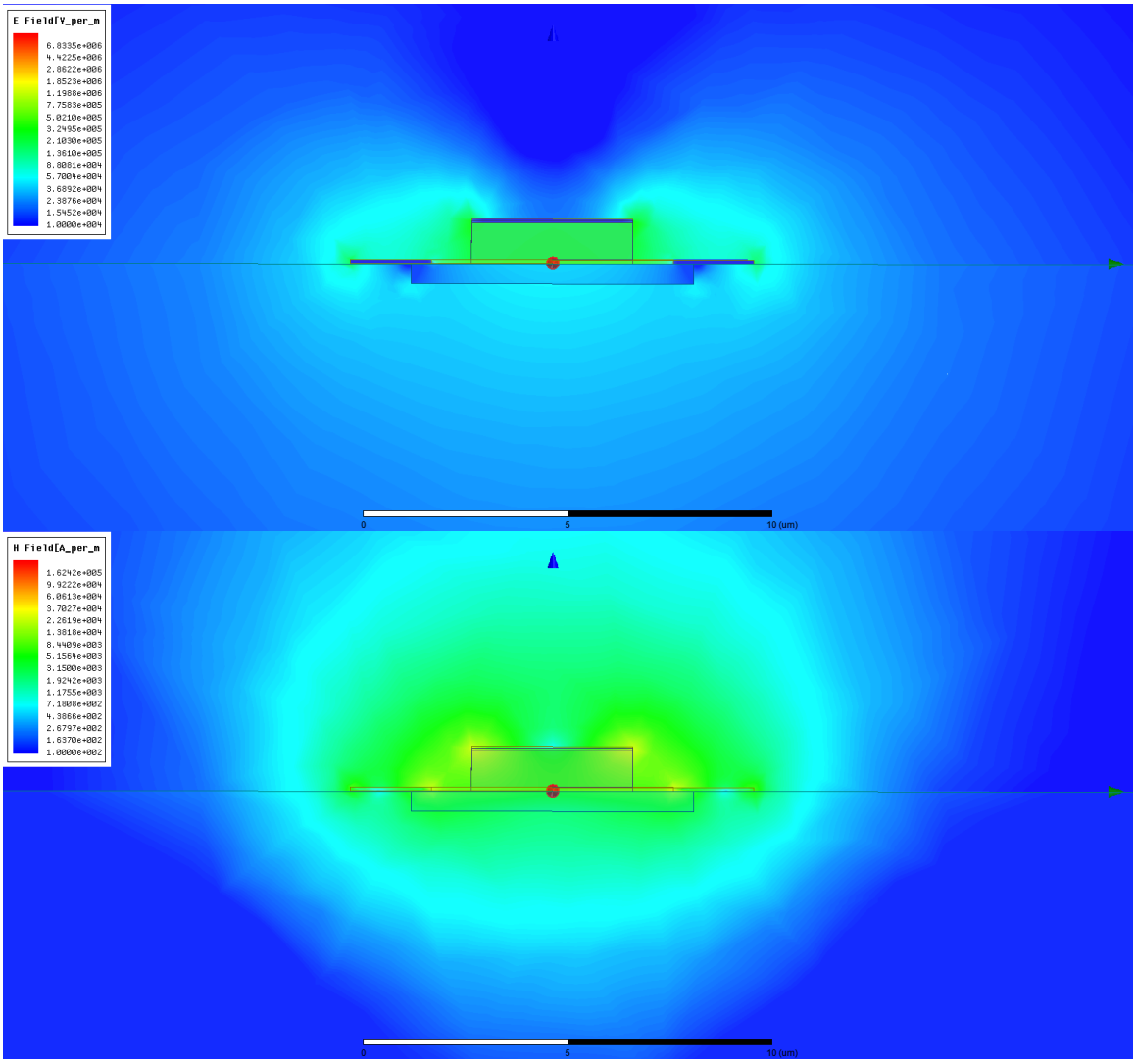

Figure Appendix E-7. Color plot of a cross-section of a UTC-PD device. The image shows an enlarged section of the device where the zoom is applied on the central stripline, lateral striplines, and the n-doped layer. This layer has a conductivity of 1.7×10^5 S/m and at a frequency of 100 GHz. a) Electric Field. b) Magnetic Field.

a)

b)

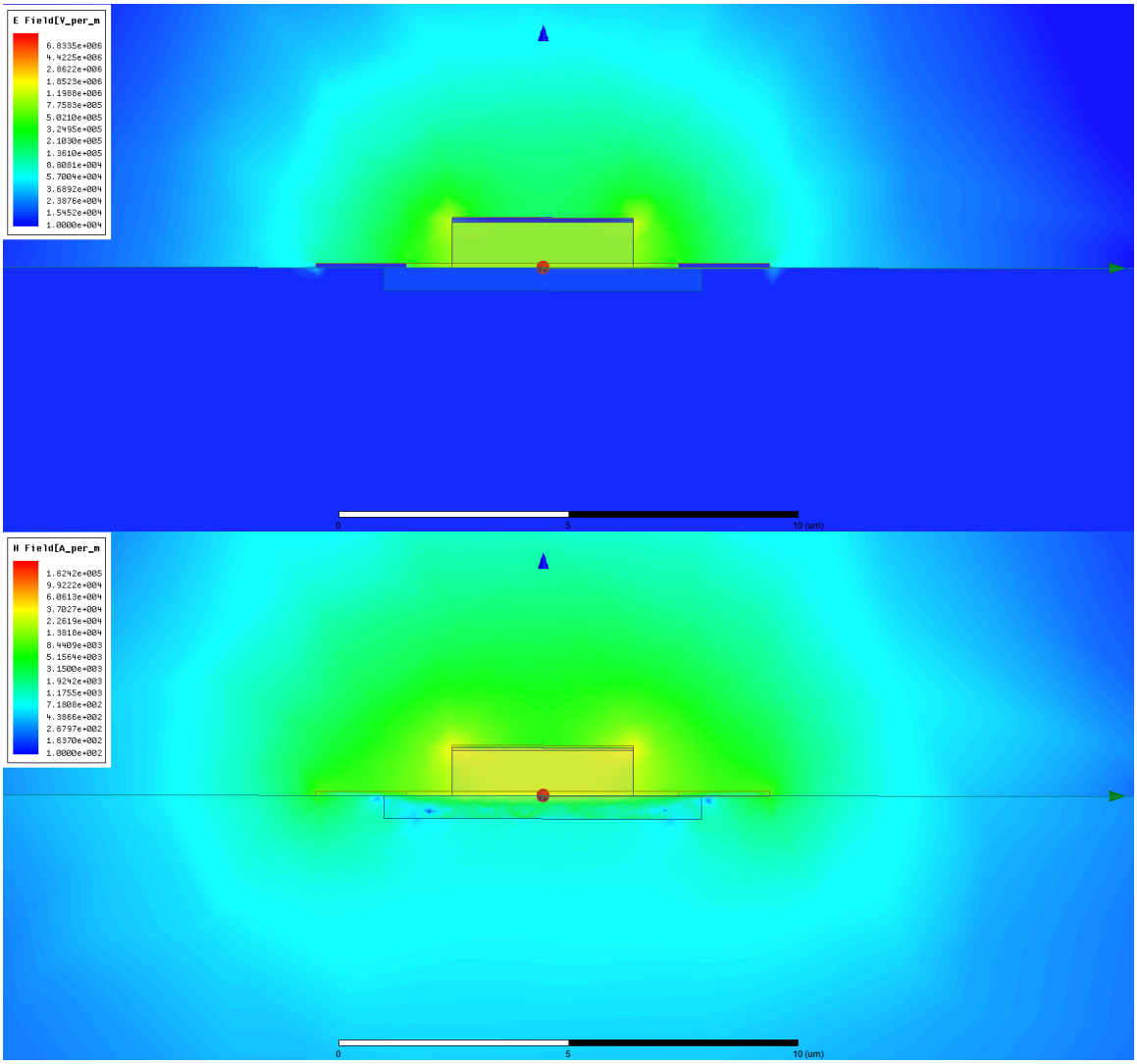

Figure Appendix E-8. Color plot of a cross-section of a UTC-PD device. The image shows an enlarged section of the device where the zoom is applied on the central stripline, lateral striplines, and the n-doped layer. This layer has a conductivity of 4.5×10^7 S/m and at a frequency of 100 GHz. a) Electric Field. b) Magnetic Field.

a)

b)

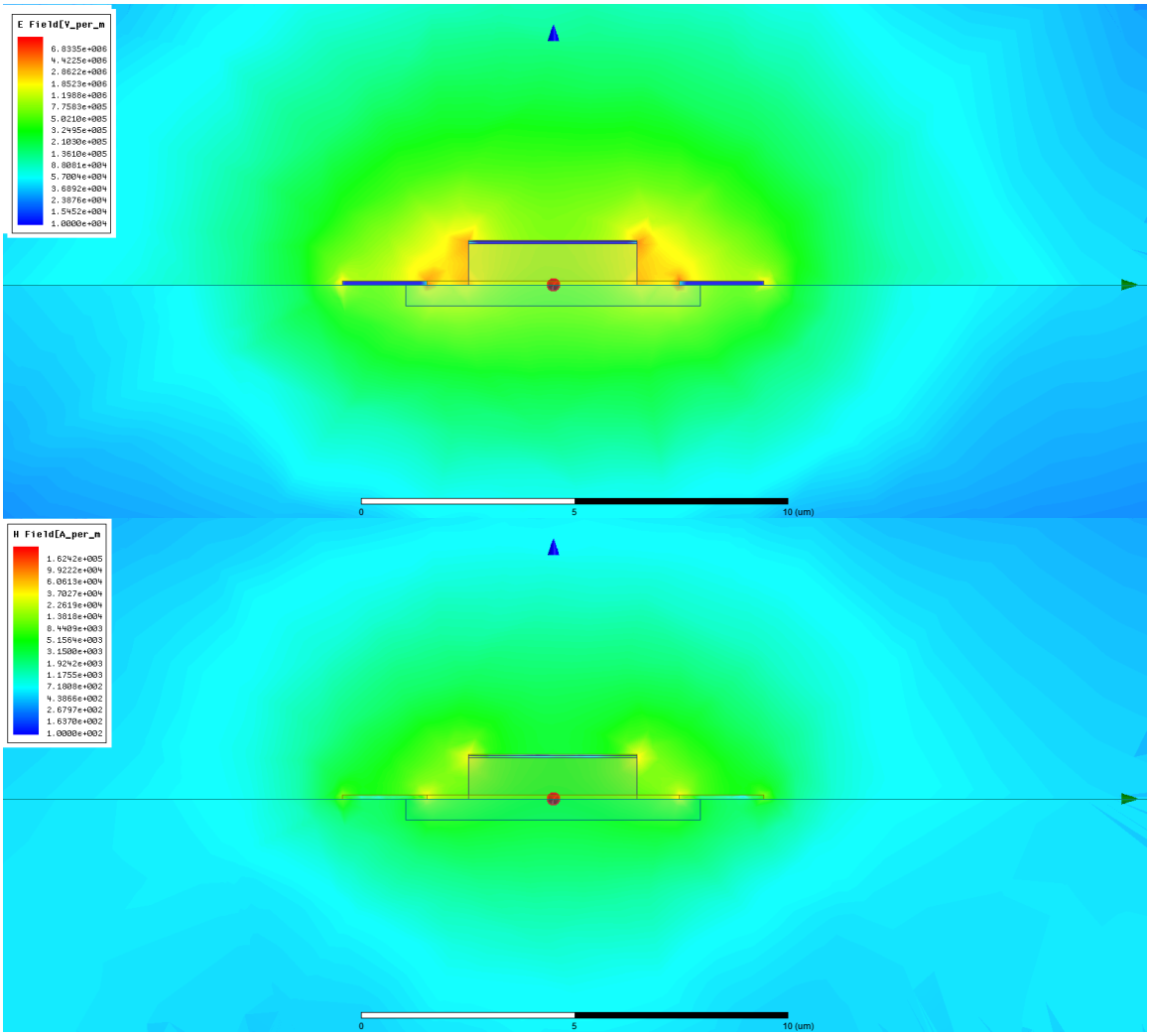

Figure Appendix E-9. Color plot of a cross-section of a UTC-PD device. The image shows an enlarged section of the device where the zoom is applied on the central stripline, lateral striplines, and the n-doped layer. This layer has a conductivity of 1.0×10^{-1} S/m and at a frequency of 1000 GHz. a) Electric Field. b) Magnetic Field.

a)

b)

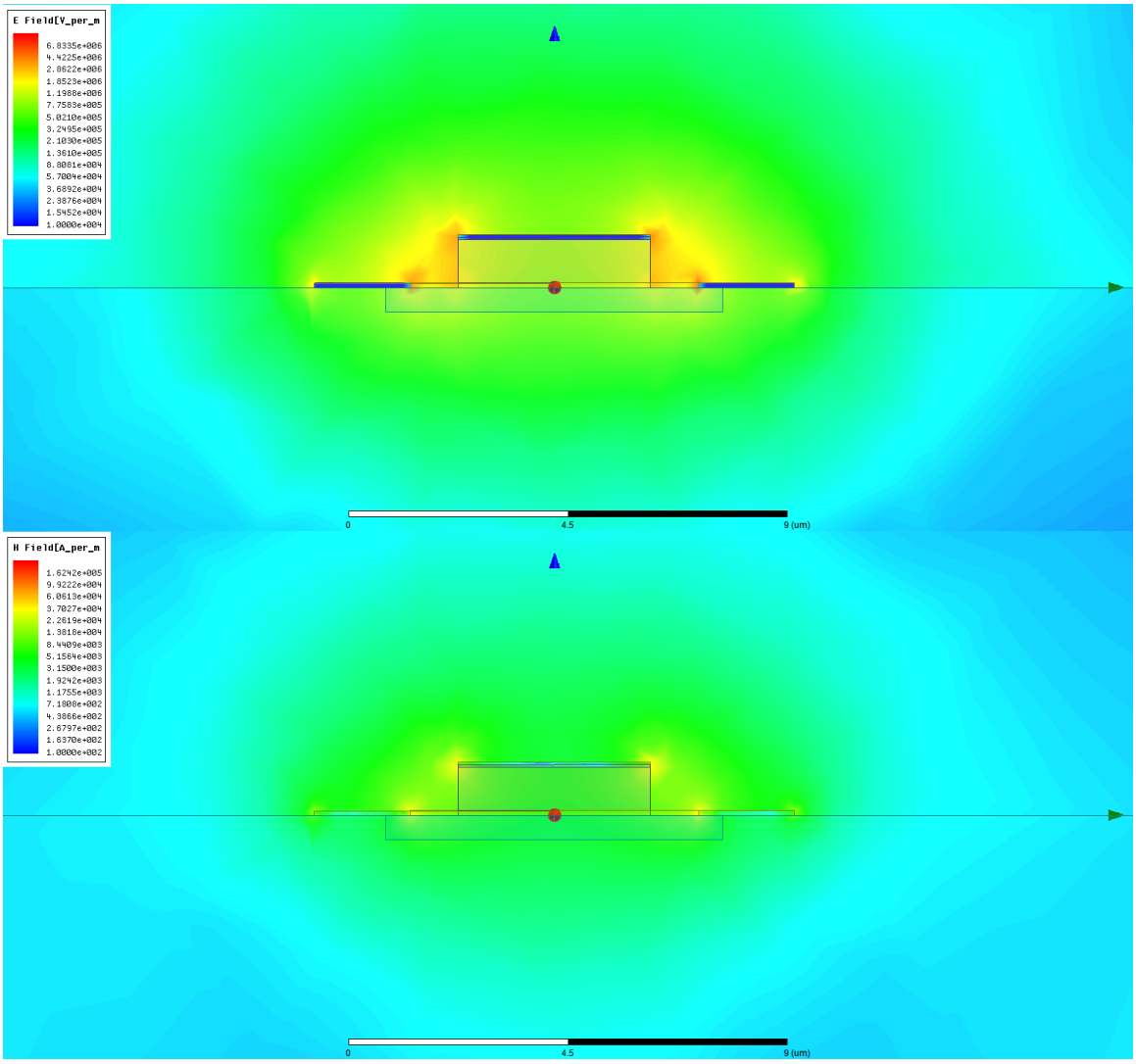

Figure Appendix E-10. Color plot of a cross-section of a UTC-PD device. The image shows an enlarged section of the device where the zoom is applied on the central stripline, lateral striplines, and the n-doped layer. This layer has a conductivity of 2.1×10^3 S/m and at a frequency of 1000 GHz. a) Electric Field. b) Magnetic Field.

a)

b)

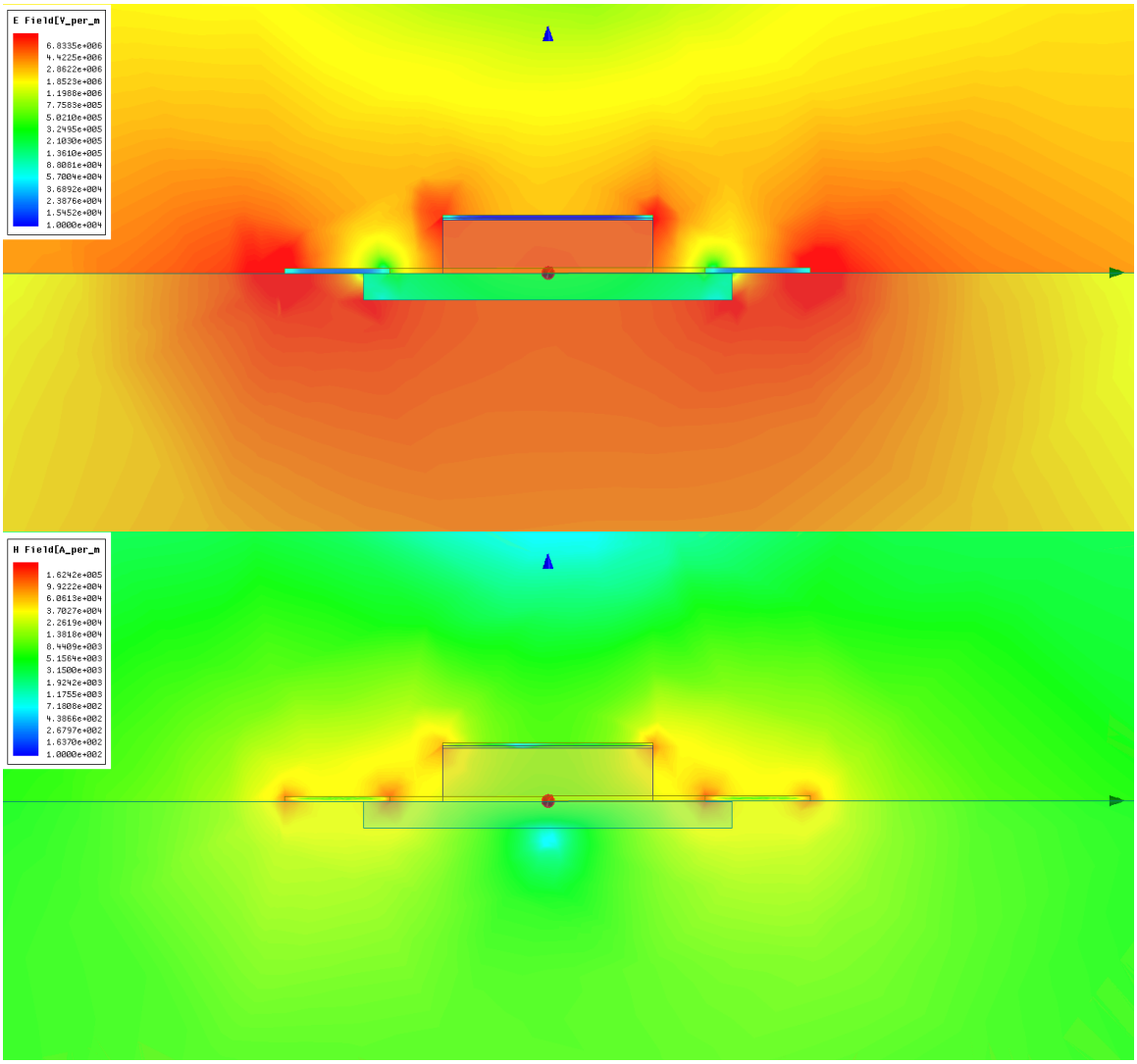

Figure Appendix E-11. Color plot of a cross-section of a UTC-PD device. The image shows an enlarged section of the device where the zoom is applied on the central stripline, lateral striplines, and the n-doped layer. This layer has a conductivity of 5×10^4 S/m and at a frequency of 1000 GHz. a) Electric Field. b) Magnetic Field.

a)

b)

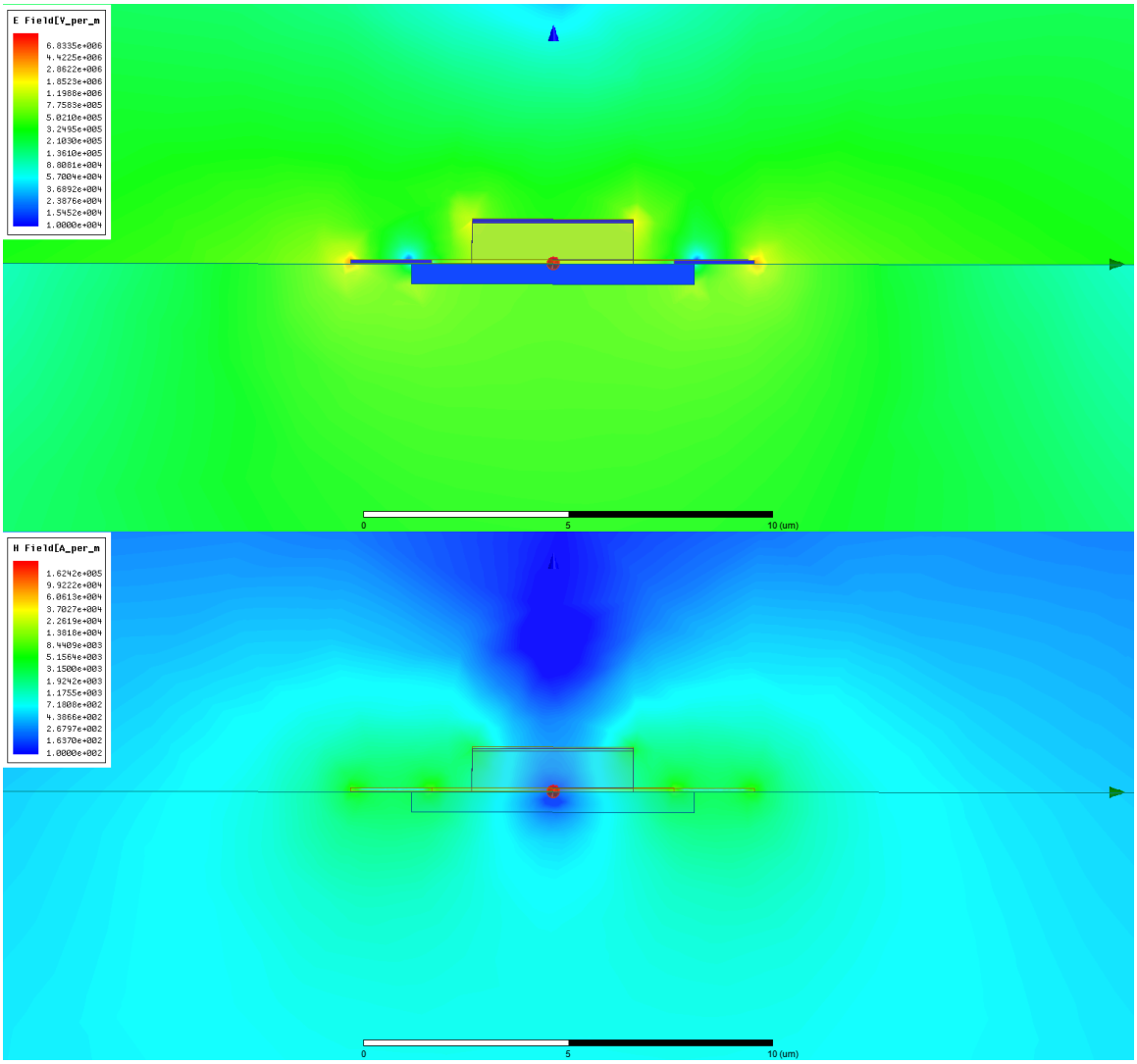

Figure Appendix E-12. Color plot of a cross-section of a UTC-PD device. The image shows an enlarged section of the device where the zoom is applied on the central stripline, lateral striplines, and the n-doped layer. This layer has a conductivity of 1.7×10^5 S/m and at a frequency of 1000 GHz. a) Electric Field. b) Magnetic Field.

a)

b)

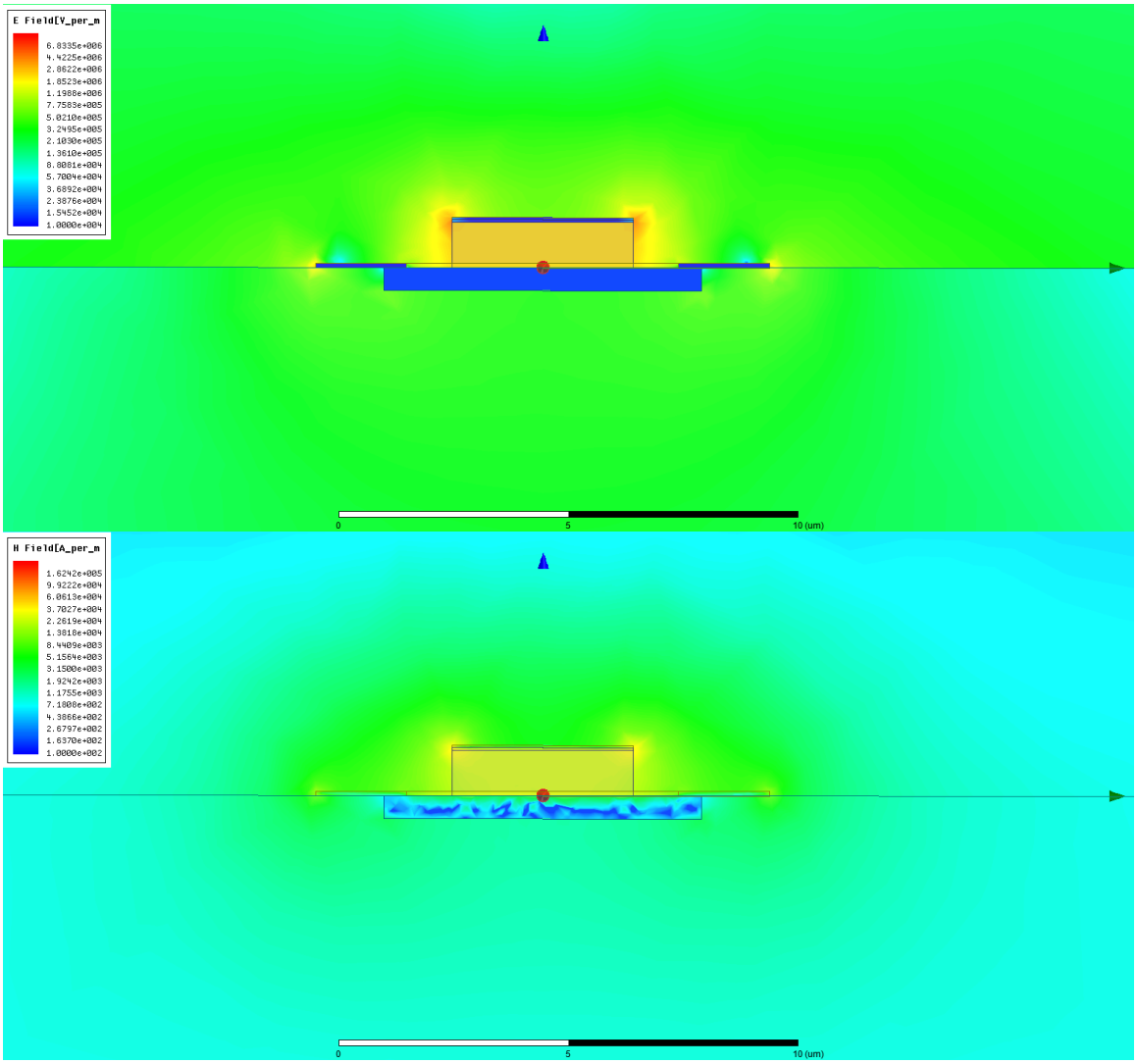

Figure Appendix E-13. Color plot of a cross-section of a UTC-PD device. The image shows an enlarged section of the device where the zoom is applied on the central stripline, lateral striplines, and the n-doped layer. This layer has a conductivity of 4.5×10^7 S/m and at a frequency of 1000 GHz. a) Electric Field. b) Magnetic Field.

a)

b)

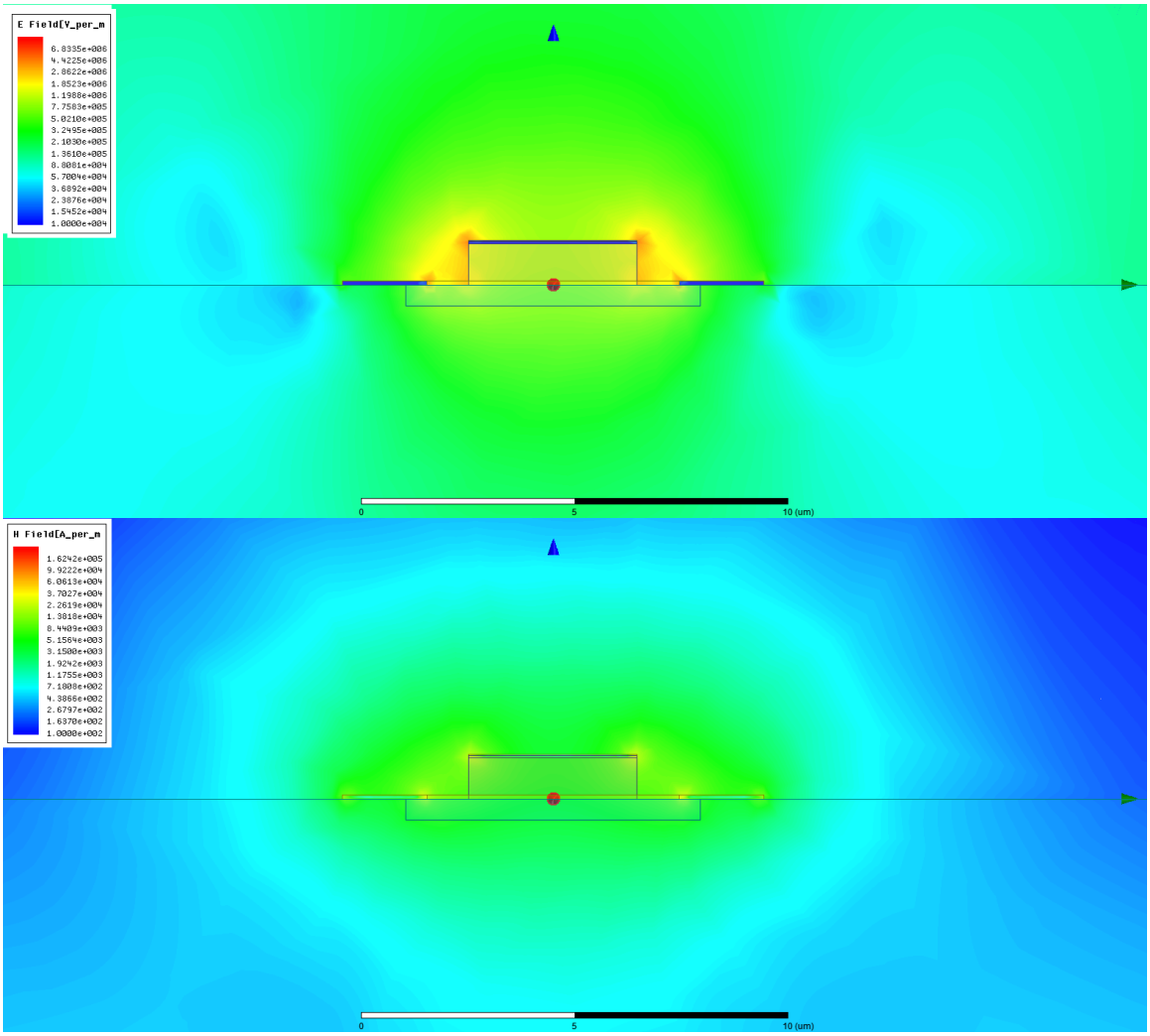

Figure Appendix E-14. Color plot of a cross-section of a UTC-PD device. The image shows an enlarged section of the device where the zoom is applied on the central stripline, lateral striplines, and the n-doped layer. This layer has a conductivity of 1.0×10^{-1} S/m and at a frequency of 2000 GHz. a) Electric Field. b) Magnetic Field.

a)

b)

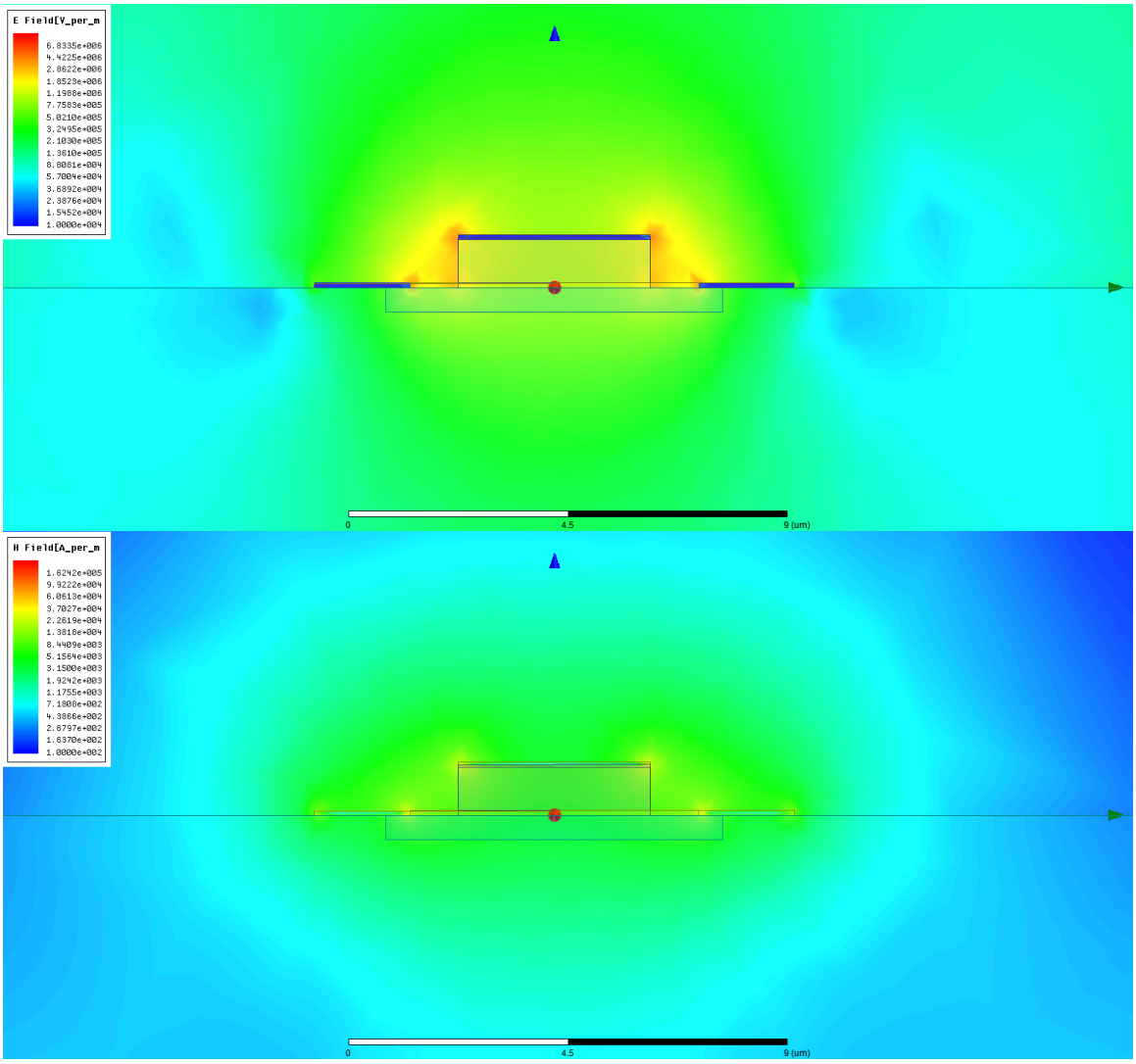

Figure Appendix E-15. Color plot of a cross-section of a UTC-PD device. The image shows an enlarged section of the device where the zoom is applied on the central stripline, lateral striplines, and the n-doped layer. This layer has a conductivity of 2.1×10^3 S/m and at a frequency of 2000 GHz. a) Electric Field. b) Magnetic Field.

a)

b)

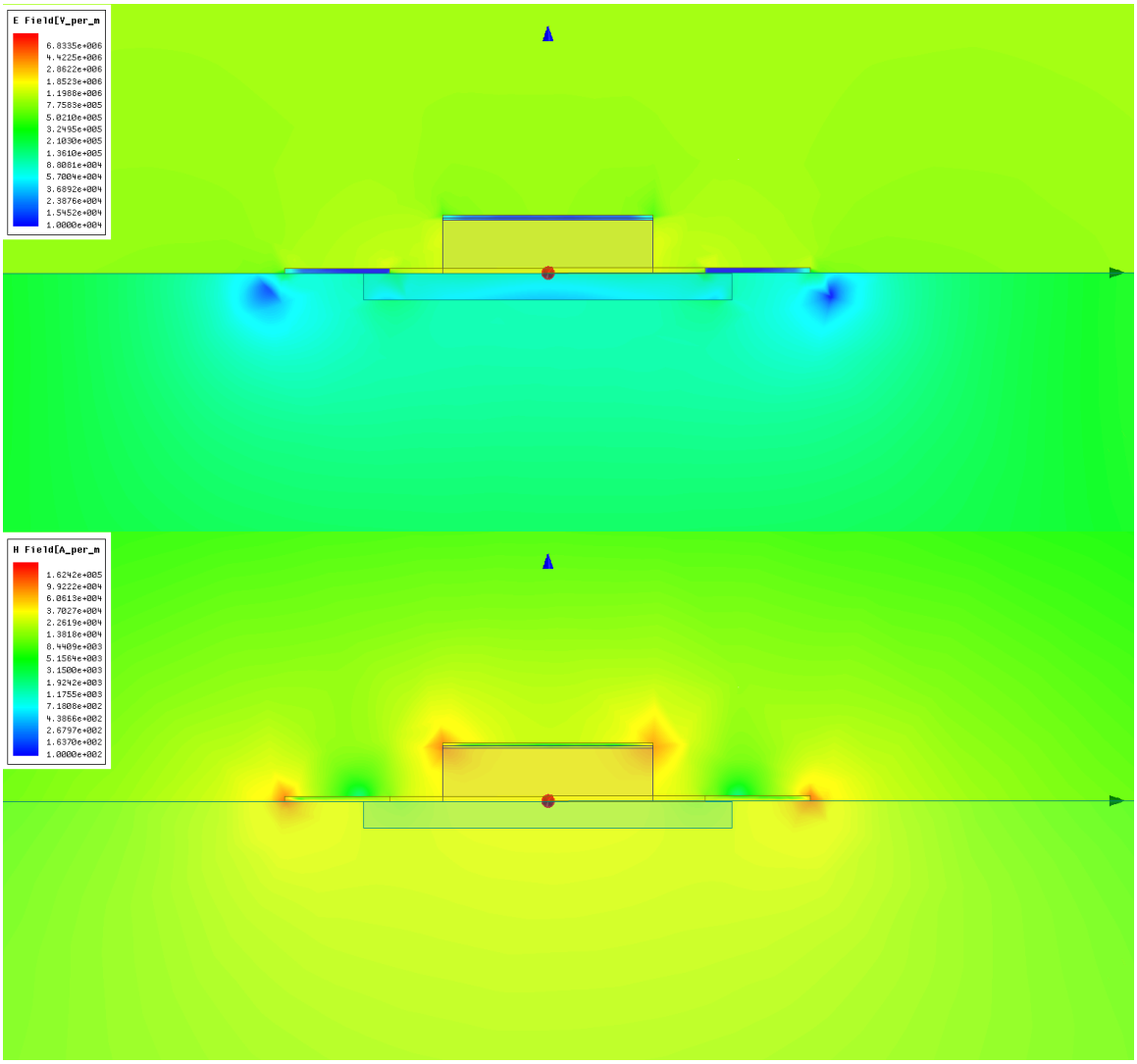

Figure Appendix E-16. Color plot of a cross-section of a UTC-PD device. The image shows an enlarged section of the device where the zoom is applied on the central stripline, lateral striplines, and the n-doped layer. This layer has a conductivity of 5×10^4 S/m and at a frequency of 2000 GHz. a) Electric Field. b) Magnetic Field.

a)

b)

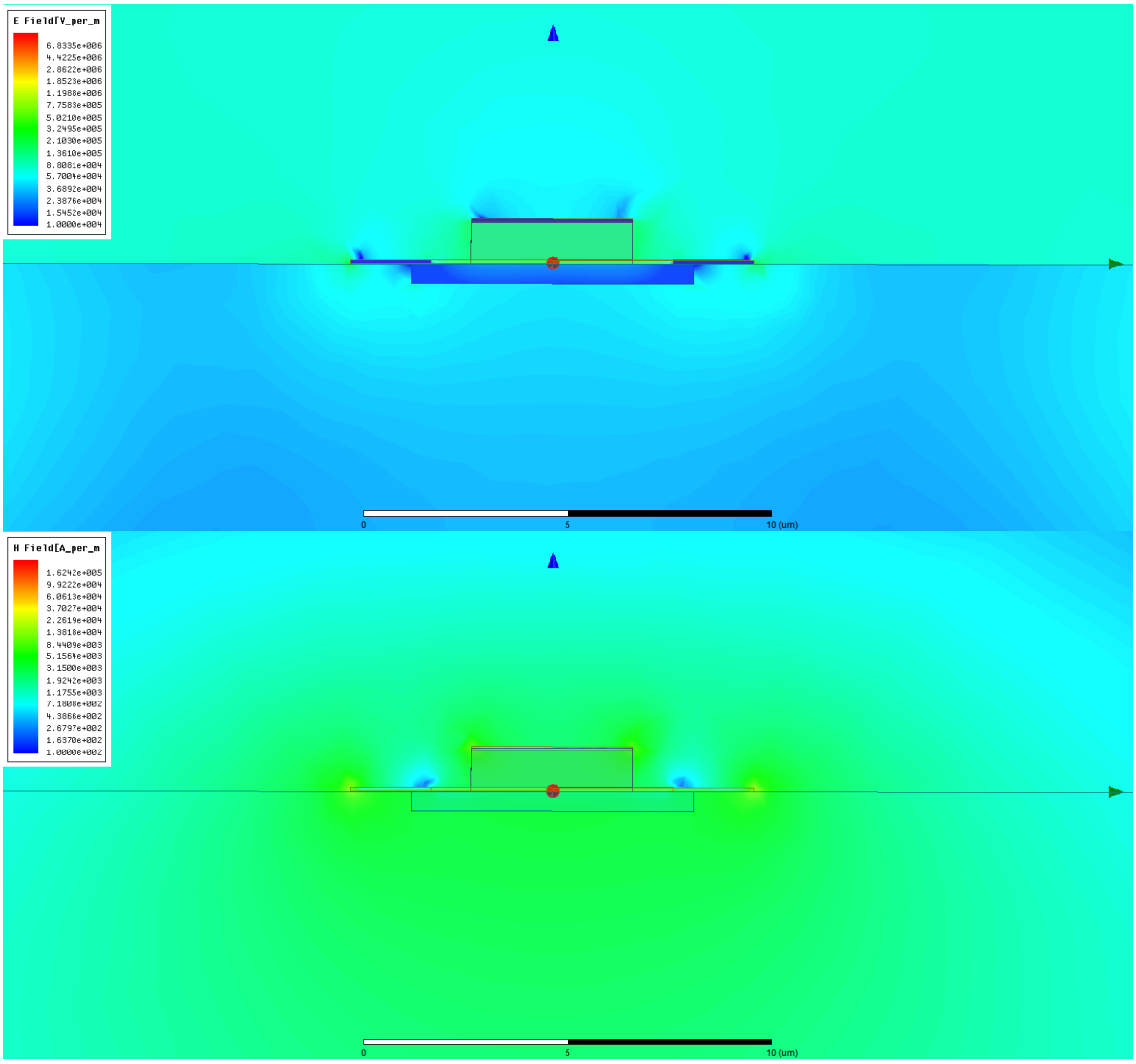

Figure Appendix E-17. Color plot of a cross-section of a UTC-PD device. The image shows an enlarged section of the device where the zoom is applied on the central stripline, lateral striplines, and the n-doped layer. This layer has a conductivity of 1.7×10^5 S/m and at a frequency of 2000 GHz. a) Electric Field. b) Magnetic Field.

a)

b)

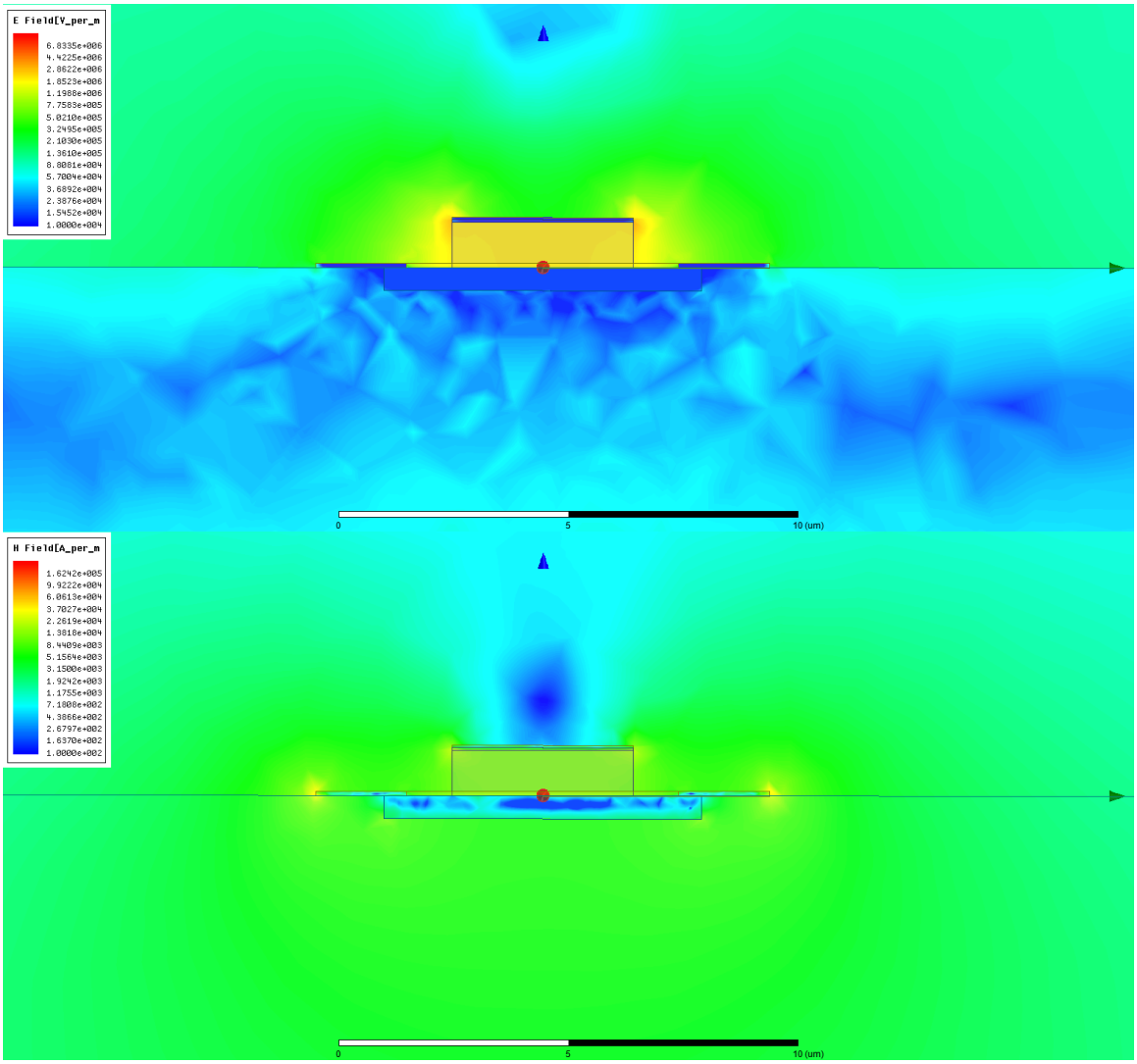

Figure Appendix E-18. Color plot of a cross-section of a UTC-PD device. The image shows an enlarged section of the device where the zoom is applied on the central stripline, lateral striplines, and the n-doped layer. This layer has a conductivity of 4.5×10^7 S/m and at a frequency of 2000 GHz. a) Electric Field. b) Magnetic Field.